Interannual Variations in the Structure and Interaction of Planetary Waves in the Southern Hemisphere Stratosphere

Yasuko Hio

March, 2004

Abstract

The winter polar vortex in the Southern Hemisphere stratosphere is characterized by quasi-stationary planetary wave of zonal wavenumber 1 (stationary Wave 1) and eastward traveling planetary wave of zonal wavenumber 2 (traveling Wave 2). Interannual variations of stratospheric circulations in the Southern Hemisphere (SH) are investigated in terms of interannual variations of these planetary waves using a long period of observational dataset.

Firstly, dynamical features of the interannual variations of the seasonal march in the SH stratosphere are examined and the unprecedented year 2002 in which a major stratosphere sudden warming occurred is characterized by comparing with the other 23 years (1979-2001). Interannual variations are characterized by early or late deceleration of the polar-night jet, which is well correlated with the variation of a time averaged upward wave activity flux in the lower stratosphere. The stronger wave activity in the lower stratosphere is associated with the earlier "shift-down" of the jet. In 2002, the upward wave activity flux in the lower stratosphere was much larger in August compared with the other 23 years and the large wave driving caused the earlier and larger deceleration of the mean zonal wind in the stratosphere.

Interannual variations of the stationary Wave 1 in late winter, when it is most vigorous, are characterized by east-west drifts of phase and wave amplitude variations. The variation of the phase is well related to the structure in the tropospheric jet over the Eastern Hemisphere. The activities of synoptic-scale waves in the middle troposphere maintain the difference of the tropospheric jet structure. The planetary-scale upward wave activity in the troposphere is larger when the stratospheric planetary Wave 1 has the large amplitudes and this inclination is most pronounced around the 300 hPa level.

I demonstrate the quasi-periodic variations of the polar vortex in terms of the wave-wave interaction between the stationary Wave 1 and the traveling Wave 2. A typical case study made clear that eastward traveling Wave 1 with the same angular frequency as the traveling Wave 2 is generated by the wave-wave interaction between the two waves. The generated traveling Wave 1 has a node in high-latitudes, where the two primarily waves have large amplitudes. The polar night jet also vacillates with the same frequency. This is due to quasi-periodic variations of the wave driving by the interference of the stationary and traveling Wave 1. Such quasi-periodic variations often occurred for the 24 years in late winter when both the stationary Wave 1 and the transient Wave 2 are vigorous. Similar periodic variations of the polar vortex are reproduced in a barotropic model experiment in

the circumstance that stationary Wave 1 generated by surface topography has a comparable amplitude to eastward traveling Wave 2 which is generated by the barotropic instability of the forced mean zonal wind.

Contents

Chapter 1

Introduction

One of the most important dynamical properties in the winter stratosphere is the forced planetary waves. They interact with the mean zonal flow and sometimes with the other scale waves. For example, stratospheric sudden warming (SSW) event in the winter NH, which is characterized by breakdown of the wintertime westerly polar vortex, is associated with the planetary wave activities from the troposphere. The SSW event occurs on average once every other year and is a main factor in intraseasonal and interannual variations of the winter stratosphere in the NH. Thus, the study of the planetary waves is invaluable to understand intraseasonal, interseasonal, and interannual variations of the stratospheric circulations. In this thesis I shed light on the interannual variations in the planetary waves and circulations related to the planetary wave activities in the less-known Southern Hemisphere (SH) stratosphere.

1.1 General circulation and its variations

The stratosphere in the SH was one of the most difficult regions to know their features. It was not until the latter half of the 1970s that the satellite measurement enabled us to investigate the general circulations in the both NH and SH equally and that the understanding of the thermal and dynamical features proper to the SH had grown up (e.g. Harwood 1975; Hartmann 1976; Leovy and Webster 1976). In the subsequent 1980s, analyses of long dataset brought us a fundamental knowledge about the climatological seasonal march of the SH circulation (e.g. Hartmann et al. 1984; Mechoso et al. 1985). We can overview a fairly reliable climatological features of the SH circulations, including climatological variability, based on the longer record of observational data now available (e.g. Randel and Newman 1998).

Figure 1.1(a) shows the climatological zonal mean temperature (thick white line) at 80°N (left) and 80°S (right) for the 15 years from 1979 to 1994 together with its variable range (shaded region) and the seasonal march in 1994-1995 for the NH and in 1995 for the SH. The climatological zonal mean polar temperature in the SH middle stratosphere is colder than in the NH in midwinter. The stratospheric zonal mean zonal wind is in approximate thermal wind balance with the zonal mean temperature, and thus the polar-night jet is much stronger in the SH than in the NH as shown in Fig. 1.1(b). The polar-night jet in the SH exists in the upper stratosphere in autumn. It strengthens and descends till

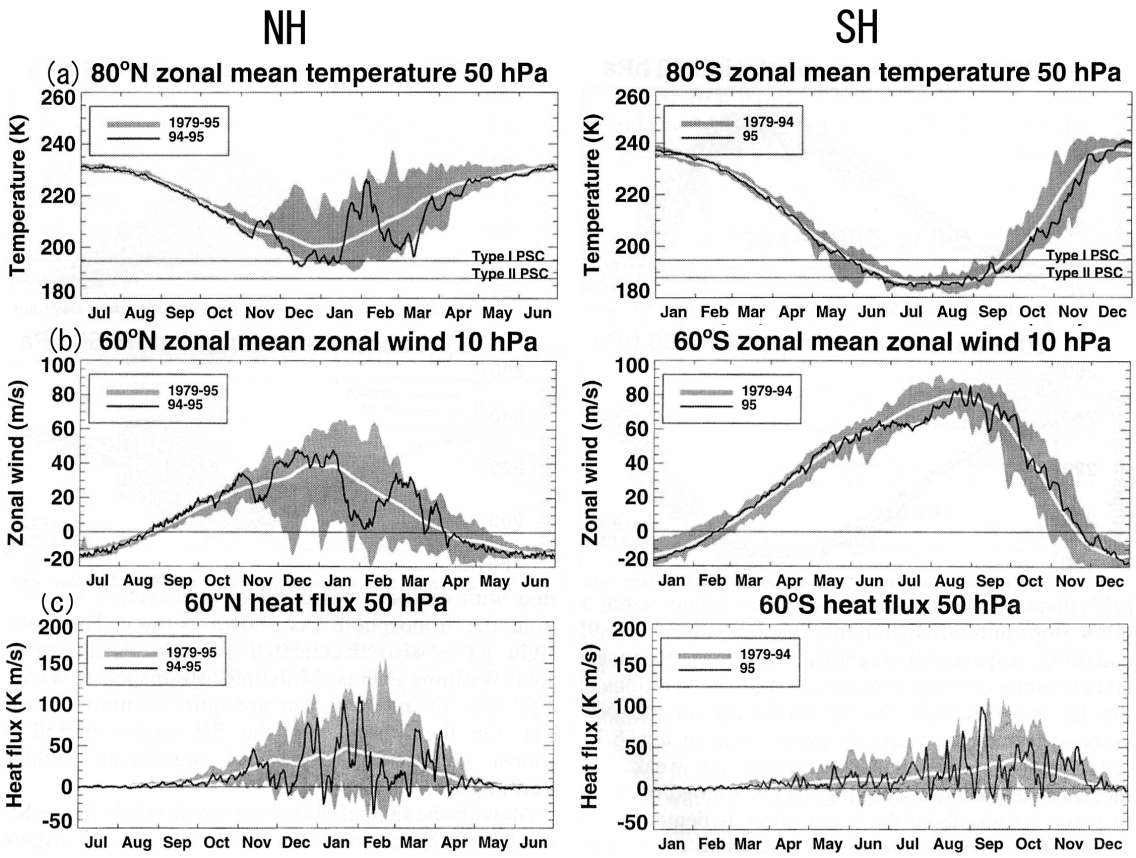

Figure 1.1: Time series of the climatology (white lines) for 15 years from 1979 to 1995 for the NH (left) and SH (right) along with the extrema of daily values (shade region): (a) 50-hPa zonal-mean temperatures at 80°N and 80°S, (b) 10-hPa zonal mean zonal wind at 60°N and 60°S , and (c) 50-hPa poleward eddy heat flux by all the waves at 60°N and 60°S. The thin solid line in each figure shows the time series in 1994-1995 and 1995, for the NH (top) and SH (bottom), respectively. (From Randel and Newman 1998)

midwinter. The core of the jet moves poleward and downward in late winter and spring with the transition of the zonal mean zonal wind from the westerly to the easterly from top down. The breakdown of the polar vortex is much delayed till spring compared to the NH (Fig. 1.1b).

These stratospheric differences in the zonal mean fields between the hemispheres are due to the differences in a residual circulation which is mainly controlled by planetary wave drivings. The residual mean circulation provides a concise view of transport in the meridional plane. A schematic of the residual mean circulation is shown in Fig. 1.2. The planetary waves generated in the troposphere propagate into the stratosphere and dissipate in the stratosphere in the winter hemisphere. The dissipation of the planetary waves induces the residual circulation from the tropics into high latitudes and the adiabatic pressure changes in the air below lead to a positive deviation of the temperature field from the radiatively determined equilibrium in high latitudes. Fig. 1.1(c) displays the climatological 50-hPa poleward eddy heat flux by all the waves at 60°N (left) and 60°S (right). The upward planetary wave activity is proportional to the poleward eddy heat

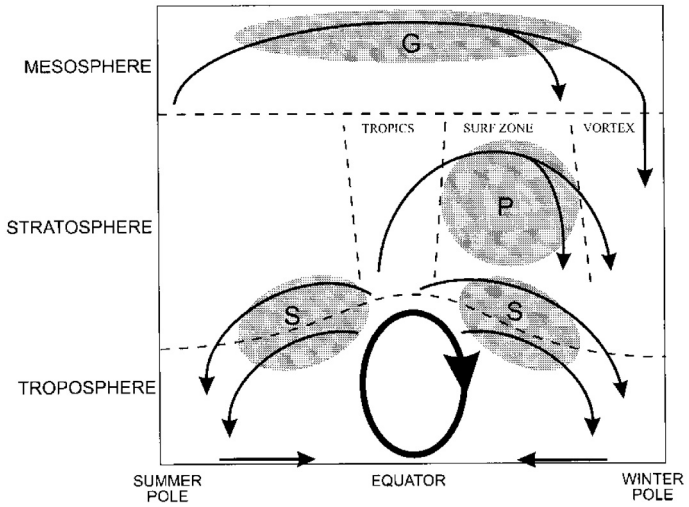

Figure 1.2: Schematic of the residual mean meridional circulation in the atmosphere. The shaded regions (labeled " S" , " P" , " G") denote regions of breaking waves (synoptic scale wave, planetary wave and gravity waves, respectively), responsible for driving branches of the stratospheric and mesospheric circulation. The heavy ellipse denotes the thermally-driven Hadley circulation of the troposphere. (From Plumb 2002)

flux. In addition, synoptic-scale waves (zonal wavenumber 4-7) do not propagate into the stratosphere but rather propagate equatorward or are absorbed in the middle upper troposphere. Thus, the poleward eddy heat flux in the lower stratosphere is used as a measure of the wave activity of the planetary wave entering the stratosphere. The wave driving in the SH has its maximum value in late winter (September-October), whereas the wave driving in the NH has strong value throughout midwinter (November-March). The weaker wave driving in the SH midwinter is related to the weaker mid-winter residual circulation, and results in the colder and more intense polar vortex. The stronger wave driving in the SH late winter results in the strong residual circulations and the smooth transition to the summer easterlies.

Fig. 1.1 also demonstrates that the variance of the polar temperature and that of the zonal mean zonal wind at high latitude on both intraseasonal and interannual timescales in the SH are smaller than in the NH. The large variations of the zonal mean polar temperature and the zonal mean zonal wind at high-latitude in the NH winter are due to large interannual variations in the poleward eddy heat flux, which are direct results of SSW events with the bursts of the wave activity from the troposphere. On the other hand, the interannual variations of the zonal mean temperature and the zonal mean zonal wind in the SH are much smaller than those in NH primarily because of no occurrence of SSW events before 2002. The large interannual variations of the zonal mean field in the SH in late winter are also associated with the large interannual variations of the wave activity.

Figure 1.3 shows Hovmöller diagrams of the planetary wave of zonal wavenumber 1 (a) and 2 (b) at 60°S, 20 hPa for 24 years from 1979 to 2002. In the SH, the planetary wave of

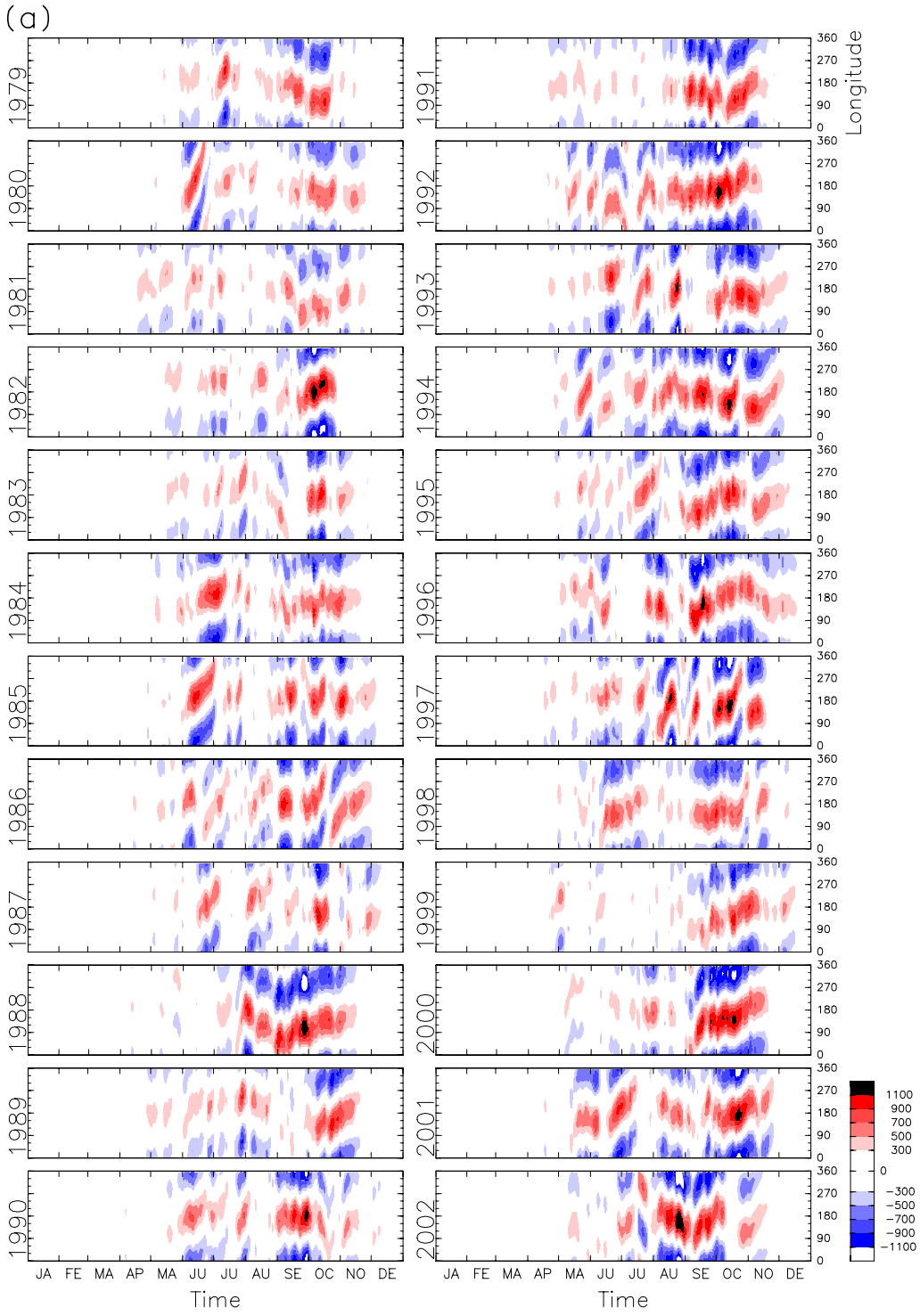

Figure 1.3: Hovmöller diagrams of the (a) Wave 1, (b) Wave 2 for the geopotential height field at 20 hPa 60°S for the 24 years from 1979 to 2002.

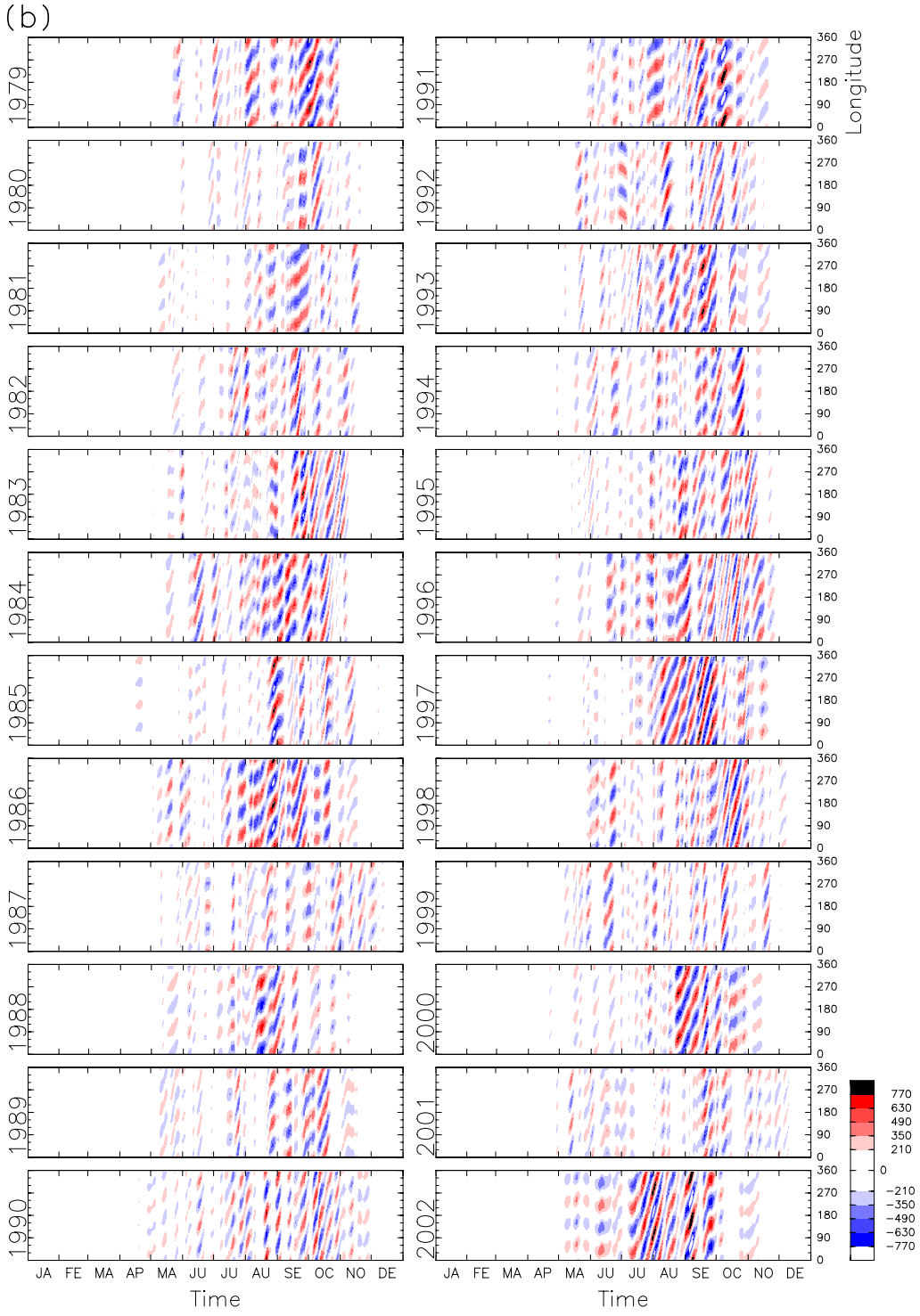

Figure 1.3: *(figure continues)*

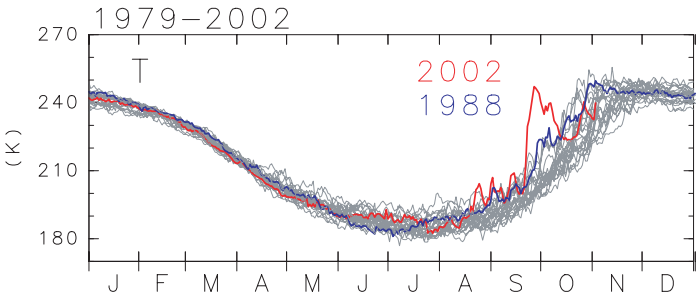

Figure 1.4: 24-year records of the daily evolution of the temperature at the South Pole. Red (blue) line denotes day-to day variations in 2002 (1988). (From Baldwin et al. 2003)

zonal wavenumber 1 in mid- and late-winter is characterized by the stationary component of zonal wavenumber 1 (hereafter stationary Wave 1), while the planetary wave of zonal wavenumber 2 is characterized by eastward propagating component (hereafter traveling Wave 2) with the period about 15 days. The amplitude of the stationary Wave 1 is smaller than that of the NH, owing to the smaller thermal and topographic forcing to generate the waves which propagate into the stratosphere. There are two vigorous seasons of the wave activity, one in early winter and the other in late winter. Seasonality and structure of the stationary waves in the NH stratosphere are reasonably well explained in terms of forcing from the troposphere and variations in background flow (e.g. Karoly and Hoskins 1982). On the other hand, there is less detailed understanding of the stationary Wave 1 in the SH. As to the Wave 2, generation mechanism has been proposed, such as vertical propagation from the troposphere (Randel 1987) and barotropic instability of the stratospheric wind (e.g. Hartmann 1983: Manney 1988).

Fig. 1.3 exhibits interannual variations of the planetary Waves 1 and 2. In this study, I investigate the interannual variations in the SH stratosphere concerning the planetary waves of the stationary Wave 1 and the traveling Wave 2.

1.2 Stratospheric sudden warming in 2002

The small interannual variations in the SH are mainly due to non-occurrence of SSW events as explained in the previous section. However, in September 2002 the SH stratosphere underwent major stratospheric warming, splitting the vortex and tearing the ozone hole into two parts for the first time since global maps for the stratosphere of the SH became available. The stratospheric temperature at the South Pole increased by about 50K for a week in late September (Fig. 1.4). Figure 1.5 shows time evolutions of potential vorticity (PV), which is a dynamical quantity conserved materially for adiabatic frictionless condition. On 15 September, the polar vortex is characterized by high values of PV (indicated in blue), with a sharp gradient of PV associated with strong westerly jet stream. Outside the polar vortex, gradients of PV are small and widespread filamentary structure exists in conse-

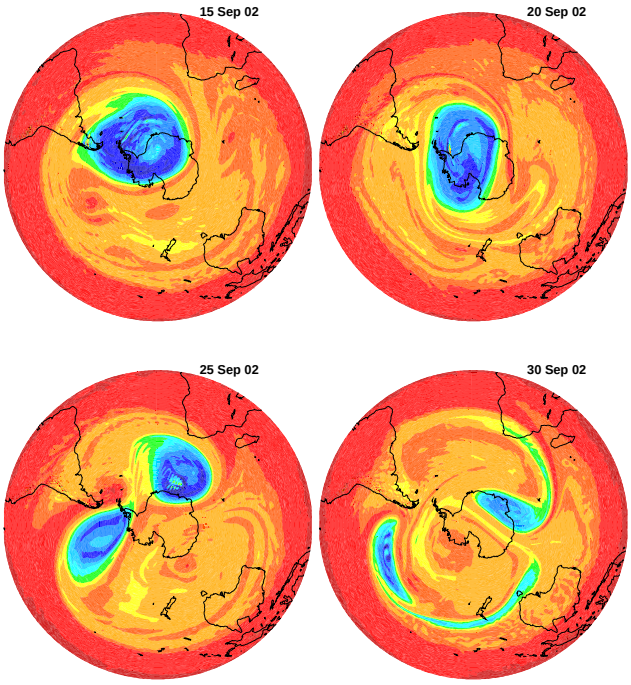

Figure 1.5: Potential vorticity on the 850K isentropic surface (near 10 hPa) for the SH on 15, 20, 25 and 30, September 2002. Values of potential vorticity associated with the stratospheric polar vortex are indicated with the color blue. (From Baldwin et al. 2003)

quence of the mixing by large-scale nonlinear advection acting on the sharp gradients of PV, which is associated with the anticyclones tracking eastward around the polar vortex. An elongated high PV rotated eastward in mid September and shifted off the pole just before the event. The subsequent split on 25 September leads to two distinct centers of high PV. Once the vortex has split, the individual vortices are rapidly weakened by the shearing out of PV around the anticyclones. These process can be regarded as the time variations of the structure and interaction of the planetary waves. Seen from monthly mean structure, the planetary Waves 1 and 2 in the stratosphere were much more vigorous in 2002 compared to the other years during July August, and September (Fig. 1.6). This indicates that the wave activities of the planetary Waves 1 and 2 in 2002 were already large as early as in midwinter compared to those in the other years.

The interannual variations of the seasonal march in the SH stratosphere and those relation to the tropospheric circulations were studied by several authors (e.g. Shiotani et al. 1993; Aoki et al. 1996; Kuroda and Kodera 1998). Shiotani et al. (1993) classified the 10 years during the 1980s into two categories in terms of the location of the maximum westerlies at the 1 hPa level in midwinter; the low-latitude-jet (LLJ) years and the high-latitude-jet (HLJ) years. During late winter, the polar-night jet moves poleward and downward earlier in HLJ years than in LLJ years (Fig. 1.7). Accompanying with the difference in the timing of the movement, the growth of the amplitude of planetary Waves 1 and 2 during the period from winter to spring is earlier in HLJ years than in LLJ years.

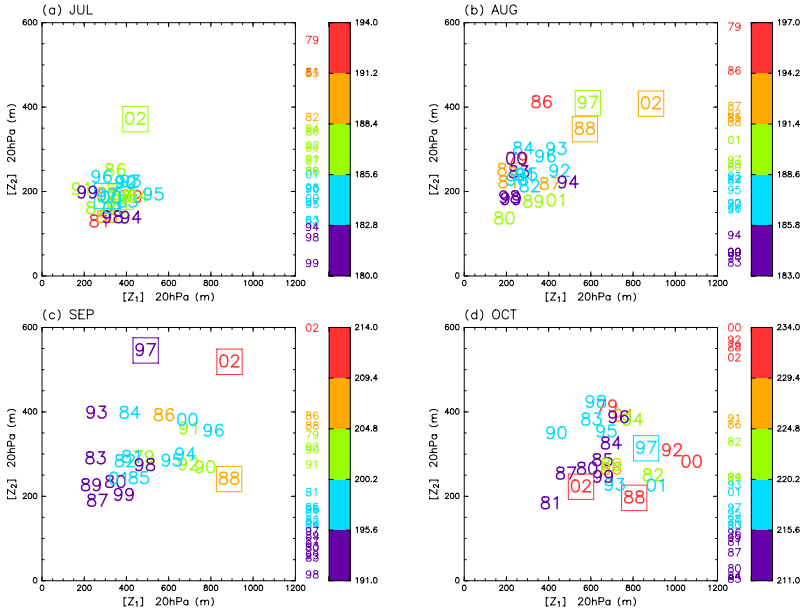

Figure 1.6: 24-year records of the monthly mean of daily geopotential height amplitudes of Waves 1 and 2 averaged over the latitudes between 60°S and 70°S, at the 20 hPa level. Monthly mean temperature at the pole is also shown with color indicated on the right side of each panel. (From Baldwin et al. 2003)

Aoki et al. (1996) investigated the interannual variations in the seasonal march of the upper tropospheric jet structure in the SH and those relation to the stratospheric polar-night jet. They defined a zonal index by the difference of the zonal mean zonal wind speed between 60°S and 40°S and found that the deviation of the zonal index from the climatology is an indicator of two typical latitudinal profile of the tropospheric zonal mean zonal mean wind: the single-jet and double-jet structure. The seasonal evolution of the zonal mean zonal wind is separated into two categories, DS (double-single) years and SD (single-double) years. DS years are characterized by a double-jet structure in early winter and a single-jet structure in late winter, while in SD years the zonal mean zonal wind has a single-jet structure in early winter and changes its profile into a double-jet structure in late winter. They showed that appearance of DS and SD years is similar to LLJ and HLJ years, which suggests the interannual variations of the seasonal evolution in the SH stratosphere are well related to those in the troposphere.

Another approach to the interannual variations in the stratosphere is a diagnosis of planetary wave activity entering the lower stratosphere, which is a good dynamical proxy for the diabatic meridional circulation. Fusco and Salby (1999) showed that interannual variations of total ozone operate coherently with variations of upward EP flux in the lower stratosphere in the winter NH (Fig. 1.8). The upward EP flux in the lower stratosphere is also a good precursor for the polar temperature in the stratosphere in the winter NH (Newman et al. 2001). Randel et al. (2002) examined the space-time patterns of correlations between column ozone tendency and the upward EP flux in the lower stratosphere and found a strong correlation during winter to spring in the SH as well as the NH.

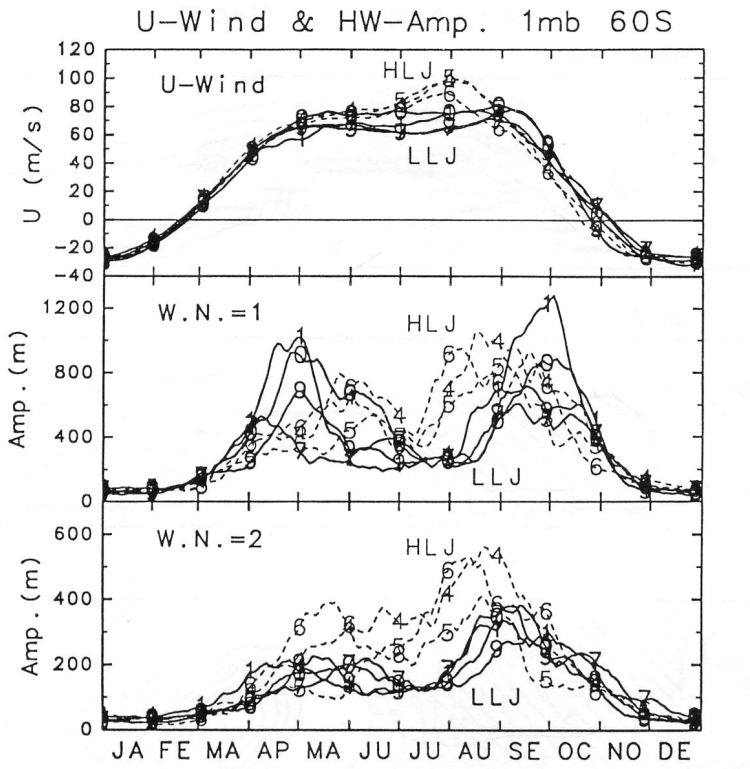

Figure 1.7: Annual movements of the zonal mean wind (top) and the Wave-1 (middle) and Wave-2 (bottom) amplitudes at 1 hPa, 60°S for HLJ years (broken lines) and LLJ years (solid lines). Numbers on each line refer to the year in the period 1980 to 1989. (From Shiotani et al. 1993)

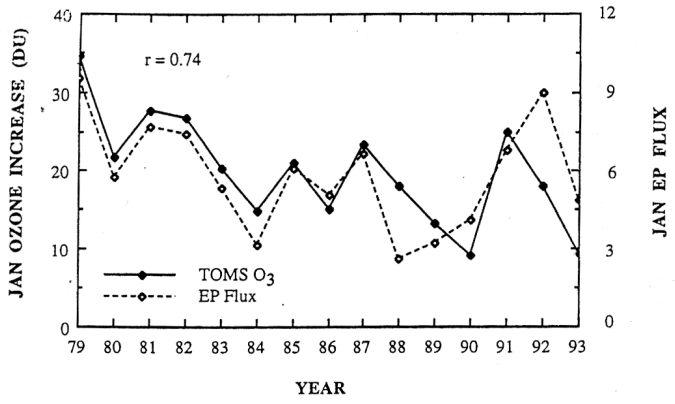

Figure 1.8: Upward EP flux at 100 hPa during January (normalized), averaged over the winter hemisphere (dashed line), compared against the corresponding increase of extratropical total ozone. (From Fusco and Salby 1999)

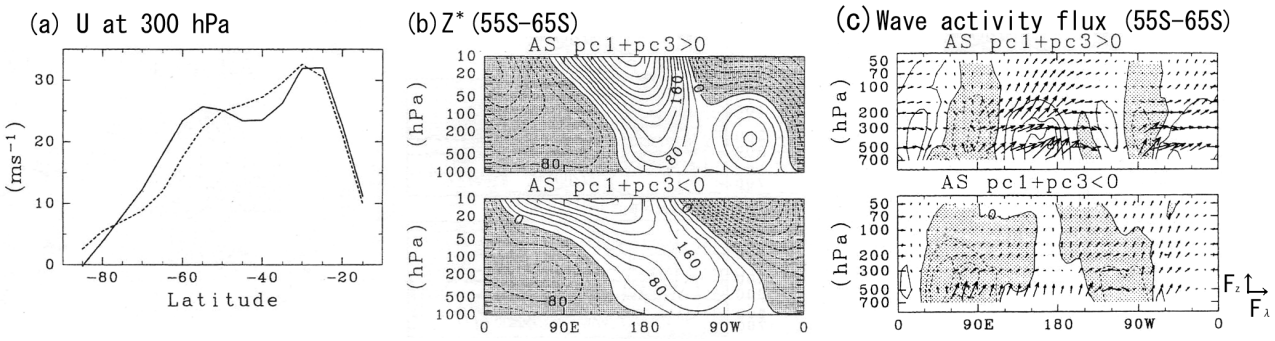

Figure 1.9: Latitudinal structure of composite zonal mean zonal wind at 300hPa (a) for double-jet group (solid line) and single-jet group (dotted line) during August and September, and longitude-hight sections of non-zonal component of geopotential height (b) and stationary wave activity flux (c) for the double-jet group (top) and the single-jet group (bottom). As to the wave activity flux, the zonal and vertical components are drawn by arrows and the meridional component is drawn by contour. (From Aoki and Hirota 1998)

Following these studies, I investigate the interannual variations of the seasonal march in the stratosphere and their relation to the troposphere in order to characterize the unprecedented year 2002, using the stratospheric zonal mean zonal wind and the upward wave activity flux as indices. I also focus attention on the skewed provability distribution of the polar temperature in September shown in Fig. 1.6 and discuss the provability distributions of the indices of the interannual variations. The results are given in Chapter 2.

1.3 Interannual variations in stationary Wave 1

The stationary Wave 1 is generated in the troposphere by large scale topography, land-sea temperature contrasts, and transient eddy component, and is propagated into the stratosphere. It is much more numerous in the NH winter than the SH due to the stronger NH topographic forcing and land-sea surface contrast. As to the SH, the main source of the stationary Wave 1 has been proposed. The non-axisymmetric orography of the Antarctica has been considered as the important source of the stationary planetary Wave 1 (e.g. James 1988; Watterson and James 1992). On the other hand, the analysis of the 15-year NMC data by Quintanar and Mechoso (1995a) suggests that stationary Wave 1 is primarily forced from lower latitudes, most prominently from the Indian Ocean region during winter. They showed that low frequency waves act to strengthen the stationary Wave 1. Their GCM model experiment (Quintanar and Mechoso 1995b) emphasizes that the winter stationary Wave 1 in the troposphere around the Antarctica is primarily generated by mechanisms other than the Antarctic elevations, such as the topographic forcing in the other regions, thermal forcing from lower latitudes, and the transient eddy component.

As shown in Fig. 1.3a, there are interannual variations in the phase and amplitude of the stationary Wave 1 for the 24 years. Aoki and Hirota (1998) investigated the three dimensional structure and the behavior of quasi-stationary planetary waves in the SH

winter in relation to the tropospheric zonal mean zonal wind variation as mentioned in previous section, i.e. double-jet structure and single-jet structure. The vertical structure of the quasi-stationary planetary waves exhibits large difference between the two categories in late winter (August and September) as shown in Fig. 1.9(b): In the years that the tropospheric jet has double-jet structure, the ridge of the stationary Wave 1 at 10 hPa is located around 170°E which is traced down to the positive anomaly around 160°W in the middle troposphere. On the other hand, when the tropospheric jet has single-jet structure, the ridge of the stationary Wave 1 at 10 hPa is located to the west around 145°E, which is traced down to the positive anomaly located to the east around 120°W. Corresponding to these differences, the stationary wave activity also shows different features between the two categories (Fig. 1.9c). When the tropospheric jet has the double jet structure, there are strong fluxes around 180°, where the Wave 1 is propagated from polar latitudes. On the other hand, the wave activity is weak for the single-jet structure. Intense fluxes are obvious around 90°E in the troposphere which seem to have their origin at lower latitudes. These suggest that the interannual variations in the amplitude and phase of stationary Wave 1 in the stratosphere are related to the tropospheric wave activity.

As a step toward the understanding of the generation mechanism of the stationary Wave 1, I investigate the interannual variations of the stationary Wave 1 in the SH stratosphere in relation to the tropospheric circulations such as the zonal wind and the wave activities. I pay my attention to the period in late winter because the amplitude of the stationary Wave 1 has its maximum and its interannual variability is also large in this period (cf. Figs. 1.3a and 1.7).

The results are presented in Chapter 3.

1.4 Wave-wave interaction between the stationary Wave 1 and transient Wave 2

The eastward traveling Wave 2 is also vigorous in late winter (Fig. 1.3b). Its generation mechanism has been proposed. Linear stability analyses of an idealized polar-night jet showed that barotropic instability of the polar-night jet may cause the eastward traveling Wave 2 (e.g. Hartman 1983; Manney 1988). Manney et al. (1991a) investigated the behavior of the Wave 2 during winter and early spring for ten years from 1979 to 1988, and found that the regular eastward propagation of Wave 2 is evident only within the stratosphere and the zonal mean state frequently satisfies conditions for instability. A subsequent eigenvalue analysis (Manney et al. 1991b) reinforces that barotropic and baroclinic instabilities play an important role for the generation of the eastward traveling Wave 2.

Some phenomena related to the wave-wave interaction between the stationary Wave 1 and traveling Wave 2 have been reported (e.g. Mechoso et al. 1988: Manney et al. 1991a). Hirota et al. (1990) studied quasi-periodic amplification of Wave 1 in the SH stratosphere

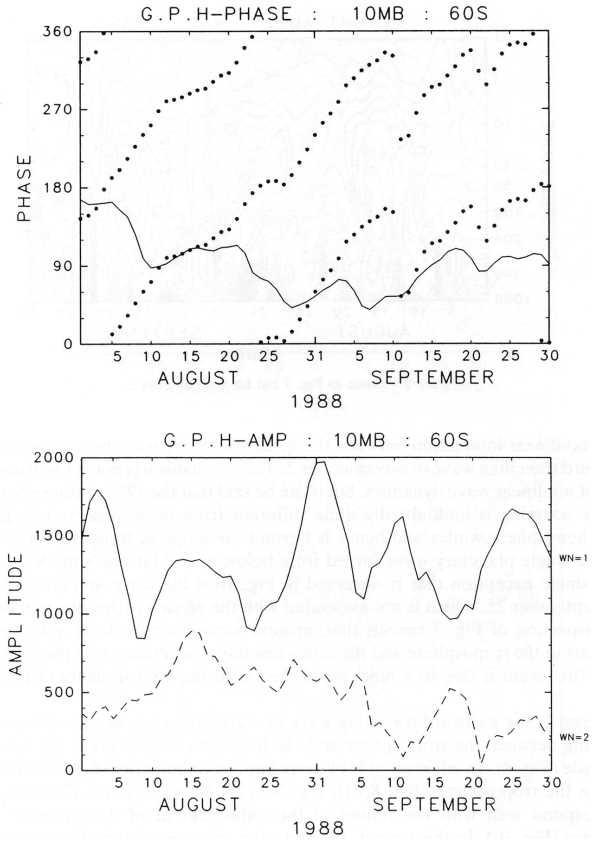

Figure 1.10: Phases (top) of geopotential height Wave 1 (solid line) and Wave 2 (dots) and Amplitudes of geopotential height Wave 1 (solid line) and Wave 2 (broken line) at 10 hPa and 60°S in August and September 1988. (From Hirota et al. 1990)

during August-September 1988 and found that Wave-1 amplitude reaches its maximum when the ridges of Waves 1 and 2 overlap as shown in Fig. 1.10. They also found such periodic variations were observed during late September and early November in 1983 and indicated that the wind structure in 1983 was peculiar because of the stronger meridional curvature of the westerly jet compared to other 5 years from 1979 to 1984 (Shiotani et al. 1990).

In contrast to the NH, the winter circulation in the SH is not highly nonlinear and weakly nonlinear dispersion theory is effective to investigate these periodic variations. These allow exchange of wave energy and enstrophy between the wavenumbers $\mathbf{k_1}$, $\mathbf{k_2}$, and $\mathbf{k_3}$ in triad of values which, with the corresponding frequencies ω_1, ω_2, and ω_3, satisfies

$$\mathbf{k_1} + \mathbf{k_2} = \mathbf{k_3} \tag{1.1}$$

$$\omega_1 + \omega_2 = \omega_3. \tag{1.2}$$

This relationship indicates that the stationary Wave 1 ($\mathbf{k_1} = (k, l)$, $\omega_1 = 0$) and the eastward traveling Wave 2 ($\mathbf{k_2} = (2k, l)$, $\omega_2 = \omega$) with the same latitudinal harmonics (l) can generate secondary waves, higher harmonic eastward traveling Wave 1 and Wave 3 ($\mathbf{k_3} = (k + 2k$ or $2k - k, 2l)$) with the same angular frequency as Wave 2 ($\omega_3 = \omega + 0$).

Equation (1.1) implies the importance to investigate spatial structure of the waves as well as their time variations to treat the wave-wave interaction. In previous studies to deal with the wave-wave interaction, variations in the phase and amplitude of the total wave are investigated. However, the waves should be divided into the stationary and transient components to observe the secondary wave satisfying Eq. (1.2). In this study, I investigate the wave-wave interaction between the stationary Wave 1 and traveling Wave 2 focusing on the meridional structure and the time change of the traveling Wave 1 using the observational dataset.

I also use a spherical barotropic model to grasp the fundamental characteristics of the wave-wave interaction, the periodicity and the meridional structure. Single layer spherical models have been used to examine stratospheric dynamics (e.g. Juckes and McIntyre 1987; Thuburn and Lagneau 1999). One of the good examples is the study by Rong and Waugh (2003). They examined internal variability of the polar vortex in a shallow water model with time independent topography for a range of topographic amplitude. For large topographic amplitude, there are breakdown and recovery cycles of the polar vortex and the filamentary structures are produced during the vortex breakdown due to highly nonlinear process. On the other hand, for small topographic amplitude, the only periodic undulation of the edge of the polar vortex is observed. Their results demonstrated that the horizontal structure of potential vorticity plays an important role in the vacillation of the stratospheric flow observed in the NH, though only the effect of the vertical structure had been emphasized in previous studies.

Ishioka and Yoden (1995) also investigated the nonlinear aspect of the polar vortex in the SH stratosphere using a spherical barotropic model without topography. In their model, the eastward traveling Wave 2 is generated due to the barotropic instability of the forced zonal flow and a vacillating solution in which the Wave 2 changes its amplitude periodically is obtained within a certain parameter range. I add the surface topography of zonal wavenumber 1 in their model and investigate the wave-wave interaction between the stationary Wave 1 forced by the topography and the eastward traveling wave 2 generated by the barotropic instability to elucidate the dynamical element to produce the periodic variations in the real stratosphere.

Using the same barotropic model, I investigate evolution of the polar vortex for a wide range of topographic forcing amplitude and jet profile in terms of the dynamics of wave-wave interaction. The effect of the wave-wave interaction in the NH stratosphere was evaluated in the 1980s by diagnosing the enstrophy budget averaged over high-latitudes and the spatial structure was not investigated (e.g. Smith 1983; Smith 1984; Robinson 1985) . However, the structure to satisfy Eq. (1.1) is one of the most important features for the wave-wave interaction. In this study, I analyze the meridional structure and temporal characteristics of each term of the enstrophy equation which is resolved into stationary and transient components to see the frequency relationship (Eq. (1.2)).

In Chapter 4, the quasi-periodic variations of the polar vortex are examined using the observational dataset and the barotropic model. The parameter sweep experiments with the barotropic model are shown in Chapter 5.

The results presented in this thesis have been submitted or in preparation for publication. Chapter 2 is based on Hio and Yoden (2004a), Chapter 3 on Hio and Hirota (2002), and Chapter 4 on Hio and Yoden (2004b). The results in Chapter 5, are now in preparation for submission.

Chapter 2

Stratospheric sudden warming in the year 2002

Abstract

Dynamical features of the interannual variations of the seasonal march in the Southern Hemisphere stratosphere are investigated with the NCEP/NCAR Reanalysis dataset from 1979 to 2002, and the unprecedented year 2002 in which a major stratosphere sudden warming occurred is characterized by comparing with the other 23 years.

A multiple empirical orthogonal function analysis of the stratospheric mean zonal wind and a composite analysis based on the principal component of the leading mode show that the interannual variations are characterized by early or late deceleration of the polar-night jet, which is well correlated with the variation of a time averaged upward EP flux in the lower stratosphere. The stronger wave activity in the lower stratosphere is associated with the earlier "shift-down" of the jet. The composite difference of the stratospheric mean zonal wind can be traced down to the lower troposphere in September and October. These features are consistent with the variations of the Southern Hemisphere annular mode, although the main disturbance to maintain the variations is different between the stratosphere and troposphere.

Some scatter diagrams show the extreme situation of the year 2002. It is far from the cluster of the other 23 years, but the large deviation in 2002 is consistent with the tendency of the fluctuations in the other years except for the extremeness.

2.1 Introduction

In September 2002, a major stratospheric sudden warming event occurred in the Southern Hemisphere (SH) and the polar vortex split into two for the first time since satellite observations of the stratosphere had begun. Midwinter warming events had been observed in 1988 (e.g., Kanzawa and Kawaguchi, 1990 ; Hirota et al. 1990), but they were minor ones. Planetary waves in the winter stratosphere were much more vigorous in 2002 compared with other years (Fig. 1.6). Rather periodic strengthening of the wave activity in August and early September corresponds to sequential occurrence of three minor warming events observed prior to the major warming event in late September. Enhancement of the wave activity can be traced back to the middle troposphere (Fig. 6 in Baldwin et al. 2003).

In this chapter, I consider these warming events as episodes in the seasonal march of the stratospheric circulation, and investigate interannual variations of the seasonal march to characterize the dynamical conditions in the unprecedented year 2002.

Shiotani et al. (1993) studied interannual variations of the seasonal march in the SH by characterizing 10 winters during the 1980s according to the location of the core of the polar-night jet in midwinter. They defined low-latitude-jet (LLJ) years and high-latitude-jet (HLJ) years. They showed that the timing of the poleward and downward shift ("shift-down") of the polar-night jet in late winter is earlier in the HLJ years than in the LLJ years and the planetary wave activity from autumn to late winter is also large in the HLJ years. Aoki et al. (1996) investigated interannual variations of the tropospheric circulation and its relation to the stratosphere by using a dataset for 15 years from 1979 to 1993. They showed that a zonal wind index, defined as the difference of the 300-hPa zonal mean zonal wind speed between 60°S and 40°S, is a sensitive indicator of two typical latitudinal profiles of the zonal mean zonal wind in the SH troposphere noted as the single-jet and the double-jet profiles, and found that the seasonal evolution of the zonal wind index from April to October is separated into two groups, DS years and SD years, where DS (SD) years are characterized by the double-jet (single-jet) in early winter and the single-jet (double-jet) in late winter. There is a correspondence between interannual variations in the seasonal march of the stratospheric polar-night jet and those of the tropospheric jet structure as listed in Table 2.1; DS years appear in LLJ years, while HLJ years appear in SD years.

A multiple empirical orthogonal function (EOF) analysis of the tropospheric and stratospheric circulation was performed by Kuroda and Kodera (1998) with a 16-year dataset to extract the interannual variations of the seasonal march from autumn to spring. The leading EOF is characterized by the poleward and downward shift of anomalous zonal mean zonal winds in the SH stratosphere, associated with anomalous propagation of planetary waves from the troposphere. The mode of the first EOF has a long time-scale of nearly half of a year through atmospheric wave-mean flow interactions.

Wave driving from the troposphere is also related to the mean meridional circulation. Fusco and Salby (1999) proposed that the planetary wave activity entering the lower stratosphere in the extratropics is a good dynamical proxy for the diabatic meridional circulation and showed that the interannual variations of the upward EP flux in high latitudes at 100 hPa are coherent with those of the tendency of the total ozone in the Northern Hemisphere (NH). Randel et al. (2002) investigated the space time patterns of this coherency in both hemispheres and showed that the high correlation moves from mid latitudes during winter to polar latitudes in spring. As to the polar temperature, Newman et al. (2001) demonstrated that in the NH, the upward EP flux at 100 hPa in mid to late winter (January-February) is highly correlated with the mean polar stratospheric temperature in March.

Following these studies, I investigate the interannual variations of the seasonal march

Table 2.1: Classification of 24 years (1979-2002) based on the PC1 of the seasonal march variation (Fig. 2.3) in this study and some other classifications of the interannual variations in the SH in the previous studies.
SSH: Shiotani et al. (1993), L: LLJ year, H: HLJ year
ASH: Aoki et al. (1996), D: DS year, S: SD year
This Study: E: ED year, L: LD year, e: positive PC1 smaller than the threshold value, l: negative PC1 larger than the threshold value
Naito: Naito (2002), W: Westerly phase of the QBO, E: Easterly phase of the QBO

Year	79	80	81	82	83	84	85	86	87	88	89	90
SSH		L	L	-	-	H	H	H	L	-	L	
ASH	-	D	D	S	-	S	S	S	-	S	D	S
This Study	E	l	l	e	l	l	L	E	L	E	l	L
Naito	E	W	E	E	E	E	W	E	W	E	E	W

Year	91	92	93	94	95	96	97	98	99	00	01	02
SSH												
ASH	D	S	D									
This Study	E	E	l	e	L	l	e	L	L	E	L	E
Naito	E	W	E	E	W	E						

in the stratosphere and their relation to the troposphere. I use the daily (12GMT) NCEP/NCAR reanalysis data for the 24-year period from 1979 to 2002 in order to characterize the unprecedented year 2002 in the whole analyzed years (see Kalnay et al., 1996 for details of the NCEP/NCAR reanalysis project and its products). The data are transformed into $5^\circ \times 5^\circ$ horizontal latitude and longitude mesh at 17 pressure levels (1000-10 hPa).

The present paper is organized as follows: In Section 2.2, year-to-year variations in the seasonal march of the stratospheric mean zonal winds and relation to the tropospheric circulation are described, and similarity or uniqueness of the circulation in 2002 is represented. Interannual variations related to the upward EP flux in the lower stratosphere are investigated in Section 2.3. Discussion is in Section 2.4, and conclusions in Section 2.5.

2.2 Interannual variations of the seasonal march

2.2.1 Zonal mean zonal wind and planetary waves in the stratosphere

Figure 2.1 shows the seasonal evolution of the climatological zonal mean zonal wind at 60°S, 20 hPa (thick solid line), along with the standard deviation of the interannual variability (shaded region). The mean zonal wind reaches its maximum in late August and interannual

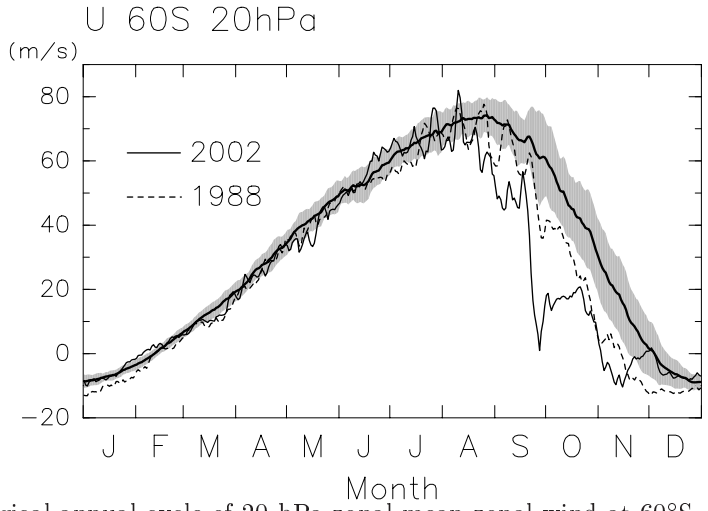

Figure 2.1: Climatological annual cycle of 20 hPa zonal mean zonal wind at 60°S, for 24 years from 1979 to 2002 (thick solid line), along with the standard deviation of its interannual variability (shaded). Thin solid (dotted) line denotes day-to day variations in 2002 (1988).

variability is large from August to November. In 2002 (thin solid line), the polar-night jet began to decelerate so early in August, and then the largest reduction occurred in late September, corresponding to the polar vortex split. Comparing with the seasonal march of 1988 (dotted line), the year in which the midwinter warming events occurred, we can recognize how the deceleration in 2002 was an extreme event.

I characterize interannual variations of the seasonal evolution by making a multiple EOF analysis (e.g. Kuroda and Kodera 1998) for the 24-year dataset, which is performed by combining 12 months of data in a vector $\mathbf{x}^i$ as

$$\mathbf{x}^i = (u^i(1),\ u^i(2),\ \cdots,\ u^i(12))^{\mathbf{T}}, \tag{2.1}$$

where $u^i(m)$ is the anomalous monthly averaged zonal mean zonal wind at 60°S, 20 hPa for the mth month of the ith year. The modes of the EOF are defined as the eigenvectors of the covariance matrix calculated from $\mathbf{x}^i$. The first mode (EOF1) shown in Fig. 2.2 represents interannual variation of the deceleration of the polar-night jet from September to December. PC1 explains as much as 66% of the total variance, so that it is safe to give attention to EOF1 only.

Both EOF1 and EOF2 are similar to those of the model experiment by Taguchi and Yoden (2002), their Fig. 7, though they used the stratospheric polar temperature as a measure of the polar vortex intensity instead of the mean zonal wind.

Figure 2.3 shows year-to-year variation of PC1 for the 24 years. In the year whose principal component of EOF1 (PC1) is positive (negative), the polar-night jet decelerates earlier (later) than the climatological seasonal march. The two largest PC1s for 2002 and 1988 reflect the large deceleration of the polar-night jet in August and September corresponding to the warming events. Absolute value of the most negative PC1 is not so

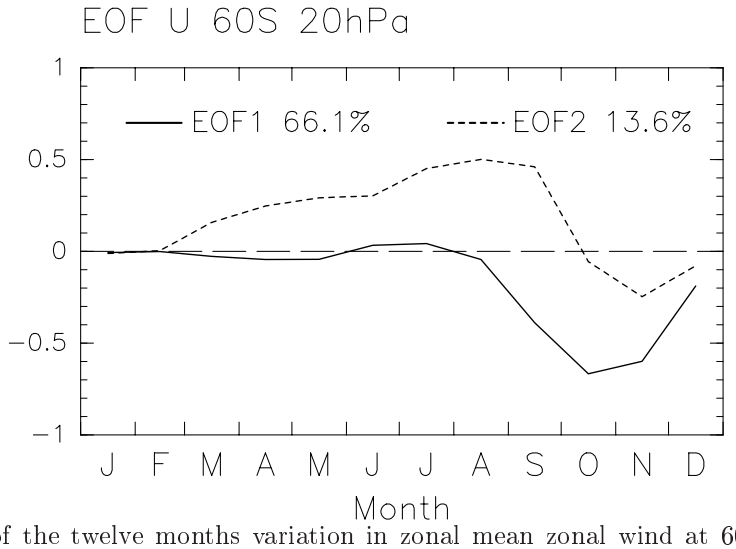

Figure 2.2: EOFs of the twelve months variation in zonal mean zonal wind at 60°S, 20 hPa from the climatological seasonal march on the basis of the covariance matrix of monthly averaged values for the 24-year dataset from 1979 to 2002.

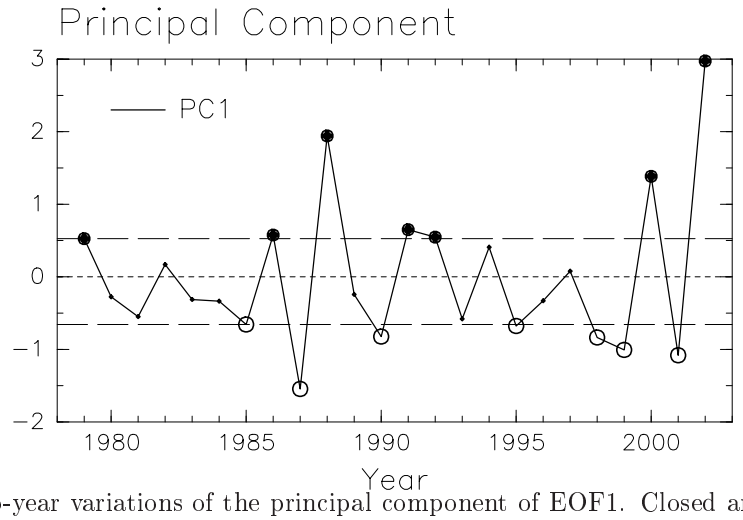

Figure 2.3: Year-to-year variations of the principal component of EOF1. Closed and open circles denote Early-Deceleration (ED) years and Late-Deceleration (LD) years, respectively. Dashed lines indicate the thresholds to determine the ED and LD years.

large as the most positive one (only −1.5 for 1987), and the frequency distribution of PC1 has some skewness as shown in Table 2.2. To capture the associated interannual variations in some dynamical fields in the stratosphere and troposphere, I make a composite analysis for two groups defined with the value of PC1; Early-Deceleration (ED) years and Late-Deceleration (LD) one. Here ED (LD) consists of the years of seven largest (smallest) PCs, indicated by closed (open) circles in Fig. 2.3. The horizontal dashed lines are the threshold values for the definition, PC1= 0.53 and −0.66.

A composite analysis for ED and LD years is done after applying a 31-day running mean for smoothing. Figure 2.4 (top) shows the composite seasonal evolutions of the zonal

Table 2.2: Normalized frequency distributions (in %) with each standard deviation σ of PC1, the zonal mean zonal wind at 45°S (U), 20 hPa averaged for October 1-15 for the 24 years (1979-2002) in this study, and the 1,000-year middle stratospheric polar temperature in August obtained by Taguchi and Yoden (TY) (2002) with a troposphere-stratosphere coupled model corresponding to the SH. The distribution of the zonal mean zonal wind is multiplied by -1 for dynamic consistency with the other distributions. Gaussian frequency distribution is also shown for comparison.

	-3σ	-2σ	-1σ	0	1σ	2σ	3σ	4σ	5σ	6σ
PC1	0.0	12.5	45.8	29.2	8.3	4.2	0.0	0.0	0.0	
U	4.2	4.2	58.3	20.8	8.3	0.0	4.2	0.0	0.0	
TY	0.3	8.7	47.7	32.8	7.0	1.8	1.1	0.2	0.2	
Gaussian	2.1	13.6	34.1	34.1	13.6	2.1	0.1	3×10^{-3}	-	

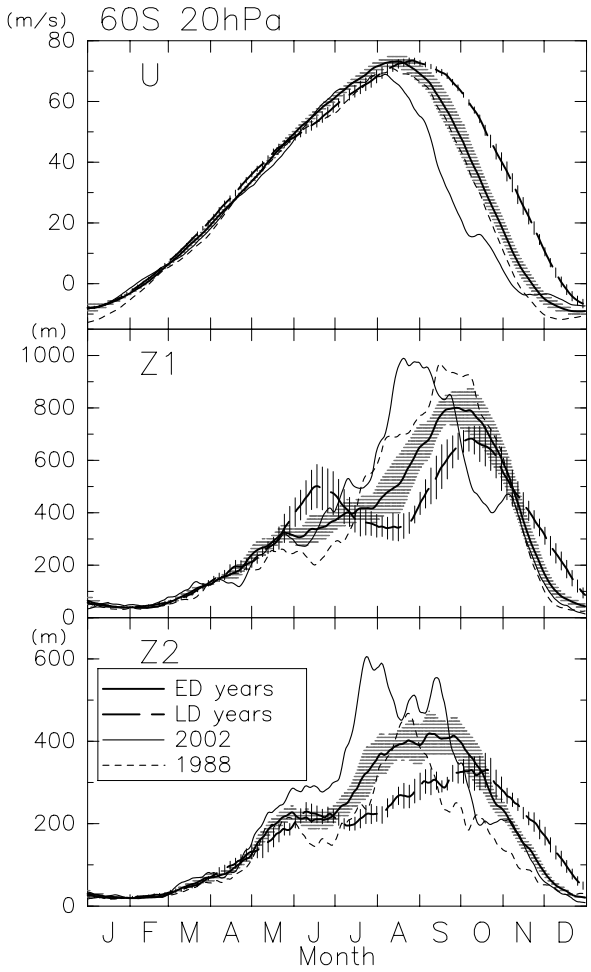

Figure 2.4: Time series of the composites for ED years (thick solid lines) and LD years (thick dashed lines) of the zonal mean zonal wind at 20 hPa, 60°S (top), and 20 hPa geopotential amplitude of Wave 1 (middle) and Wave 2 (bottom) at 60°S, along with the ±0.5 times standard deviation (shade region for ED years and vertical bars for LD years). Thin solid line and dotted line denote the time series for 2002 and 1988, respectively. A 31-day running mean is applied to each quantity beforehand.

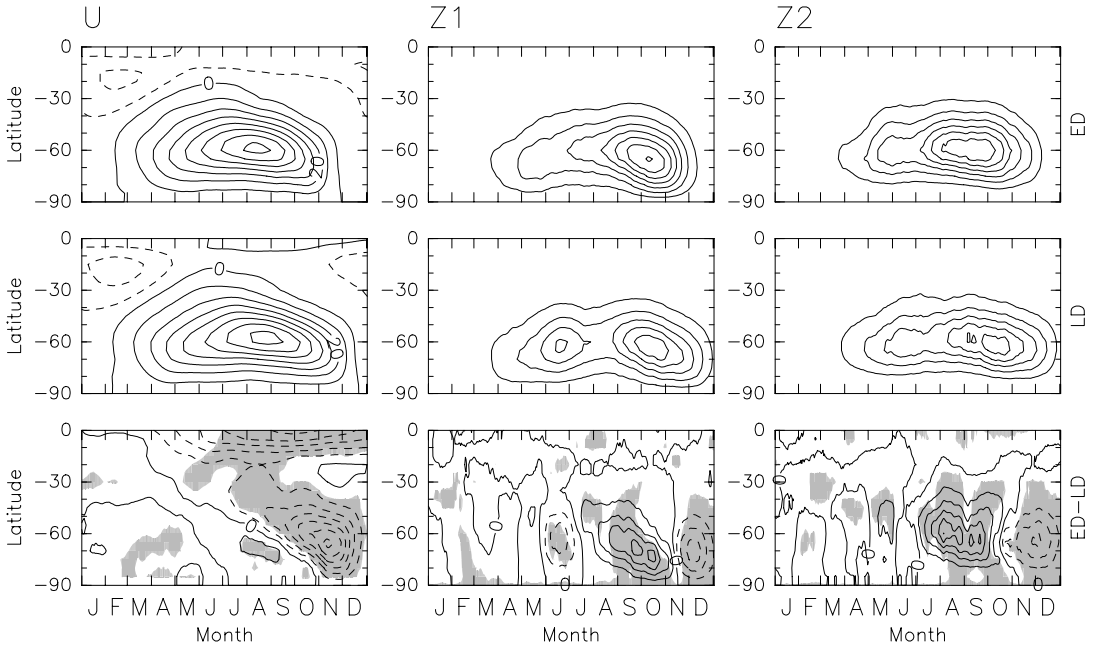

Figure 2.5: Latitude-time sections of the zonal mean zonal wind (left) and geopotential height amplitude of Wave 1 (center) and Wave 2 (right) for the composites of ED years (top) and of LD years (middle), and the differences between the two groups (bottom). Dotted contours denote negative values. Areas where the statistical significance of the difference is larger than 90 % based on the t-test are shaded in the bottom panels. Contour intervals for the mean zonal wind are 10 ms^{-1} (top and middle) and 4 ms^{-1} (bottom). Contour intervals of the amplitude of Wave 1 are 120 m (top and middle) and 60 m (bottom), while those of the amplitude of Wave 2 are 60 m (top and middle) and 30 m (bottom). A 31-day running mean is applied to each quantity beforehand.

mean zonal wind at 60°S, 20 hPa for ED (thick solid line) and LD (thick dashed line) years. Shaded regions show the ranges of ± 0.5 times standard deviation for each group. When these regions do not overlap, the difference between the two groups is significant at more than 90% based on the t-test. The difference in deceleration of the polar-night jet is highly significant from September to December. The zonal mean zonal wind for 2002 (thin solid line) is much weaker already in August, even if it is compared with the composite for ED years.

Figure 2.5 (left) displays latitude-time sections of the composite mean zonal wind at 20 hPa for ED years (top), LD years (middle) and the composite difference (bottom). The polar-night jet in ED years is weaker on the equatorward flank of the jet in August and shifts poleward earlier than that in LD years. As the result, the negative composite difference in mid latitudes moves poleward together with the polar-side positive one from August to October. The large negative difference in November and December reflects the difference in the timing of the shift to summer circulation. There is a significant difference in low latitudes from July to December. The composite mean zonal wind is easterly in ED years and westerly in LD years. Its association with the quasi-biennial oscillation (QBO) of the equatorial mean zonal wind will be discussed later. Note also the significant difference

in March and April in high latitudes.

Composites of time evolution of the geopotential amplitude of zonal wavenumber 1 (Wave 1) at 60°S, 20 hPa for ED and LD years are shown in Fig. 2.4 (middle). Latitude-time sections of the Wave 1 amplitude at 20 hPa for each group and their difference are also shown in Fig. 2.5 (center). The amplitude of the Wave 1 for LD years has two maxima in early winter and in spring, which are well known feature in the SH. On the other hand, that for ED years has one maximum in spring; the maximum amplitude is larger and appears earlier. In both groups, the location of the amplitude peak moves poleward from September to November along with the shift of the polar-night jet. The composite difference also shows poleward movement of positive values from late July to early November. Statistically significant difference is also seen in June in high latitudes.

Similar features are seen in the amplitude of Wave 2 as shown in Fig. 2.4 (bottom) and Fig. 2.5 (right). ED years have larger amplitude in August and September, while smaller one in November and December.

As to the year 2002 shown in Fig. 2.4 with the thin solid line, Wave 2 amplified sharply in July, and then Wave 1 amplified in August. Both amplitudes are much larger even if compared with the composite for ED years. The amplitude of Wave 1 in 1988 (dotted line) is very large in September, though that of Wave 2 is not so large except for August.

2.2.2 Composite differences of the zonal mean zonal wind and wave activity in the stratosphere and troposphere

Contours in Fig. 2.6 denote latitude-height sections of the composite difference in monthly averaged zonal mean zonal wind between ED and LD years for nine months from April to December. Significant differences are found as early as in May around 30°S above 30 hPa. The dipole pattern moves poleward and expands downward in the stratosphere from June to October. This month-to-month variability corresponds to the earlier shift-down of the polar-night jet in ED years. The difference in the zonal mean zonal wind is largest in November, over 24 ms^{-1} at 65°S, 20 hPa. Significant differences in the troposphere are also seen from August to December. The mean zonal wind around 60°S is weaker over 3 ms^{-1} in ED years in the upper troposphere in September and October and in the whole troposphere in November and December. On the other hand, that around 35°S is significantly stronger in ED years from September to November. In low-latitudes, the difference of the mean zonal wind between ED and LD years is negative in the middle stratosphere, suggesting that the QBO phase at these levels tends to be easterly (westerly) for the ED (LD) years.

The composite difference of the monthly averaged EP flux is also shown in Fig. 2.6 with arrows, which are drawn only at the positions where the difference in either component is statistically significant at 90% level. From July to October, the upward EP flux for ED years is larger in the high-latitude stratosphere. This is consistent with the difference in the geopotential amplitudes of Wave 1 and Wave 2 shown in Figs. 2.4 and 2.5. Along with the

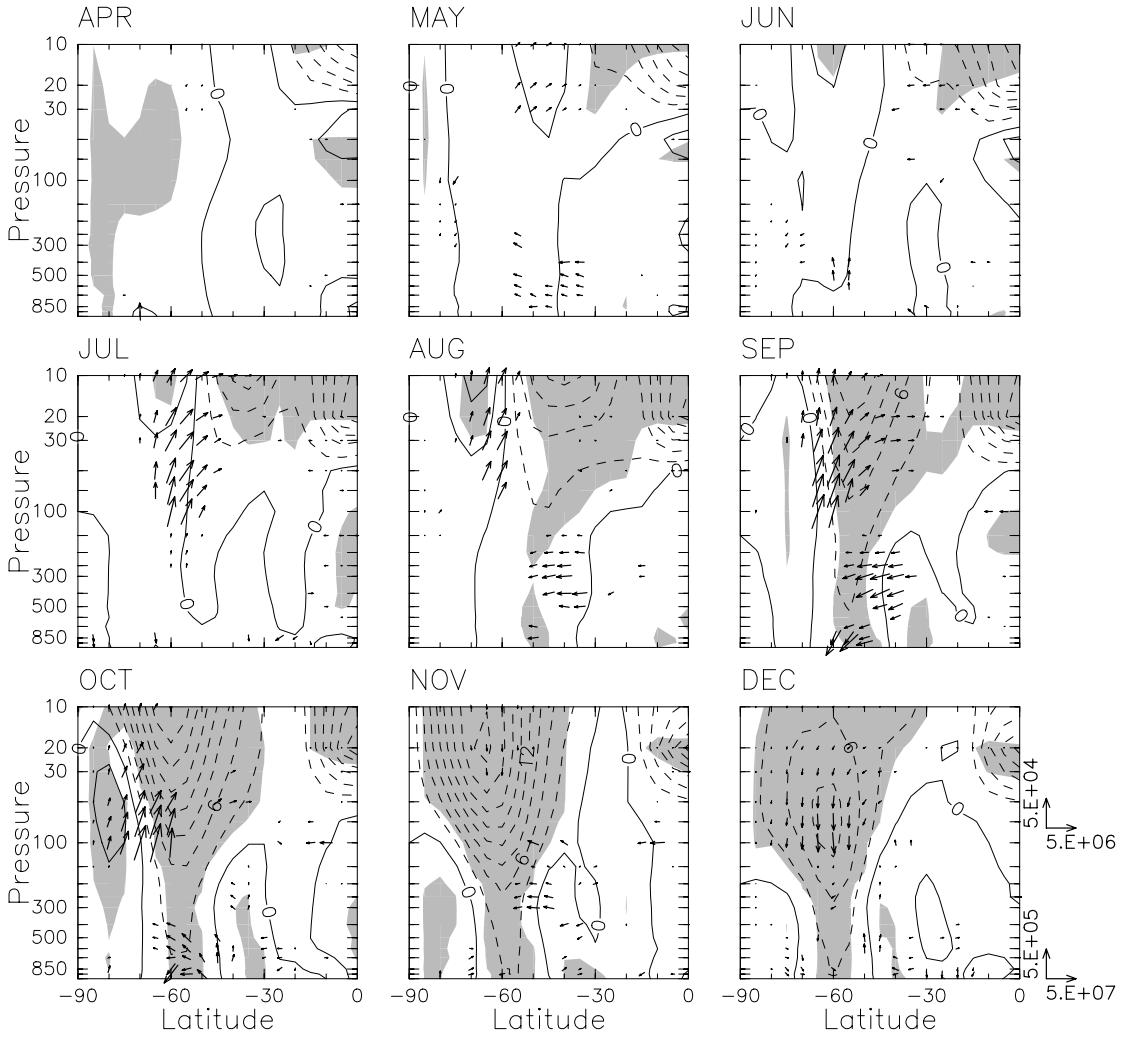

Figure 2.6: Latitude-height sections of composite difference of the monthly averaged zonal mean zonal wind between ED and LD years for nine months from April to December. The contour interval is 3 ms^{-1} and dotted contours denote negative values. Areas where the statistical significance of the difference is larger than 90% based on the t-test are shaded. Composite difference of the EP vectors is also drawn by an arrow at the location where the significance level of the difference in either component is above 90 %. The length of the unit vector is displayed on the right-hand-side of the graph for December. The scaling of the unit vector below 100 hPa is ten times as large as that above 100 hPa.

earlier evolution of the polar-night jet, the difference of the EP flux also moves poleward and downward. Equatorward EP flux in the mid-latitude upper troposphere is weaker in ED years in August and September, and synoptic-scale waves are mostly responsible for this difference (not shown). Significant difference in the EP flux is also seen in the mid-latitude lower troposphere in September and October. The composite difference in the mean zonal wind in the troposphere is mainly associated with the difference in the EP flux by synoptic-scale waves.

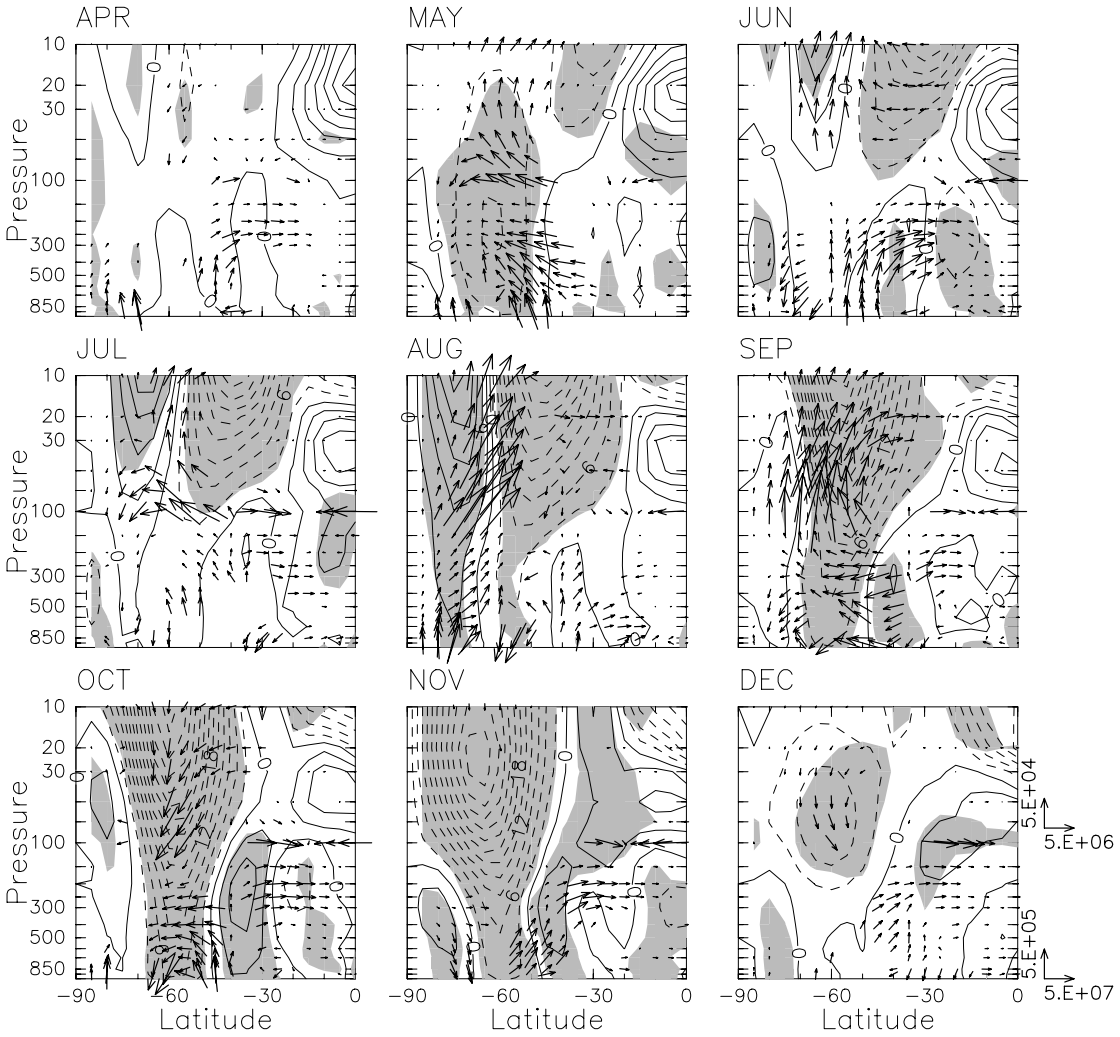

Figure 2.7: Latitude-height sections of the difference of the monthly averaged zonal mean zonal wind between 2002 and LD years (2002 − LD) for nine months from April to December. The contour interval is 3 ms^{-1} and dotted contours denote negative values. Shaded regions correspond to the areas where the anomaly is greater than the 1.5 times standard deviation of LD years. Composite difference of the EP vectors is also drawn by an arrow. The length of the unit vector is displayed on the right-hand-side of the graph for December. The scaling of the unit vector below 100 hPa is ten times as large as that above 100 hPa.

2.2.3 Characterization of the year 2002

Differences of the monthly averaged zonal mean zonal wind and the monthly averaged EP flux in 2002 from the composite for LD years are shown in Fig. 2.7 for nine months from April to December. Many of the patterns of the differences resemble those between ED and LD years (Fig. 2.6). A poleward movement of the dipole pattern in the stratospheric mean zonal wind is also seen from June to September with much larger values, which is accompanied with a much larger upward EP flux in the stratosphere. Particularly, the dipole pattern in August expands down into the high-latitude troposphere, and the upward EP flux is also larger in the polar region of the whole troposphere where the mean zonal

wind is stronger. In October and November, the difference of the mean zonal wind is much larger compared with those in Fig. 2.6, indicating much earlier seasonal march in 2002. Note that in October the difference of the EP flux is downward in the stratosphere showing the weaker upward flux in 2002, which is consistent with the smaller amplitudes of Wave 1 and Wave 2 in 2002 as shown in Fig. 2.4.

The differences of the tropospheric mean zonal wind from August to November are also larger than those in Fig. 2.6. In accord with these differences, the difference of the vertical component of the EP flux in the lower troposphere is upward around 50°S and downward around 70°S in September, October and November. In low latitudes, the differences of the stratospheric mean zonal wind have the opposite sign from those in Fig. 2.6, and shift downward from April to December. This reflects that the QBO phase of the equatorial mean zonal wind is westerly in 2002 while it tends to be easterly in ED years. I shall come back to these in more detail in Discussion.

It is also notable that the mean zonal wind in high latitudes in May is weaker in 2002 both in the troposphere and the lower stratosphere with the largest difference in the upper troposphere, associated with the poleward and upward EP flux anomaly in the same region.

2.3 Relation to the upward EP flux in the lower stratosphere

2.3.1 Correlation of the upward EP flux to the zonal mean zonal wind

Figure 2.8 shows the seasonal evolution of the climatological upward EP flux at 100 hPa averaged over 45°-75°S (thick solid line) along with the standard deviation of the interannual variability (shaded region). The climatological EP flux has a maximum in late September and interannual variations are large through winter and spring. In 2002 (thin solid line), the upward EP flux is very large in August and September, while small in October. These features were already pointed out with the differences of the EP vectors shown in Fig. 2.7. In 1988 (dotted line), the larger upward EP flux compared with the climatology is seen in July and August, though it is not so large as that in 2002. The upward EP flux at 100 hPa between 45°S and 75°S is used as a proxy of the wave activity in the lower stratosphere to investigate the relation to some dynamical fields in the stratosphere and troposphere. Figure 2.9 shows correlations of the 24-year time series of the zonal mean zonal wind averaged for the first 15 days of each month with the upward EP flux in the lower stratosphere during the preceding 45 days for nine months from April to December. This average period for the EP flux is the same as that used in Newman et al. (2001), which was determined based on the thermal damping rate in the middle stratosphere. The correlations which exceed ±0.4 (0.65) are significant at the 95% (99.9%) level for 24 data

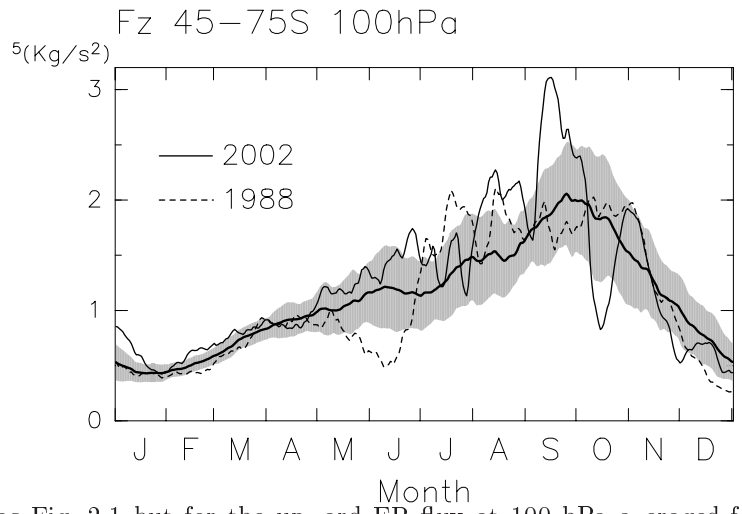

Figure 2.8: Same as Fig. 2.1 but for the upward EP flux at 100 hPa averaged for 45°-75°S. A 31-day running mean is applied to each quantity beforehand.

values, and are lightly (heavily) shaded in the figure. From July to September, strong negative correlations are found in the equatorward flank of the climatological core of the polar-night jet and positive ones in the poleward frank. This dipole pattern moves poleward and downward with the seasonal shift of the climatological polar-night jet, indicating that the stronger wave activity in the lower stratosphere is associated with the earlier shift-down of the polar-night jet. The significant positive correlations in the polar stratosphere disappear in October, while the negative correlations spread in mid and high latitudes in November and December. In the troposphere a dipole pattern with positive correlations in the poleward frank of the subtropical jet and negative ones in the equatorward frank is found in October; this relation suggests the larger (smaller) upward EP flux in the lower stratosphere in late August and September is related with the poleward (equatorward) shift of the subtropical jet in October.

The patterns of the correlation in the stratosphere from July through November are similar to those of the composite difference of the zonal mean zonal winds between ED and LD years shown in Fig. 2.6. This means that the EP flux in the lower stratosphere is a good indicator of the interannual variations in the seasonal march of the stratospheric circulation in the SH through winter and spring. Large negative correlations are found on the equatorward of the core of the polar-night jet, even in the formation stage of the jet from May to June.

2.3.2 Scatter diagrams to characterize the year 2002

The upper left panel of Fig. 2.10 shows a scatter diagram for the pair that gives the maximum correlation in the stratosphere during the nine months shown in Fig. 2.9 (at the point marked with a cross). The upward EP flux averaged over the period from August 16

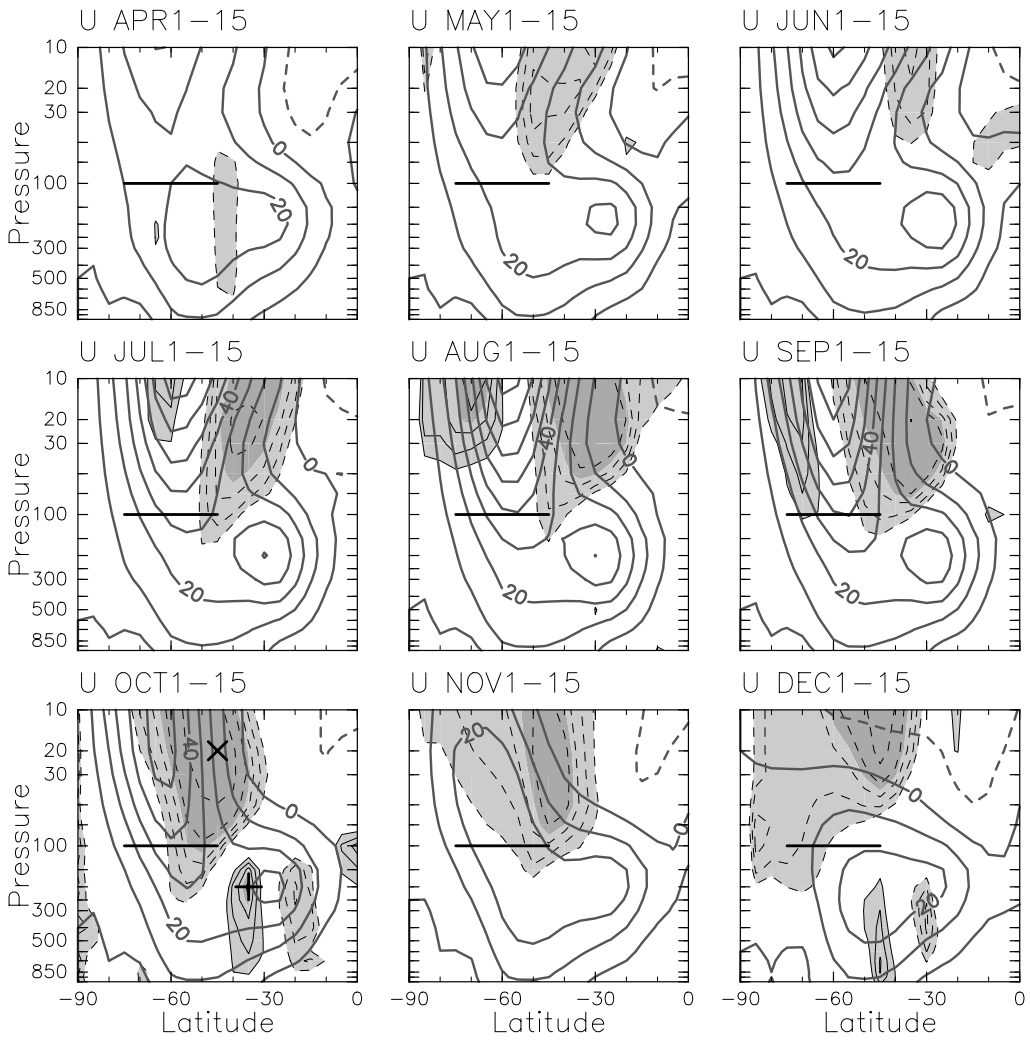

Figure 2.9: Correlation of the 24-year time series of the zonal mean zonal wind averaged for the first 15 days of each month with the upward EP flux at 100 hPa for 45°-75°S during the period preceding 45 days for nine months from April to December. Thin line contours are drawn above 0.4 or below −0.4 with an interval 0.1 and values over ±0.4 (0.65) are lightly (heavily) shaded. Dotted contours denote negative values. Climatological zonal mean zonal wind averaged for the same first 15 days is superimposed with thick gray lines. The contour interval for the mean zonal wind is 10 ms^{-1}.

to September 30 is plotted against the zonal mean zonal wind at 45°S, 20 hPa averaged for October 1-15 for the 24-year data. The correlation with the stratospheric mean zonal wind is very high whether the year 2002 is included for the calculation ($r = -0.86$) or not (-0.73). For these periods in 2002, the mean zonal wind is easterly and the upward EP flux in the lower stratosphere is extremely large compared with the other 23 years.

Now a confidence ellipse is introduced in the assumption of the bivariate normal distribution (see Wilks 1995) to characterize the year 2002. The solid-line ellipse denotes 90% confidence limit for the full dataset with the year 2002, while the dotted-line one for the other 23 years without 2002. The major and minor axes of the confidence ellipses are oriented in the direction of the first and second eigenvectors of the variance-covariance

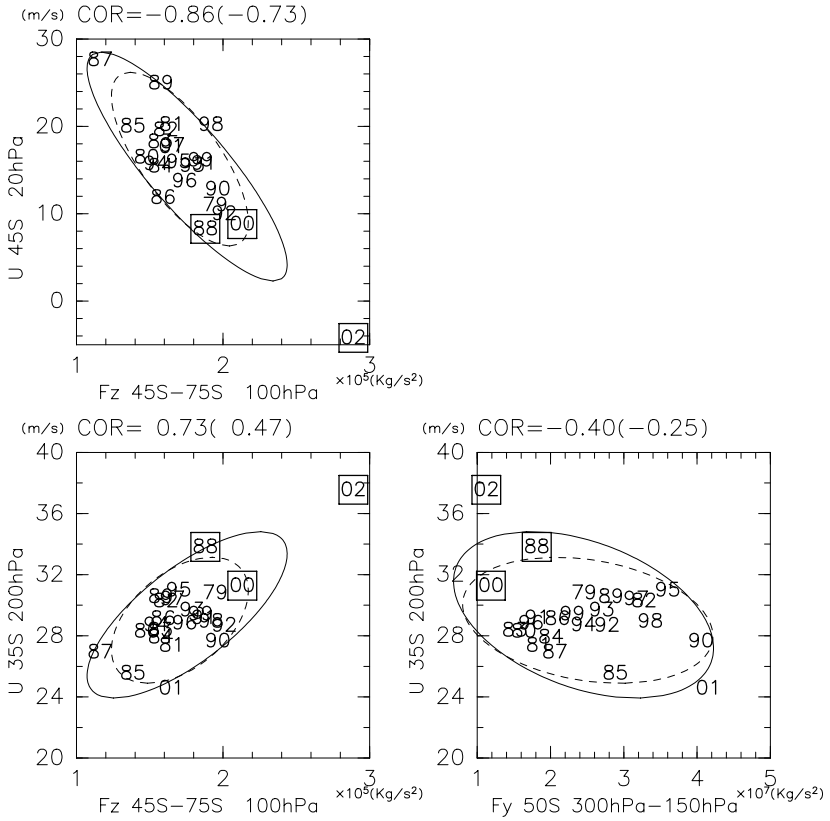

Figure 2.10: Scatter diagrams between the upward EP flux at 100 hPa averaged for 45°-75°S and the zonal mean zonal wind at 45 °S, 20 hPa (upper panel), between the same upward EP flux and the zonal mean zonal wind at 35 °S, 200 hPa (lower left panel), and between this tropospheric mean zonal wind and the horizontal EP flux at 50 °S averaged for 300-150 hPa (lower right panel). The time-averaging period for the mean zonal winds is 15 days from October 1 to October 15, while that for the EP fluxes is 45 days from August 16 to September 30. Two values above each panel are the correlation for the 24 years and for the 23 years without 2002 (written in parentheses). The solid-line (dotted-line) ellipse denotes 90% confidence limit for the 24 years (the 23 years).

matrix, respectively, and are stretched in these directions by an amount proportional to the square roots of the respective eigenvalues. That is, when the correlation between the two quantities is so high that the first eigenvalue is much larger than the second one, the ellipse is stretched much more along the major axis. The stretched ellipses in the upper panel of Fig. 2.10 are another description of the high correlation between the upward EP flux in the lower stratosphere and the stratospheric mean zonal wind. The confidence ellipse is stretched more in the almost same direction when the year 2002 is included for calculation, even though the year 2002 is outside of both confidence ellipses. These features indicate that the point for 2002 is far from the clusters of the other 23 years satisfying the fundamental relationship obtained from the other years.

In Fig. 2.9, another peak of the correlation of the 45-day averaged upward EP flux with the mean zonal wind averaged for the following 15 days is found in the troposphere at the point marked with a plus sign. The lower left panel of Fig. 2.10 is the scatter diagram

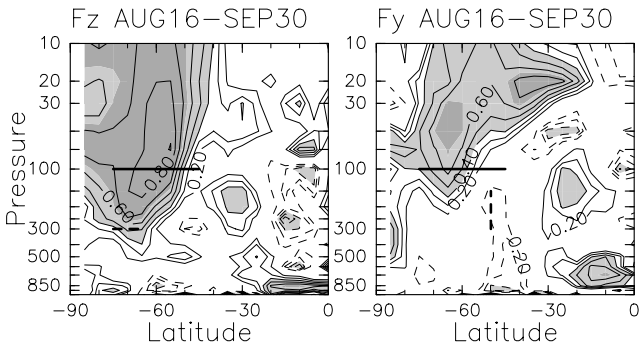

Figure 2.11: Correlation of the 24-year time series of the upward (left) and equatorward (right) EP flux averaged 45-day period from August 16 to September 30 with the upward EP flux at 100 hPa for 45°-75°S for the same period. Contours are drawn above 0.2 or below −0.2 with an interval 0.1 and values over ±0.4 (0.65) are lightly (heavily) shaded. Dotted contours denote negative values.

for the EP flux in the lower stratosphere and the mean zonal wind at 35°S, 200 hPa. The correlation is high ($r = 0.73$) for the full dataset. If the year 2002 is excluded from the calculation, the correlation is reduced to 0.47 but the confidence ellipse does not change the angle of the major axis. Both of the EP flux and the mean zonal wind are largest in 2002 in the 24 years.

Figure 2.11 shows the correlation map of the vertical component (left) and the horizontal component (right) of the EP flux with the upward EP flux at 100 hPa between 45°S and 75°S for the same period from August 16 to September 30. Both components highly correlate over a wide area in the stratosphere with the largest value along 60°S for the vertical component and in lower latitudes at 20 hPa level for the horizontal component. This means that the propagated EP flux converges in the middle stratosphere at the lower latitudes, which is consistent with the result shown in Fig. 2.9 that the maximum correlation of the mean zonal wind to the upward EP flux at the 100 hPa between 45°S and 75°S is located on the equator side of the reference latitudes of the upward EP flux.

A scatter diagram of the horizontal EP flux at 50°S in the upper troposphere averaged between 300 hPa and 150 hPa and the tropospheric mean zonal wind at the same position as used in the lower left panel is shown in the right panel of Fig. 2.10 to see more direct relationship in the upper troposphere. The height range for the averaged horizontal EP flux is shown in Fig. 2.11 with the dashed line where the equatorward EP flux is weakly correlated with the upward EP flux at 100 hPa. The tropospheric equatorward EP flux at the poleward side of the subtropical jet has negative correlation with the tropospheric mean zonal wind, though it is not highly significant. The year 2002 is outside of both confidence ellipses, representing the uniqueness of this year: The equatorward EP flux is smallest, while the mean zonal wind is strongest.

In these scatter diagrams, we can see the extreme situation of the year 2002. The points

for 2002 are far from the clusters of the other 23 years and outside of the 90% confidence ellipses. As to the relationship between the upward EP flux and the mean zonal wind, angles of the major axis of the confidence ellipses for the full 24 years are almost the same as those for the 23 years without the year 2002, indicating that the large deviations in 2002 are consistent with the tendency of fluctuations in the other years.

Note that other two years whose PC1 is very large in Fig. 2.3 (that is, 1988 and 2000) are also found on the same side as the year 2002; large upward EP flux in the lower stratosphere, weak mean zonal wind in the stratosphere, strong mean zonal wind in the upper troposphere, and small equatorward EP flux in the upper troposphere.

2.4 Discussion

Shiotani et al. (1993) introduced HLJ and LLJ years based on the location of the polar-night jet in midwinter and pointed out some relevance to the timing of the deceleration of the polar-night jet in late winter, such that the jet decelerates earlier in HLJ years than in LLJ years. LLJ years appear in LD years defined in this paper. However, the correspondence of ED years to HLJ years is not clear as shown in Table 2.1. On the other hand, the leading mode of the multiple EOF for the variations of the seasonal march obtained by Kuroda and Kodera (1998) reveals very similar features as our composite difference between ED and LD years shown in Fig. 2.6. It is basically the year-to-year variation of the timing of slow poleward and downward shift of the polar-night jet during winter.

The composite difference of the zonal mean zonal wind at 20 hPa (Fig. 2.5) shows the significant difference in the equatorial wind from July to December. It is easterly (westerly) in ED (LD) years. This relation reminds us of the result of a composite analysis by Naito (2002) based on the QBO phase of the equatorial mean zonal wind in July averaged between 20 hPa and 30 hPa for the 17 years from 1979 to 1996. Figure 2 in her paper resembles our left-bottom panel in Fig. 2.5, and the time series of the QBO category listed in Table 1 has a good correspondence with our time series of ED or LD years. However, such a correspondence is less clear for the recent years since 1997. In the year 2002, the QBO category is westerly, although the seasonal march is much earlier than the other 23 years.

In Section 2.2, it was found that the tropospheric EP flux anomalies as well as the stratospheric ones show the significant difference between the year 2002 and the average for LD years (Fig. 2.7). Here I note the horizontal scale of waves to make the difference by decomposing the EP flux into each wavenumber component. As to the difference of the upward EP flux in August, Wave 1 is responsible for the large positive anomaly around 80°S, indicating that vigorous Wave 1 in the stratosphere in 2002 is generated in the lower troposphere at fairly high latitudes. On the other hand, EP flux anomalies in the lower and middle troposphere in October and November are largely due to synoptic-scale waves. The active latitudes of the synoptic-scale waves shift equatorward in 2002 compared with

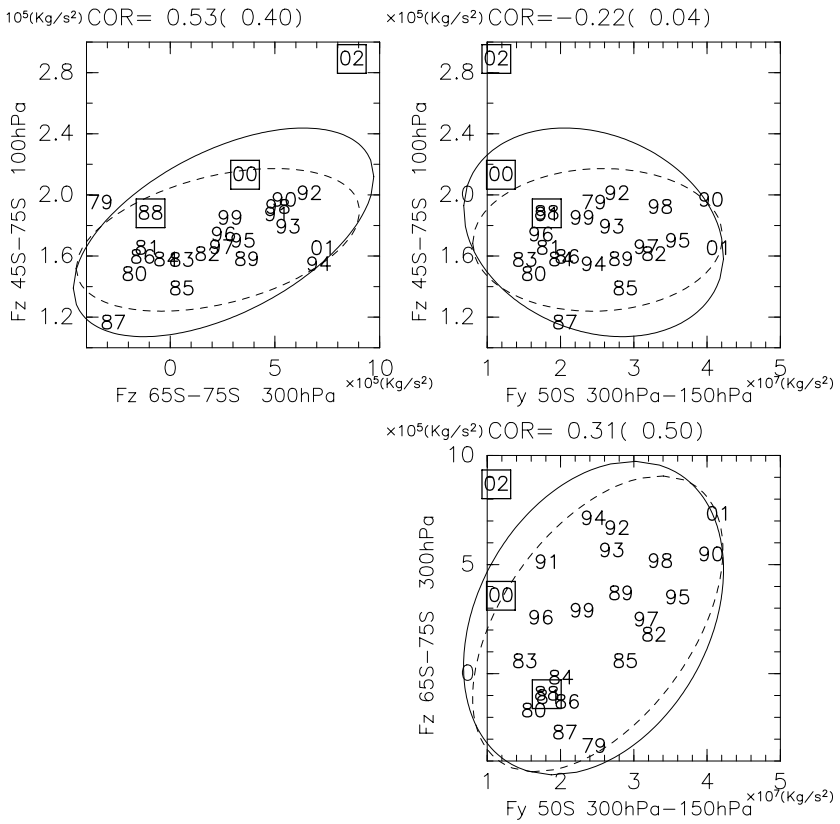

Figure 2.12: Same as Fig. 2.10 but for the combinations of the upward EP flux at 100 hPa averaged for 45°-75°S and that at 300 hPa averaged for 65°-75°S (upper left panel), the upward EP flux at 100 hPa and the equatorward EP flux at 50°S averaged for 300-150 hPa (upper right panel), and the tropospheric upward EP flux and the tropospheric equatorward EP flux (lower right panel). The time-averaging period is 45 days from August 16 to September 30.

those in LD years, while the location of the tropospheric jet shifts poleward.

These features about the tropospheric jet and synoptic-scale waves are consistent with the previous studies about the zonal flow vacillation in the SH troposphere (e.g., Karoly 1990; Hartmann and Lo 1998). Limpasuvan and Hartmann (2000) also showed that the SH annular mode (SAM) is maintained by the momentum flux anomaly of synoptic-scale eddies. The SAM in the stratosphere, which is associated with the upward EP flux propagating into the stratosphere, extended down into the troposphere in October 2002 (Fig. 7 in Baldwin et al. 2003). The SAM in the troposphere was maintained mainly by the horizontal EP flux anomaly due to the synoptic-scale waves as described above. The present result suggests that the main disturbance to maintain the SAM is different between the stratosphere and the troposphere, even though we sometimes regard the SAM as a single "mode".

The correlation map shown in Fig. 2.11 indicates that the variations of the upward EP flux in the lower stratosphere have some association with those of wave activity in the troposphere. In the upper panels of Fig. 2.12, the scatter diagram of the EP flux at the

100 hPa level between 45°S and 75°S with the tropospheric vertical component (left) or the horizontal component (right) of the EP flux are shown; the upward EP flux at 300 hPa between 65°S and 75°S or the equatorward EP flux at 50°S between 300hPa and 150 hPa (described as the dashed lines in Fig. 2.11). The upward EP flux in the upper troposphere in 2002 is the largest, while the equatorward EP flux in 2002 is the smallest compared with the other 23 years. As the result, the year 2002 is isolated from the other years in both of the scatter diagrams. The difference in the orientation angle of the confidence ellipses with and without the year 2002 also shows the uniqueness of 2002. The scatter diagram of the equatorward EP flux with the upward EP flux in the upper troposphere (the lower panel of Fig. 2.12) shows significant correlation ($r = 0.50$) for the 23 years from 1979 to 2001. However, the year 2002 is far from this relationship, which is located near the minor axis rather than the major one of the confidence ellipse for the other 23-year dataset, and correlation coefficient is reduced to 0.31 if this year is included for the calculation. Further study on the interannual variations in the troposphere which are related to the upward EP flux in the lower stratosphere, as the analysis on hemispheric geopotential-height patterns done by Salby and Callaghan (2002) for the NH, will be important to make clear what kind of disturbances in the troposphere modulates the upward EP flux in the lower stratosphere.

Frequency distribution of the PC1 score (Fig. 2.3) for the 24 years shows positively skewed distribution as listed in Table 2.2. Similar distribution (with opposite sign) is obtained for the mean zonal wind in the stratosphere. Taguchi and Yoden (2002) also obtained highly skewed distribution of the polar temperature in the upper stratosphere for the months through winter and spring in the 1,000-year integrations of a simple troposphere-stratosphere coupled model corresponding to the SH. A large number of the sampling guarantees the non-Gaussian distribution, and about 0.2 % of the 1,000 years are extremely warm with a monthly temperature anomalies exceeding 5 times standard deviation. The skewed probability distribution requires careful treatment in the statistical arguments of the rarity. Here caution is necessary on the skewness of the observed data, because of the small sample number. Correlation analysis with a small number of the sampling also requires careful treatment; the correlation coefficients in some scatter diagrams in Figs. 2.10 and 2.12 change drastically by excluding the year 2002 from the calculation.

2.5 Conclusions

A major stratospheric sudden warming event occurred in September 2002 for the first time in the Southern Hemisphere (SH) since satellite observations of the stratosphere had begun. I investigated the interannual variations in the SH for the 24 years from 1979 to 2002, in terms of the seasonal evolution and the troposphere-stratosphere coupling, and characterized the dynamical features of the unprecedented year 2002 by comparing with the other 23 years.

Interannual variations of the seasonal march were extracted with a multiple EOF anal-

ysis of the zonal mean zonal wind in the stratosphere. The leading mode explains the variations in the timing of the deceleration of the polar-night jet (Fig. 2.2). I defined two groups, Early-Deceleration (ED) years and Late-Deceleration (LD) years, according to the value of the principal component of EOF1 (Fig. 2.3), and made a composite analysis.

The seasonal march characterized by the poleward and downward shift of the polar-night jet from winter to spring is earlier in ED years as shown in Figs. 2.4, 2.5 and 2.6. The amplitude of the planetary waves in late winter is also larger for ED years in consistent with the wave-mean flow interaction theory. The weaker mean zonal wind in the high-latitude stratosphere in ED years, which is associated with the stronger upward EP flux in the stratosphere, can be traced down into the lower troposphere in September and October (Fig. 2.6). The location of the subtropical jet and the horizontal EP flux in the mid-latitude troposphere also show some difference between ED and LD years.

These features are consistent with the variations of the SH annular mode. However, the main disturbance to maintain the variations is different between the stratosphere (planetary waves) and the troposphere (synoptic-scale waves). The present results were also compared with some previous studies about the interannual variations of the SH (Table 2.2). The longer data set shows less clear relation with the QBO of the equatorial mean zonal wind.

In 2002, the upward EP flux in the lower stratosphere was much larger in August even compared with the other ED years and the large wave driving caused the earlier and larger deceleration of the mean zonal wind in the stratosphere (Figs. 2.7 and 2.8). The tropospheric circulation in 2002 also showed outstanding differences from LD years as shown in Fig. 2.7. The polar-front jet is weak and the subtropical jet shifts poleward in September and October. The upward EP flux in the high-latitude troposphere is weak in association with the weak polar-front jet.

The upward EP flux in the lower stratosphere is a good indicator of the interannual variations of the seasonal march of the stratospheric circulation through winter and spring (Fig. 2.9). The stronger wave activity in the lower stratosphere is associated with the earlier shift-down of the polar-night jet. Some scatter diagrams show the extreme situation of the year 2002 (Fig. 2.10): The upward EP flux is large in the lower stratosphere, the zonal mean zonal wind is weak in the mid-latitude stratosphere and strong in the upper troposphere, and the equatorward EP flux is small in the upper troposphere. However, the large deviations in 2002 are consistent with the fluctuations in the other 23 years except for the extremeness. Two other years (1988 and 2000) in ED years are also found in the similar situation as the year 2002 but have smaller deviations.

As stated in the last paragraph in Discussion, observational studies like the present one always suffer the limitation of the data length. The dataset for 24 years is not long enough to obtain a stable frequency distribution, but there is no other data of the real atmosphere. It will be important for us to use numerical models to supplement the statistical arguments based on much longer datasets.

Chapter 3

Interannual variations of the stationary wave of the zonal wavenumber 1

Abstract

A statistical analysis is made of the interannual variability of stratospheric planetary waves in the Southern Hemisphere in late winter using NCEP/NCAR reanalysis data gathered over a 20 year period from 1979 to 1998. The study investigates the dynamical coupling between the planetary waves and the tropospheric circulation, by focusing on the activity of transient baroclinic disturbances.

With the aid of EOF analysis applied to the 10 hPa monthly mean height anomalies and tropospheric circulation patterns, it is found that the year-to-year variation of quasi-steady planetary waves in late winter (September and October) is characterized by a longitudinal phase shift of zonal wavenumber 1 as well as by a variation in wave amplitudes. An eastward (westward) shift of the stratospheric planetary waves corresponds to a double-jet (single-jet) structure of the upper tropospheric (300 hPa) zonal winds. On the other hand, planetary wave amplitude variation is closely related to that of the meridional heat flux in the upper troposphere.

These results are reinforced by the Eliassen-Palm flux diagnosis composed of the stratospheric EOF scores, and hence the effect of tropospheric transient waves on the forcing to the stratospheric planetary waves is stressed.

3.1 Introduction

Mainly as a result of the abundance of satellite data gathered during the last two decades, stratospheric observations for both hemispheres have now become available and notable differences in dynamical features between the two hemispheres have become apparent, not only in their seasonal variations but also in their year-to-year variability.

For stratospheric circulation in the Southern Hemisphere (SH), Shiotani et al. (1993) made the first analysis on the interannual variation of the seasonal evolution of mean zonal winds and planetary waves, by using a TIROS-N SSU dataset covering the 10 year period from 1980 to 1989. They found that planetary waves in the SH stratosphere in late

winter show a significant year-to-year variation in association with changes in the intensity and latitudinal profiles of the polar-night westerlies. They further showed, through the Eliassen-Palm (EP) flux diagnosis, that evidence exists for a dynamical coupling between the stratosphere and troposphere which is related to the mean zonal wind variation.

Following this early work, Aoki et al. (1996) and Aoki and Hirota (1998) made further statistical analyses on the relationships between the SH tropospheric circulation and stratospheric planetary waves in order to identify the characteristic features which are unique to the SH.

Regarding the quasi-steady planetary waves in the stratosphere as seen in the monthly mean geopotential height field in wintertime, it has been widely recognized that the stratospheric wave is generated through an upward propagation of energy from the troposphere (e.g., Charney and Drazin, 1961). In the NH, the forcing in the lower atmosphere is considered to be due mainly to the large-scale topographic effect: This can be easily understood from the fact that the geographic location of stationary planetary waves in the NH winter stratosphere is almost always fixed by the topography, as in the cases of the Aleutian High and the Greenland Low, for instance.

In the SH stratosphere, however, the interannual variation of planetary waves is rather larger than that in the NH, in both location (phase) and wave amplitude (Shiotani et al., 1993). Quintanar and Mechoso (1995a) suggested that forcing from the Indian Ocean region is an important source of SH planetary waves, in addition to orographic and thermal forcing from the Antarctic continent. Note that this variability can be also seen in the year-to-year change of intensity and in the location of the so-called " Ozone Croissant" over the Antarctic continent in late winter (e.g. Kayano, 1997).

In view of the fact that the surface topographies are quite different between the two hemispheres, it is important to examine both the generation mechanism and interannual variability for planetary waves in the SH stratosphere in terms of the dynamical coupling between the troposphere and the stratosphere. In particular, investigation of the contribution of transient, baroclinic disturbances (i.e., the location and intensity of "storm tracks") to the tropospheric forcing in the SH is of considerable interest.

Another important issue concerning the SH stratospheric circulation is the difference of the seasonal march from that observed in the NH. As was shown, for example, by Hirota et al. (1983), planetary wave amplitudes in the SH stratosphere have two maxima in early winter (May and June) and in late winter (September and October), with a minimum in mid-winter (July-August). A number of aspects of this behavior are still open to question, however, so that in what follows I confine my attention to the period of maximum wave activity in late winter.

Keeping the above-mentioned differences between the two hemispheres in mind, in the present study I first make a statistical EOF analysis of the interannual variation of SH stratospheric circulation patterns over a 20 year period. I then discuss the relationship

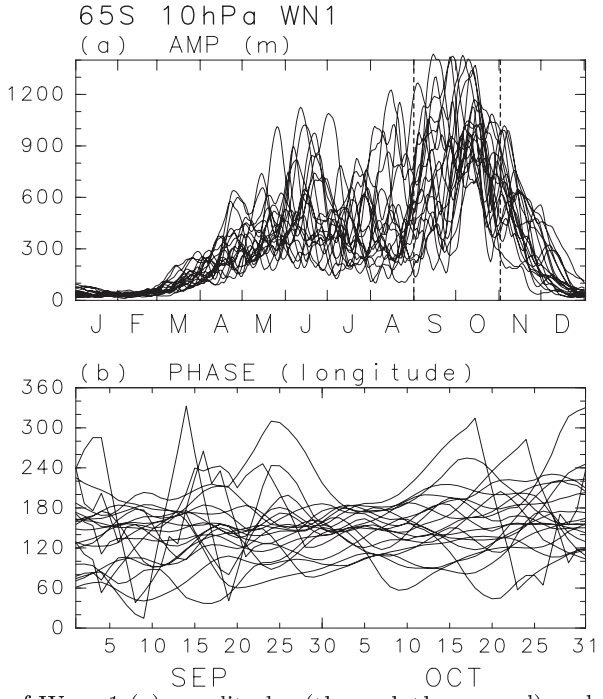

Figure 3.1: Time evolution of Wave 1 (a) amplitudes (through the annual) and (b) phases (from September to October) at 10 hPa, 65°S within the period 1979-1998.

with the tropospheric circulation, and especially with the activity of short-period and synoptic-scale transient disturbances. Suggestions are given for the role of transient waves in the forcing of steady-state planetary waves.

3.2 Data

In this study I use the daily NCEP/NCAR reanalysis data for the 20-year period from 1979-1998. The data was transformed as the previous chapter. Figure 3.1(a) shows the annual march of planetary waves of zonal wavenumber 1 (hereafter Wave 1) amplitudes at 10hPa, 65°S for the 20-year period. The wave amplitudes show maxima in September and October and large interannual variability in terms of their growth timing, as mentioned by Shiotani et al. (1993). Thus, monthly mean fields covering 40 months (September and October for 20 years) are used in making a statistical analysis to understand the structure and behavior of quasi-steady planetary waves in late winter. Figure 3.1(b) shows the time series of Wave-1 phase for the two months. The stationary component is dominant and no seasonal variation of phase is found during the period of the late winter (September and October). Thus it is valid to investigate the interannual variability of stationary waves with the 40 monthly mean datasets by ignoring the intraseasonal variations.

Throughout this chapter angle brackets ($\langle A \rangle$) denote monthly means and primes (A') represent deviations from the zonal mean.

3.3 Monthly mean features

Figure 3.2 shows the SH monthly mean geopotential height anomaly (deviations from the zonal mean) at 10 hPa for September months in the period 1979-1998. It can be easily seen that the zonal wavenumber 1 component is the most prominent with phase and amplitude quite variable over the 20 year period. Similar features are seen for October (not shown here). The variability is represented in Fig. 3.3, in which both scatter diagrams and histograms of the phase and amplitude of the monthly mean Wave 1 at 10 hPa are provided for (a) 65°S and (b) 65°N for the two winter months when planetary waves are active (September and October for SH, and January and February for NH). In the SH, the phase varies widely between 40° and 220° and is centered on about 150°, in contrast to the NH where the phase is almost locked around 180°. The amplitude is highly variable in both hemispheres. Before making a statistical analysis let us give a general view of the connection between the tropospheric and stratospheric circulation of the two specific years. Figure 3.4 illustrates longitude-height cross sections of monthly mean geopotential height anomaly ($\langle Z' \rangle$) between 55°S and 65°S for September of 1989 and 1990. In Fig. 3.3, the data of these two years are plotted with open circles, showing that both phase and amplitude are quite different between the two years. As shown in Fig. 3.2, the quasi-stationary planetary wave in the stratosphere shifts eastward and has larger amplitude in 1990 than in 1989. In the troposphere, the amplitude of the Wave 1 in 1990 is large, reflecting the structure in the stratosphere, while in 1989 it is rather small.

The cases for the years 1989 and 1990 indicate different tropospheric circulation patterns in association with the stratospheric pattern. In the following sections I first examine the interannual variability of planetary waves in the SH stratosphere in a statistical manner. Then, I investigate how the connections between the troposphere and stratosphere differ in relation to this variability.

3.4 EOF of the stratospheric circulation

The empirical orthogonal function (EOF) analysis is applied on the basis of the unstandardized covariance matrix of monthly mean geopotential height anomaly at the 10 hPa level between 20°S and 90°S for the 40 months of the analysis period. Taking into account the difference in area on a sphere, monthly mean variability is weighted by the square root of the cosine of latitude.

Figure 3.5(a) gives the 40-month mean pattern (i.e., climatology) of the 10 hPa height deviation, in which the dominance of Wave 1 is observed with the ridge and trough located at 150°E and 50°W respectively along the latitude belt of about 60-70°S.

With the long-term variations of this pattern, the first mode of the analysis (EOF1) shown in Fig. 3.5(b) indicates the east-west fluctuation of phase, since the dipole pattern is almost orthogonal to the climatological pattern. In the case that the standardized lead-

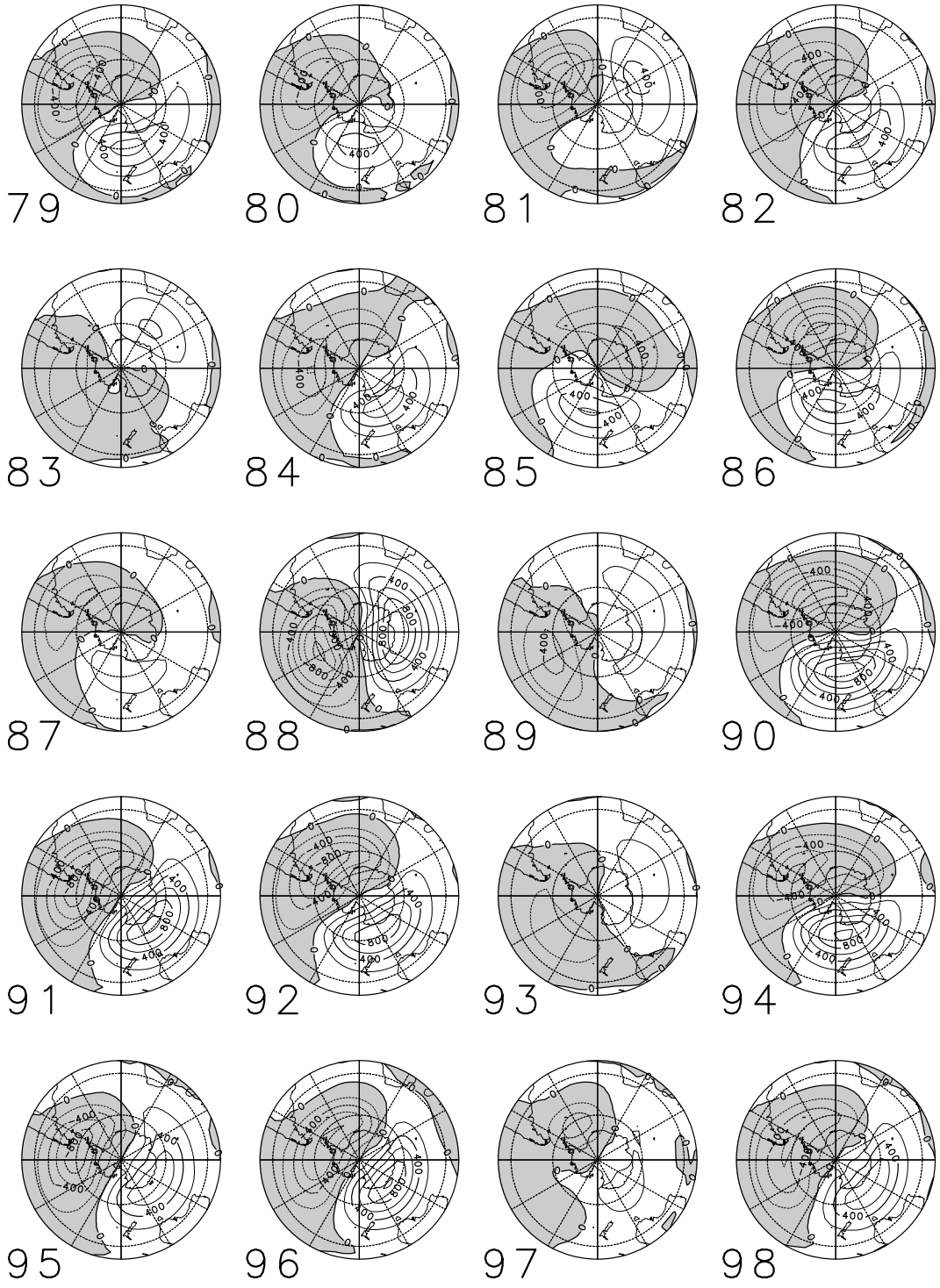

Figure 3.2: Monthly mean height anomaly of $\langle Z' \rangle$ (unit in meter) at 10 hPa for September months between 1979-1998. The outer circle corresponds to the 20°S parallel. The contour interval is 200 m and negative values are shaded.

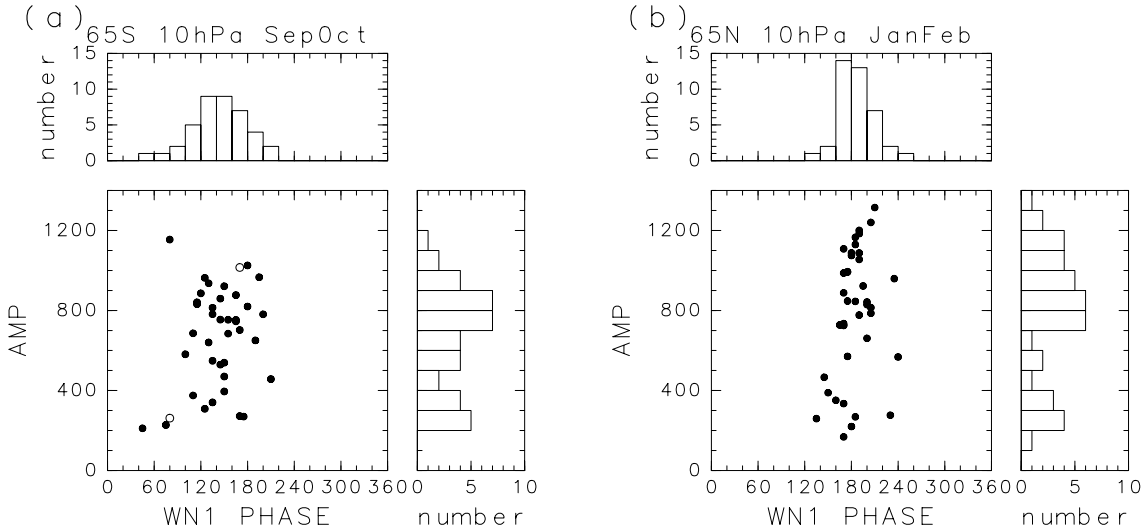

Figure 3.3: Scatter diagrams for monthly mean Wave 1 at 10 hPa, (a) 65°S and (b) 65°N on the phase and amplitude plane. The data consist of (a) September and October, (b) January and February, of 1979-1998. The upper and right panels are histograms of phase and amplitude respectively. Open circles in (a) indicate the September of 1989 (lower point) and 1990 (upper point) used in Fig. 3.4

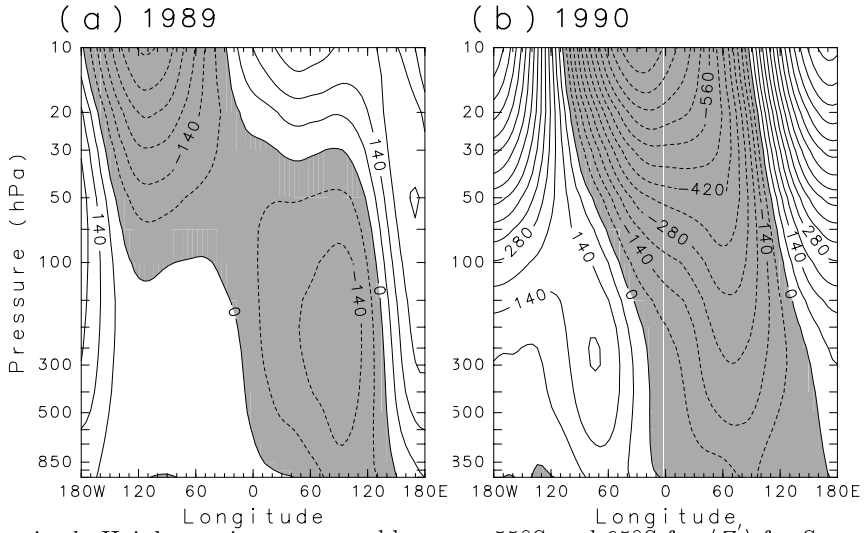

Figure 3.4: Longitude-Height sections averaged between 55°S and 65°S for $\langle Z' \rangle$ for September in (a) 1989, and (b) 1990. The contour interval is 70 m. Shaded areas correspond to negative values.

ing principal component of EOF1 (PC1) is positive (negative), the phase shifts westward (eastward) from the climatological pattern.

On the other hand, the pattern of EOF2 (Fig. 3.5c) is almost in phase with Fig. 3.5(a), which indicates the variation of wave amplitude. Positive (negative) values of PC2 denote the large (small) wave amplitude. Both PC's explain large fractions of the total variance (59% for PC1 and 29% for PC2), showing that the interannual variability of planetary waves in the SH stratosphere is characterized by longitudinal phase shifts and amplitude fluctuations.

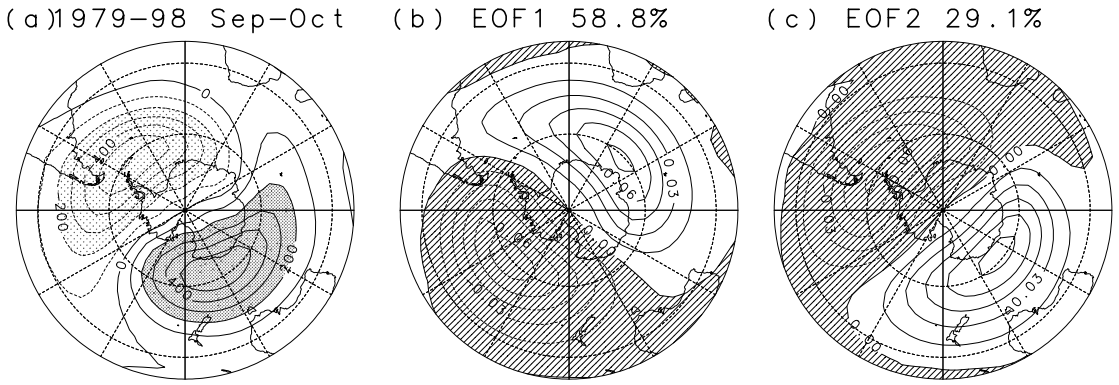

Figure 3.5: EOF patterns of (b) the first and (c) the second principal components obtained from the monthly mean geopotential height anomaly $\langle Z' \rangle$ at 10 hPa taken from September and October over the 20-year analysis interval and (a) average of the 40 months. The outer circle is the 20°S parallel. The contour interval is 0.15 and negative values are shaded for (b) and (c). For (a) the contour interval is 100 m.

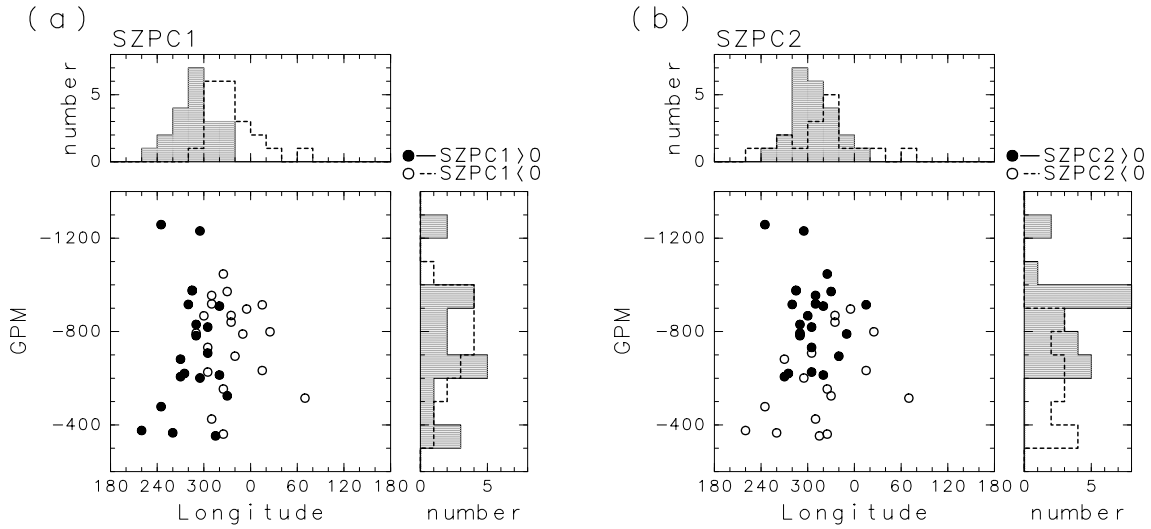

Figure 3.6: Scatter diagrams of the longitude and the values of the minimum $\langle Z' \rangle$ anomaly at 10 hPa between 50°S and 75°S. (a) Solid (open) circle indicates PC1 index positive (negative) and (b) solid (open) circle indicates PC2 index positive (negative). Histograms of the minimum value and its position are shown in the right and upper panels respectively.

The representation shown in Fig. 3.6 gives scatter diagrams and histograms of the longitude and value of minimum $\langle Z' \rangle$ at 10 hPa, i.e., the location and the depth of the trough according to the sign of the PC's. The classification by PC1 sign (Fig. 3.6a) confirms the separation of the east-west drift of phase with the positive groups shifting westward, while the wave intensity is clearly separated by the sign of PC2 (Fig. 3.6b). The amplitude for the positive PC2 category is certainly larger.

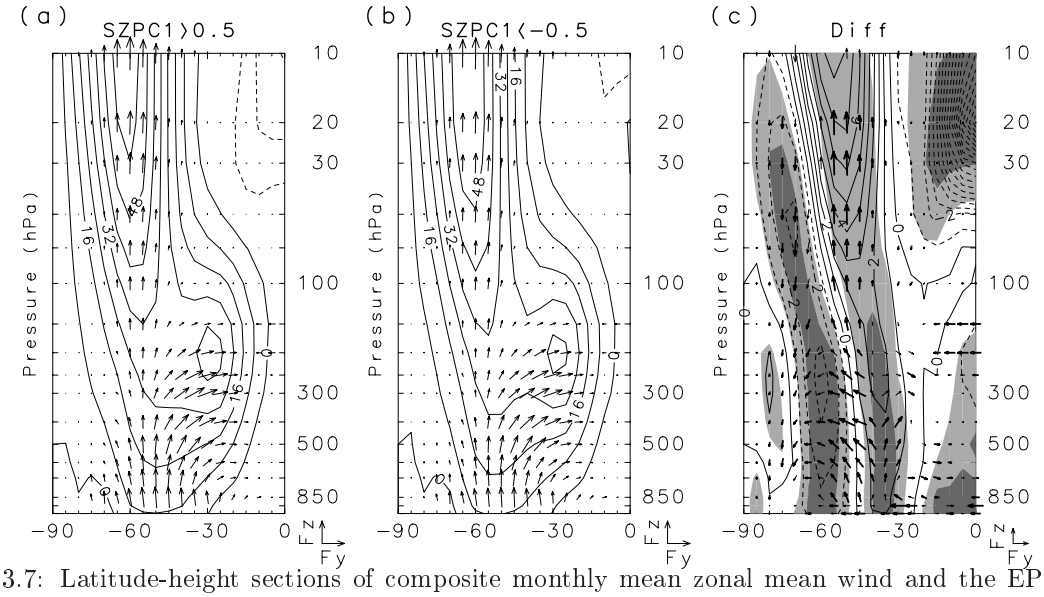

Figure 3.7: Latitude-height sections of composite monthly mean zonal mean wind and the EP flux for the group with (a) positive (b) negative PC1 index, and (c) the difference between the two. The contour interval is 8.0 m s^{-1} for (a) and (b). The contour interval of (c) is 1 m s^{-1}. Light (dark) shaded areas are significant in 1σ (2σ). The vertical component of the EP flux is weighted by the inverse of density. The length of the unit vectors corresponds to 1.0 $\times 10^6$ kg s^{-2} for the horizontal component and 1.0 $\times 10^6$ m^3 s^{-2} for the vertical component for (a) and (b). The length of the unit vector for (c) is one-tenth of that for (a) and (b). Vectors are drawn only when the significance level is above 95% (corresponding to 2σ) with bold arrows and above 68% (1σ) with thin arrows.

3.4.1 Difference of the zonal mean zonal wind and wave activity

In order to investigate the variability of stratospheric waves in terms of dynamical coupling to the troposphere, I made a composite analysis of monthly mean zonally averaged zonal winds and the Eliassen-Palm (EP) flux vectors with both PC1 and PC2 as indices. For this purpose, the sub-dataset in which the PC score is larger (smaller) than 0.5 (-0.5) is used as the positive (negative) PC category. In practice, the numbers of samples N used in the composite analysis are $N^+ = 13$ and $N^- = 11$ for positive and negative PC1, and $N^+ = 14$ and $N^- = 12$ for positive and negative PC2, respectively.

As regards the statistical significance of this composite analysis, I make a test in a following way: From the all dataset (40 month samples), I extract 2 sets (N^+ and N^-) randomly, and make the composite difference between the two sets. By repeating this calculation for 10,000 times with randomly chosen 2 sets, I investigate the statistical distribution of the composite differences for zonal winds and EP fluxes. As is expected, the result of this test reveals that the composite differences of 10,000 cases show the normal distribution with the median close to zero. Compared with this random test, as shown below in Figs. 3.7- 3.15, the characteristic differences of the composite analysis with PC1 and PC2 indices are substantially larger than the standard deviation σ or more. Therefore the results shown below are statistically significant.

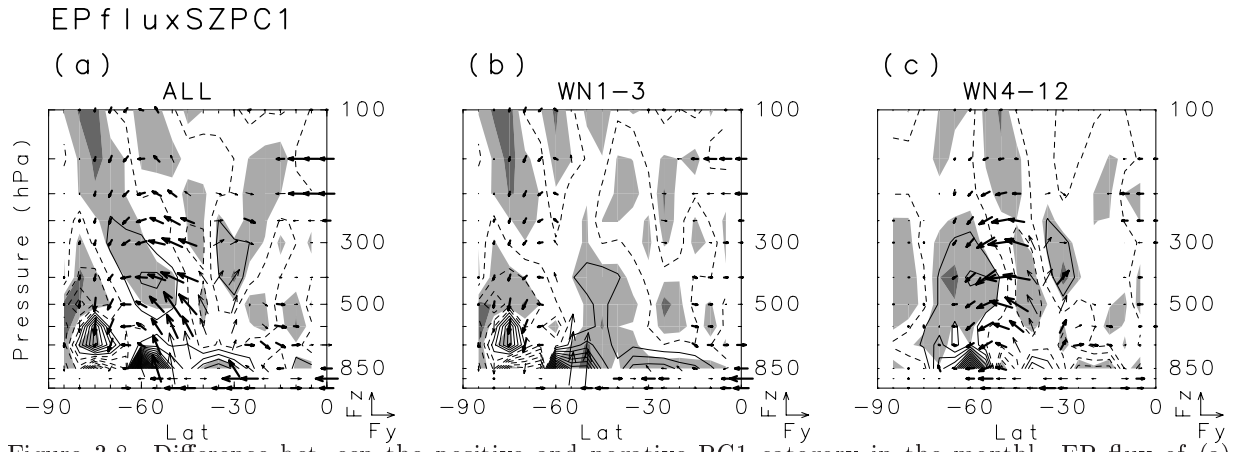

Figure 3.8: Difference between the positive and negative PC1 category in the monthly EP flux of (a) total waves, (b) zonal wavenumber 1-3, (c) zonal wavenumber 4-12 and its divergence. The contour interval for the divergence is 0.09 m s^{-1} day $^{-1}$. Solid contours indicate the convergent region and dashed lines divergent region. Light (dark) shaded areas are significant in 1σ (2σ). The length of the unit vectors corresponds to 1.0 $\times 10^6$ kg s^{-2} for the horizontal component and 5.0 $\times 10^2$ kg s^{-2} for the vertical component. Vectors are drawn only when the significance level is above 95% (corresponding to 2σ) with bold arrows and above 68% (1σ) with thin arrows.

Composite maps of monthly mean zonal winds and EP flux vectors for positive and negative PC1's are shown in Figs. 3.7(a) and (b), respectively. Vertical components of the EP flux, F_z, are weighted by the inverse of the density in order to emphasize the features in the stratosphere clearly. In both of these categories common features for the late winter circulation are found: The polar-night jet structure is strong in the stratosphere and the subtropical jet structure is found in the troposphere. The EP vectors point upward and equatorward and the wave activity shows notable propagation into the high-latitude stratosphere where the westerly winds are strong.

The difference between the two categories is shown in Fig. 3.7(c). Light and dark shadow correspond to the area whose significance level is larger than 68% (i.e. the value is larger than one σ of the random distribution) and 95% (larger than 2σ), respectively. The difference of EP vectors are drawn whose magnitude ($|\mathbf{F}|$) are statistically significant in 2σ (1σ) with bold (thin) arrows. The maximum of the stratospheric westerly jet is located equatorward (poleward) for the positive (negative) PC1 category. The tropospheric westerly winds also show a different structure: The positive PC1 category corresponds to a strong lower latitude jet, described here as a, "single-jet structure", whereas the negative PC1 category corresponds to enhanced higher latitude jet, the, "double-jet structure". These features will be shown more clearly later in Fig. 3.11. This correspondence of the jet structure between the troposphere and the stratosphere is in agreement with the result of Aoki et al. (1996). The composite difference of the vertical component of the EP vector in the stratosphere displays a dipole structure in harmony with the structure of the anomaly

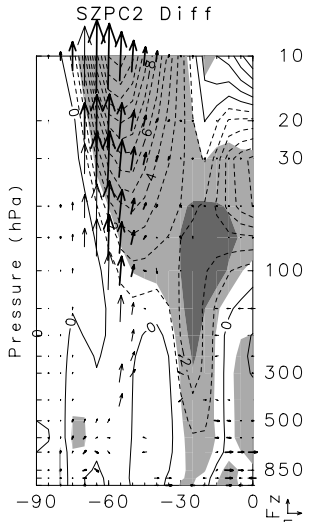

Figure 3.9: Same as Fig. 3.7 (c) but for the difference between the positive and negative PC2 index.

in the stratospheric zonal wind, as is expected from wave propagation theory.

The composite EP vectors in the troposphere show different features those in the stratosphere. In order to see the tropospheric processes more precisely, I show the composite difference of the tropospheric total EP flux again and its divergence between the PC1 categories in Fig. 3.8(a) and their breakdown into those of Waves 1-3 and Waves 4-12 in Fig. 3.8(b) and (c), respectively. Again, bold (thin) arrows indicate that difference in the magnitude of the EP vectors is statistically significant at the 95% (68%) level of significance and dark (light) shadow indicates that the difference of EP flux divergence is significant at the 95% (68%) in the area. As the components of the EP flux are not weighted by the inverse of the density in this figure, I can make a direct, visible comparison between wave activity at the different levels. Horizontal vectors in Figs. 3.8(a) and (c) turn weakly equatorward between 25°S and 35°S, and poleward between 45°S and 60°S. These features indicate that the positive PC1 category tends to have a small poleward momentum flux at higher latitudes and a large poleward flux at lower latitudes compared with the negative PC1 category. Upward-pointing arrows around 40°S mean larger (smaller) poleward heat fluxes for the positive (negative) category. The contribution from Waves 4-12 (Fig. 3.8c) shows similar features so that in Fig. 3.8(a), indicating that the difference is largely due to the synoptic-scale waves. The composite difference of the EP flux divergence contributed from the synoptic scale waves (the contour map of Fig. 3.8c), exhibits a tripole structure in the upper troposphere. The positive region around 40°S is explained by the fact that the EP flux attributed to the synoptic scale waves is weakly (strongly) convergent in this region for the positive (negative) PC1 category, because at this level the EP flux divergence ($\nabla \cdot \mathbf{F}$) is normally negative. In the same way, the negative region around 60°S is explained by the strongly (weakly) convergence of the positive (negative) PC1 category. Compared with the difference of zonal winds (Fig. 3.7c), the difference of $\nabla \cdot \mathbf{F}$ seems to work to

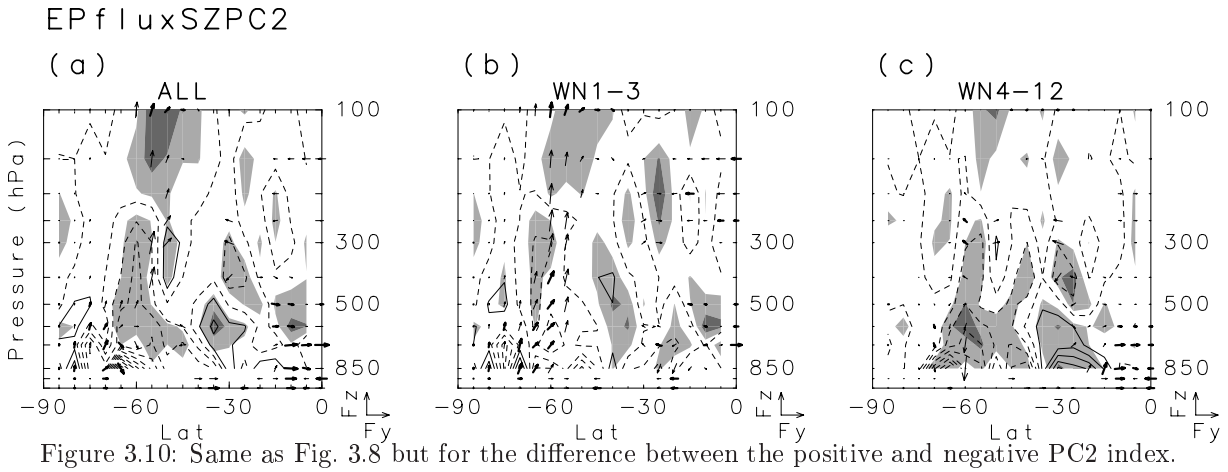

Figure 3.10: Same as Fig. 3.8 but for the difference between the positive and negative PC2 index.

maintain the zonal wind anomaly from the climatological pattern. This is consistent with the results of earlier studies (e.g., Hartmann and Lo, 1998).

In Fig. 3.9 I next categorize the dataset into the sign of PC2 in a similar way to Fig. 3.7(c). The positive PC2 category (large amplitude year) tends to have a strong polar-night jet wind. It is interesting that zonal mean zonal wind in the troposphere does not show notable difference in the extratropical latitude but does so in the tropical region (around 20°S). The wave activity in the stratosphere varies so as to produce a wave-mean flow interaction. The stronger (weaker) wave activity for the positive (negative) PC2 category is consistent with the features seen in Fig. 3.6(b). This is also the case for the upper tropospheric wave activity in the high latitude discussed below.

Figure 3.10 shows the same representation as Fig. 3.8 but for PC2 index. A difference is found in the upper tropospheric vertical component between 55°S and 65°S in Fig. 3.10(a). This pattern is also seen in Fig. 3.10(b), indicating the difference is largely due to the activities of the planetary-scale waves. It is also notable that the difference is prominent in the upper troposphere above 500 hPa as to planetary-scale waves. The difference in the divergence corresponds to this vertical EP flux anomaly, i.e. positive anomaly around 300 hPa between 55°S and 65°S. As the EP flux is weakly convergent or divergent in this region for both categories (not shown), the difference in the upper tropospheric divergence pattern suggests the generation of planetary waves at this level. The composite difference of EP flux divergence due to the synoptic-scale waves (Fig. 3.10c) shows the dipole pattern in the lower troposphere.

3.4.2 Difference of the tropospheric circulation pattern

I inspect the hemispheric pattern of the zonal wind and the eddy flux in the troposphere for the purpose of gaining a more precise understanding of the different flux patterns between the PC's categories seen in the previous section. Figure 3.11 shows PC1 composite maps of

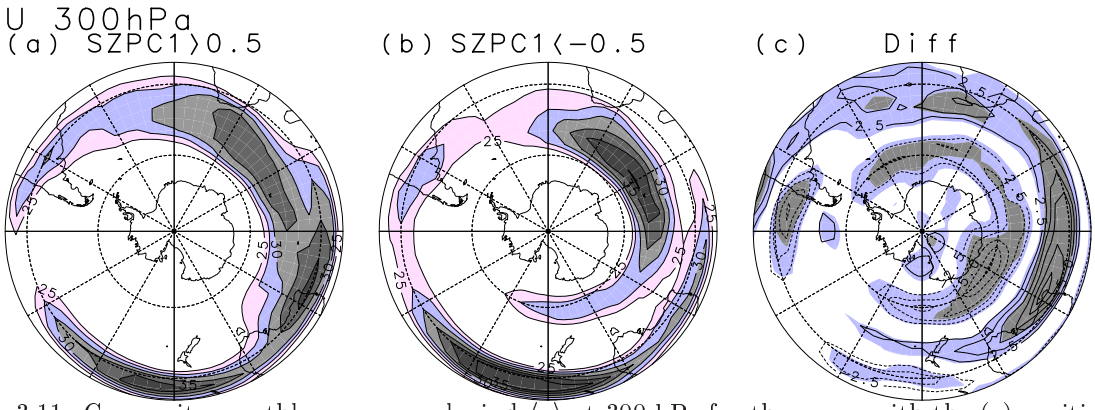

Figure 3.11: Composite monthly mean zonal wind $\langle u \rangle$ at 300 hPa for the group with the (a) positive (b) negative PC1 index, and (c) the difference between the two. The contour is drawn above 20 m s^{-1} with an interval of 2.5 m s^{-1}, and values greater than 25 m s^{-1} are painted for (a) and (b). The contour interval of (c) is 1.25 m s^{-1} and light (dark) shaded areas are significant in 1σ (2σ).

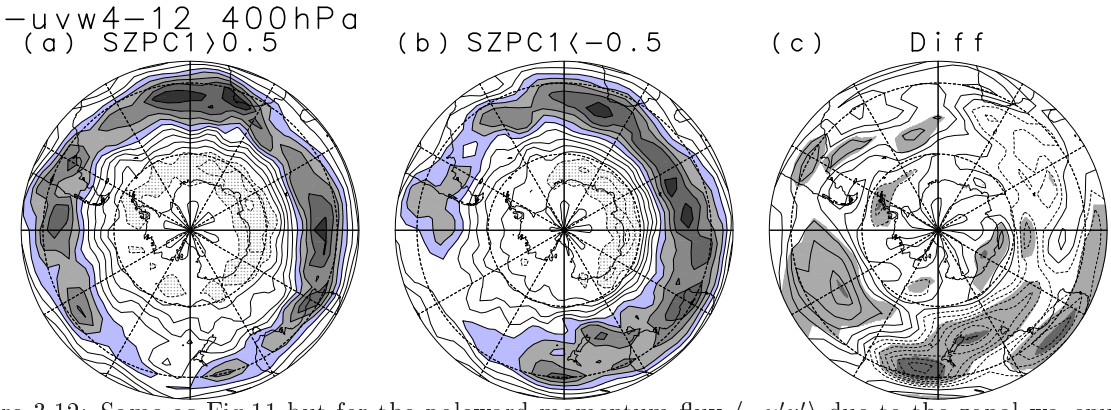

Figure 3.12: Same as Fig.11 but for the poleward momentum flux $\langle -u'v' \rangle$ due to the zonal wavenumber 4-12 at 400 hPa. The contour interval of (a) and (b) is 6.0 m^2 s^{-2}, and values greater than 24 m^2 s^{-2} are painted for (a) and (b). The positive (negative) values refer to the mean poleward (equatorward) momentum fluxes. The contour interval of (c) is 3.0 m^2 s^{-2} light (dark) shaded areas are significant in 1σ (2σ).

the monthly mean zonal wind $\langle u \rangle$ at 300 hPa. As was shown in Fig. 3.7, the positive PC1 group, which means a westward drift of stratospheric waves, corresponds to the single-jet structure profile, while the negative PC1 group corresponds to a double-jet structure in the upper troposphere. Between the two groups there is a large difference in the Eastern Hemisphere (Fig. 3.11c).

Taking into the consideration the notable difference in the horizontal component of the EP flux (Fig. 3.8c), the hemispheric pattern of eddy poleward momentum flux ($\langle -u'v' \rangle$) due to the synoptic scale waves (wavenumber 4-12) at 400 hPa is displayed in Fig. 3.12. The wave activity is strong between 40°S and 50°S over the Atlantic and Indian Oceans. I have also plotted the eddy momentum flux of the 10-day high-pass filtered component (not shown) and found a similar pattern, with the exception of smaller fluxes over the

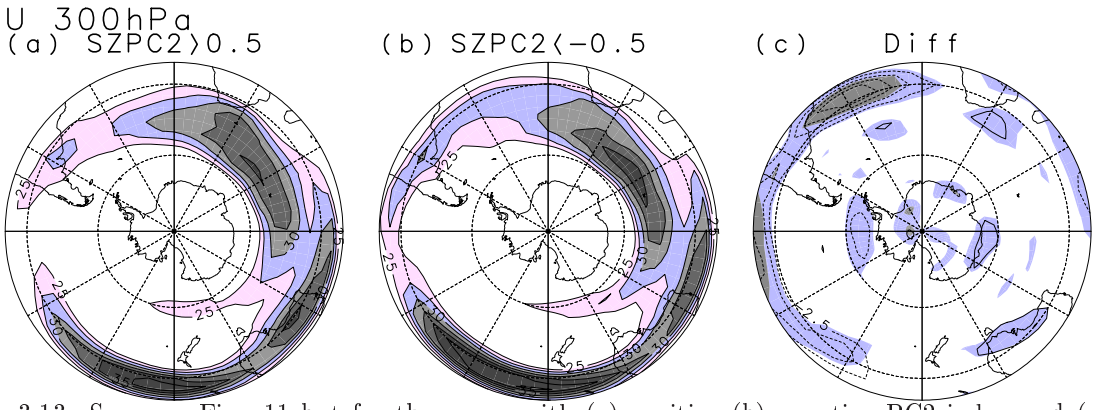

Figure 3.13: Same as Fig. 11 but for the group with (a) positive (b) negative PC2 index and (c) the difference between the two.

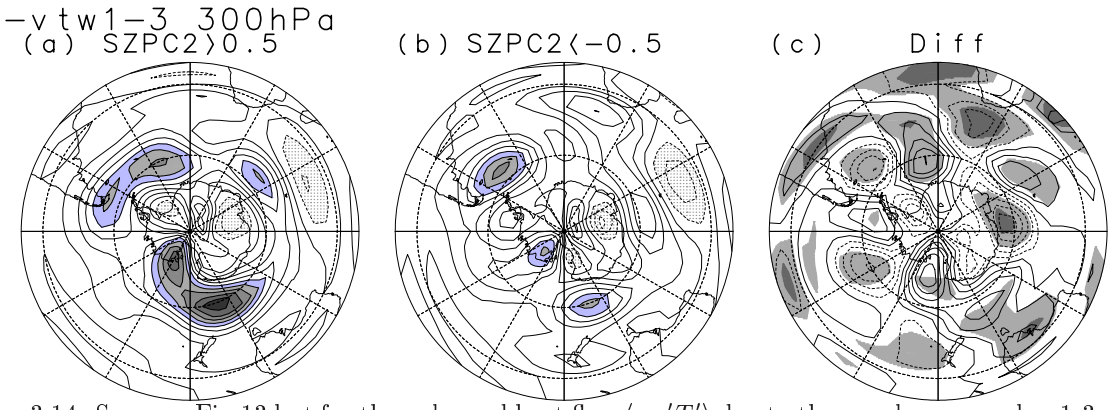

Figure 3.14: Same as Fig.13 but for the poleward heat flux $\langle -v'T' \rangle$ due to the zonal wavenumber 1-3 at 300 hPa. The contour interval of (a) and (b) is 1.5 K m s^{-1} and values greater than 6.0 K m s^{-1} are painted. The positive (negative) values refer to the mean poleward (equatorward) heat fluxes. The contour interval of (c) is 1.0 K m s^{-1}. Light (dark) shaded areas are significant in 1σ (2σ).

Atlantic. These features therefore roughly represent the storm tracks in the SH (Trenberth 1991). For the PC1 negative category, there is another large poleward flux region to the south of Australia, and this difference results in the difference in the horizontal component of the EP flux (Fig. 3.8c). Compared with the zonal mean wind map (Fig. 3.11b), this region corresponds to the northward side of the exit of the polar-front jet for the PC1 negative category. The eddy momentum flux therefore acts to maintain the jet structure downstream of jet core, which is consistent with the earlier work about the jet stream and the storm tracks (e.g. Holton, 1992).

The PC2 composite maps of zonal winds (Fig. 3.13) at 300 hPa do not show marked differences between the positive and negative category except for the subtropical jet in the Western Hemisphere. This agrees with the features seen in Fig. 3.9.

The poleward eddy heat flux patterns ($\langle -v'T' \rangle$) contributed from the planetary scale waves at 300 hPa (Fig. 3.14) reveal a remarkable contrast not only in strength but also in distribution. A strong poleward heat flux appears at high latitude and along the 55°S zone:

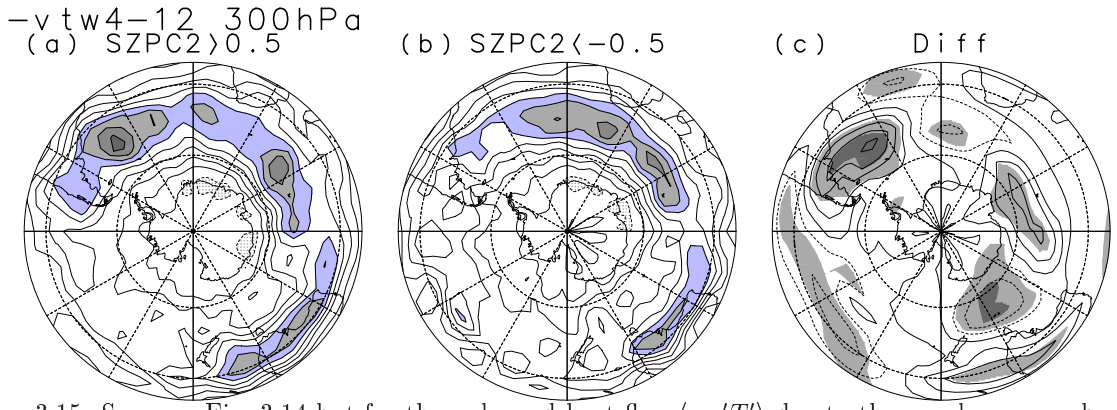

Figure 3.15: Same as Fig. 3.14 but for the poleward heat flux $\langle -v'T' \rangle$ due to the zonal wavenumber 4-12 at 300 hPa. The contour interval of (a) and (b) is 1.5 K m s^{-1} and values greater than 6.0 K m s^{-1} are painted. The contour interval of (c) is 0.75 K m s^{-1}. Light (dark) shaded areas are significant in 1σ (2σ).

There are two maxima, one between 160°E and 180° and the other around the Atlantic. In the former region, there is a big difference in strength for the PC2 fluxes. For the latter region, the maximum of the positive PC2 fluxes lies in a broader region. The two maxima mean that the stationary wavenumber1 component is dominant in the stratosphere.

Figure 3.15 shows the PC2 composite maps of eddy heat flux due to the synoptic scale waves (wavenumber 4-12) at 300 hPa. Taking a zonal mean, the difference in the magnitude is quite small as shown in Fig. 3.10(c). For the horizontal pattern, however, a large difference in the distribution is observed. The positive PC2 category shows a maximum in poleward eddy heat flux around the Atlantic, while the negative category maximizes around the Indian Ocean.

In Fig. 3.10(b) it was demonstrated that for planetary-scale waves, the positive PC2 category has the larger vertical component of EP flux than the negative category, especially above 400 hPa. As the upper tropospheric zonal winds in mid-latitude do not appear to have a marked difference (Fig. 3.9), it is interesting to consider the cause of this difference in wave activity. One possible explanation is that the nonlinear effect cannot be negligible in the troposphere: The difference shown in Fig. 3.15 may be significant for the production of planetary scale waves through the nonlinear effect. Further examination is needed to clarify the temporal and spatial characteristics of the waves involved in the nonlinear effect (wave-wave interaction) in relation to the generation of planetary waves.

3.5 EOF of the tropospheric circulation

I make an EOF analysis on the tropospheric circulation, in order to reconfirm the connection between the troposphere and stratosphere. Since a large difference in tropospheric zonal winds between the PC1 sign categories appears in the Eastern Hemisphere (Fig. 3.11), the monthly mean tropospheric zonal winds in eight SH tropospheric levels (850-200 hPa)

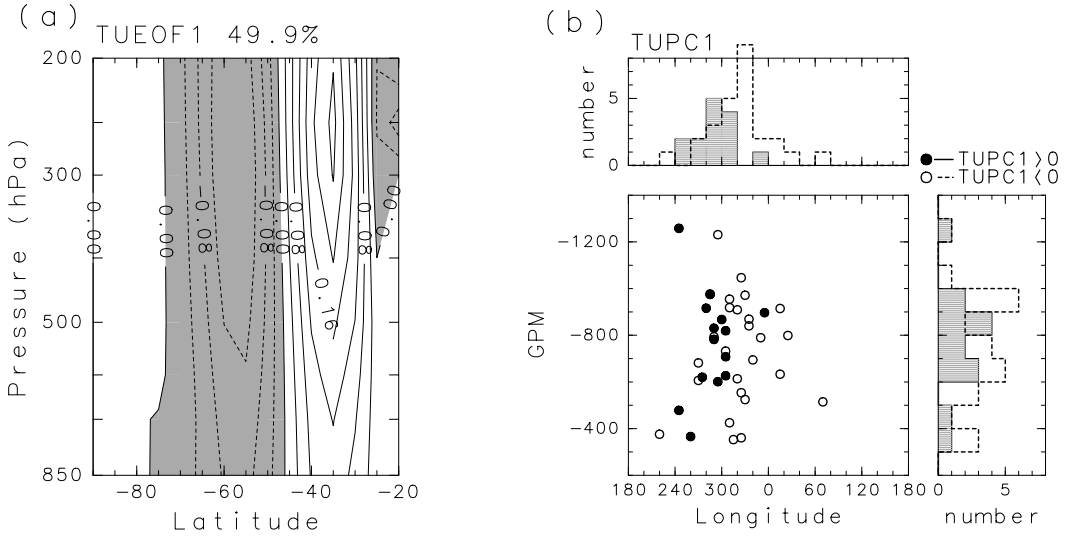

Figure 3.16: (a) Latitude height section (850-200 hPa) of the first EOF mode for monthly mean zonal wind averaged longitudinally for the Eastern Hemisphere. Negative values are shaded. (b) Same as Fig.6, but solid (open) circles denote positive (negative) TUPC1.

are averaged over 0°-180° longitude. Before making the EOF analysis, the climatology for each calendar month (20-year average) was removed from the each dataset to extract the seasonal variation. The data are weighted by the square-root of the density at each level to give anomalies equal weights in terms of kinetic energy.

The first mode shown in Fig. 3.16(a) exhibits a meridional dipole pattern with a node centered around 45°S, which explains up to about 50% of the total variance. When the PC of this mode (denoted as TUPC1 hereafter) is positive (negative), the tropospheric zonal wind has a single-jet (double-jet) structure. Classification by the sign of TUPC1 reconfirms that the phase of planetary waves at 10 hPa is clearly separated as shown in Fig. 3.16(b), consistent with the separation based on the stratospheric PC1 sign shown in Fig. 3.6(a).

The difference in the tropospheric zonal wind structure between the PC1 category seems to be similar to the mode of the low frequency variation, i.e., a zonally symmetric and equivalent barotropic dipole pattern centered at 40°S and 60°S (e.g.,Yoden et al., 1987, Shiotani 1990). I made an EOF analysis of the zonally averaged monthly mean zonal wind in the troposphere and found that the first component of this PC is certainly well correlated with TUPC1 (correlation coefficient is 0.78). However, I could not determine whether it categorizes the phase of the stratospheric wave. Therefore, these results suggest that the difference seen in the zonal wind structure between the PC1 category (Fig. 3.11) is not the same as the tropospheric zonally symmetric variation presented by earlier authors.

3.6 Conclusions

An EOF-based statistical study of the interannual variations of planetary waves in the wintertime has been made. SH stratosphere using NCEP/NCAR reanalysis dataset covering a 20 year period. The results were used to interpret some aspects of upper tropospheric circulation such as the mean zonal flow and various scale waves. Resulting from this work, the characteristic features of the interannual variations of the stratospheric planetary waves and their connection with the tropospheric dynamics can be summarized as follows :

- The year-to-year variation of monthly mean planetary waves at 10hPa in late winter can be characterized by an east-west drift of phase, and by a well defined wave amplitude variation (Figs.3.5 and 3.6).

- The variation of the phase is related to the structure in the tropospheric jet. The westward (eastward) drift of the stratospheric wave corresponds to a single-jet (double-jet) structure in the upper troposphere over the Eastern Hemisphere (Figs. 3.7 and 3.11). The activities of synoptic-scale waves show a variety of different features which to maintain the jet structure (Figs. 3.8 and 3.12).

- The vertical component of the EP flux in the troposphere is larger when stratospheric planetary waves have the large amplitudes and this inclination is most pronounced around the 300 hPa level (Figs.3.9 and 3.10). In relation to the hemispheric pattern of monthly mean activities of the planetary scale waves in the troposphere, we found a difference in the maximum location and the intensity of the heat flux according to the difference in the amplitude variability (Fig. 3.14). The hemispheric pattern of the eddy heat flux due to the synoptic waves also shows a different distribution(Fig. 3.15).

Building on the basis of the present statistical study, future work will aim to clarify the dynamical process to explain the connection between the troposphere and the stratosphere. Scinocca and Haynes (1998) introduced the Transformed Fourier Decomposition (TFD) equations to define the nonlinear forcing. The TFD equations express the forcing of a specific wavenumber by wave-wave interactions and employ a relation between the Fourier decomposed quasi-geostrophic potential vorticity equation and the total eddy-vorticity forcing. In this sense, the TFD equations would be a powerful tool to investigate the effect of synoptic waves on the generation of planetary scale waves propagating into the stratosphere.

Since the distributions of the storm tracks and the zonal wind structure are tightly correlated in the SH (e.g., Karoly, 1990), we also need further studies to define the relationship between the zonal wind and horizontal eddy fluxes due to the synoptic waves, in terms of the interannual variability.

Chapter 4

Quasi-periodic variations of the polar vortex due to the wave-wave interaction

Abstract

The winter polar vortex in the Southern Hemisphere stratosphere is characterized by prominent quasi-stationary planetary wave of zonal wavenumber 1 (Wave 1) and eastward traveling Wave 2. Quasi-periodic variations of the polar vortex are investigated in terms of the wave-wave interaction between Wave 1 and Wave 2 with both the NCEP/NCAR Reanalysis dataset from 1979 to 2002 and a spherical barotropic model.

A typical case shows that the transient Wave 1 generated by the wave-wave interaction has comparable amplitude to those of the stationary Wave 1 and the traveling Wave 2, and has a node around 60°S where these primary waves have large amplitude. The transient Wave 1 travels eastward with the same angular frequency as that of the traveling Wave 2. The polar night jet also vacillates with the same frequency such that it has its minimum when the stationary Wave 1 and the transient Wave 1 are in phase at the polar side of the node. The vacillation is basically due to quasi-periodic variations of the wave driving by the interference between the stationary and traveling Wave 1s.

Similar periodic variations of the polar vortex are obtained in our model experiment in the circumstance that stationary Wave 1 generated by surface topography has comparable amplitude to eastward traveling Wave 2 which is generated by the barotropic instability of a forced mean zonal wind.

The winter polar vortex shows large interannual variability. Similar quasi-periodic variations due to wave-wave interaction often occurred for the 24 years in late winter when the transient Wave 2 was vigorous.

4.1 Introduction

In the Southern Hemisphere (SH) stratosphere, quasi-stationary planetary wave of zonal wavenumber 1 (hereafter Wave 1) and eastward traveling Wave 2 with a period of about 15 days are prominent in late winter (e.g., Harwood 1975). It has been widely recognized that the quasi-stationary Wave 1 is generated in the troposphere due to zonal asymmetry

of the surface topography and land-sea distributions, and propagates into the stratosphere (Randel 1987). Interannual variation of the quasi-stationary Wave 1 was investigated by Hio and Hirota (2002). On the other hand, generation mechanism of the eastward traveling Wave 2 is *in situ* instabilities (Hartmann 1983; Manney et al. 1988). Manney et al. (1991a) found that the Wave 2 is confined to the stratosphere during the episodes of its regular eastward propagation, while the Wave 2 in the stratosphere is propagated from the upper troposphere during episodes of largest growth. A subsequent eigenvalue analysis (Manney et al. 1991b) also showed that barotropic/baroclinic instabilities play an important role for the generation of the stratospheric Wave 2 in late winter. Some other mechanisms for the generation of traveling Wave 2 have also been proposed, such as the baroclinic instability of the zonal mean field in the troposphere (Hartmann 1979) and the wave-wave coupling among baroclinic waves (Young and Houben 1989; Scinocca and Haynes 1998).

The importance of wave-wave interaction in the planetary-wave variations has been investigated for the Northern Hemisphere (NH) winter since the 1980s. The negative correlation between the amplitude of Waves 1 and 2 in the NH stratosphere (e.g., Hirota and Sato 1969) was investigated by calculating the potential enstrophy budget (Smith 1983; Smith et al. 1984; Robinson 1985). As for the SH, wave-wave interaction between stratospheric Waves 1 and 2 in late winter and spring has been reported by some authors; Mechoso et al. (1988) and Manney et al. (1991a) suggested that these amplitudes are sometimes anti-correlated in September and October.

Hirota et al. (1990) and Shiotani et al. (1990) studied quasi-periodic amplification of Wave 1 in the SH stratosphere in late winter and found that Wave-1 amplitude reaches its maximum when the ridges of Waves 1 and 2 overlap. Ushimaru and Tanaka (1992) simulated the interaction among Wave 1, Wave 2 and the zonal mean zonal flow using a semi-spectral stratosphere-only model in which both the stationary Wave 1 and the eastward traveling Wave 2 were prescribed at the bottom boundary near the tropopause. In their model result, the energy transfer between Wave 1 and Wave 2 is important for the periodic amplification of Wave 1.

Some model studies have shown that stratospheric variations, such as the vacillation of the mean zonal flow, can occur internally with fixed external conditions, including time independent wave forcing near the tropopause (e.g., Holton and Mass 1976; Yoden 1987; Scaife and James 2000). The vacillation phenomenon corresponds to periodic occurrence of the stratospheric sudden warming events. All of their results show the importance of the periodic change in the vertical structure of the polar vortex through the interactions between planetary waves and zonal mean zonal flow. Recently, Rong and Waugh (2003) (hereafter RW) examined internal variability of the polar vortex in a shallow water model, i.e. a one layer model, with time independent topographic forcing and relaxation to a constant zonally symmetric equilibrium state. They demonstrated that the horizontal structure of potential vorticity (PV) as well as the vertical structure plays an important

role in the vacillation of the stratospheric flow. For the large topographic amplitude, there are breakdown and recovery cycles of the polar vortex, and filamentary structures are produced during the vortex breakdown due to highly nonlinear process.

For the small amplitude forcing cases in RW experiments, on the other hand, there is only a periodic undulation of the edge of the polar vortex and the vacillation of the zonal flow does not occur. These features resemble the SH winter circulation. In contrast to RW, I focus on the periodic variations under such a condition that the flow obeys the weakly nonlinear dispersion theory. This condition allows a triad of wavenumbers for resonant energy exchange (Lighthill 1978). Under the circumstance of the SH winter stratosphere, the stationary Wave 1 ($A_1 \exp(\mathbf{k_1} \cdot \mathbf{x})$) and the eastward traveling Wave 2 ($A_2 \exp(\mathbf{k_2} \cdot \mathbf{x} - \omega_2 t)$) of the same latitudinal harmonics can generate traveling Waves 1 or 3 ($A_3 \exp(\mathbf{k_3} \cdot \mathbf{x} - \omega_3 t)$) which satisfy the following relationships,

$$\mathbf{k_1}(1, l) + \mathbf{k_2}(2, l) = \mathbf{k_3}(1 \text{ or } 3, 2l) \tag{4.1}$$

$$0 + \omega_2 = \omega_3. \tag{4.2}$$

Therefore, a higher harmonic Wave 1 or 3 which travels eastward at the same angular frequency as the traveling Wave 2 (ω_2) may be generated by the wave-wave interaction. However, to our knowledge, there is no study on the horizontal structure variations concerning the wave-wave interaction in the SH stratosphere.

This work aims to investigate quasi-periodic variations of the polar vortex through wave-wave interactions between Wave 1 and Wave 2, using the NCEP/NCAR Reanalysis dataset. I use the daily data for 24 years from 1979 to 2002 as Chapter 2. Waves are divided into stationary (time averaged) component and transient (deviation from the time mean) component, and time variations of their horizontal structures are studied to capture the nature of the wave-wave interactions. I also use a spherical barotropic model to understand the dynamical elements that produce such periodic variations of the polar vortex.

A detailed analysis for a typical example of the observed wave-wave interactions will be shown in the next section, and the result of the model experiment similar to the observation is described in Section 4.3. In Section 4.4, the interannual variations of the wave-wave interactions are investigated. Discussion is in Section 4.5, followed by the conclusions in Section 4.6.

4.2 A typical case in October 1996

In this section, I focus on a typical period for the 20 days from 8th to 27th in October 1996, during which quasi-periodic variations of the polar vortex were observed clearly.

4.2.1 Latitudinal structure of zonal mean states

Figure 4.1(a) shows the latitudinal profile of the time averaged zonal mean zonal wind $\langle \bar{u} \rangle$ (solid line) in the SH at 20 hPa level for this period, where $\langle A \rangle$ denotes the time mean of

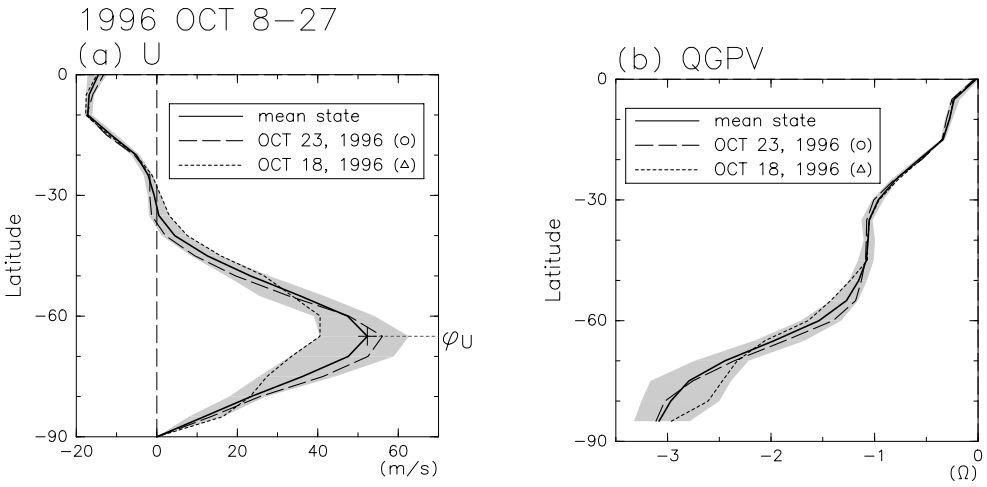

Figure 4.1: Latitudinal profiles of zonal mean zonal wind (a) and zonal mean QGPV (b) at 20 hPa for the 20-day period from October 8th to 27th in 1996. The solid line shows the time mean state along with the variation range for each latitude (shaded region). The broken and dashed lines show the profiles on 23rd and 18th, respectively. The value of the QGPV is scaled by the rotation rate of the earth $\Omega = 7.292 \times 10^{-4}$ s^{-1}.

A and $\bar{A}$ the zonal mean. The maximum speed of the polar night jet exceeds 50 m s^{-1} at $\phi_U = 65°$S where the time variation (shaded region) is also the largest. The latitudinal profile of the time averaged zonal mean quasi-geostrophic PV (hereafter QGPV), $\langle \bar{q} \rangle$ at 20 hPa (Fig. 4.1b) shows a monotonic increase with latitude ϕ. It is nearly constant in mid-latitudes in contrast to the large gradient ($\frac{\partial \langle \bar{q} \rangle}{\partial \phi}$) in the high-latitudes around the latitude of the jet core. Broken and dashed lines indicate these profiles when the zonal mean zonal wind is strong (23rd) or weak (18th) at ϕ_U, respectively. The zonal mean zonal wind on 23rd is stronger than that on 18th in the high-latitudes, whereas weaker on the equator side of 55°S. Corresponding to this, $\frac{\partial \langle \bar{q} \rangle}{\partial \phi}$ on 23rd is larger than the time mean state in the high-latitudes and slightly negative in the mid-latitudes around 40°S, while on 18th it is smaller than the mean state in the high latitudes and nearly zero in the mid-latitudes.

4.2.2 Horizontal patterns

Figure 4.2(a) shows the time mean state of the QGPV field at 20 hPa for the 20 days. The polar vortex is displaced off the pole with a circular pattern, indicating the dominance of Wave 1 for the stationary component. As to the time evolution (Fig. 4.2b-f), the elongated polar vortex rotates eastward with a period of about six days, changing its shape quasi-periodically. The polar vortex on 8th is roughly circular, and it is stretched along 90°E - 90°W lines on 10th. After that, it becomes less elongated, and its shape on 14th is roughly circular again similar to that on 8th. These quasi-periodic variations are observed throughout the analyzed 20 days.

Eddies ($A' = A - \bar{A}$) are divided into stationary waves defined as zonal asymmetries in the time means ($\langle A' \rangle$) and transient waves defined as the deviations from the time

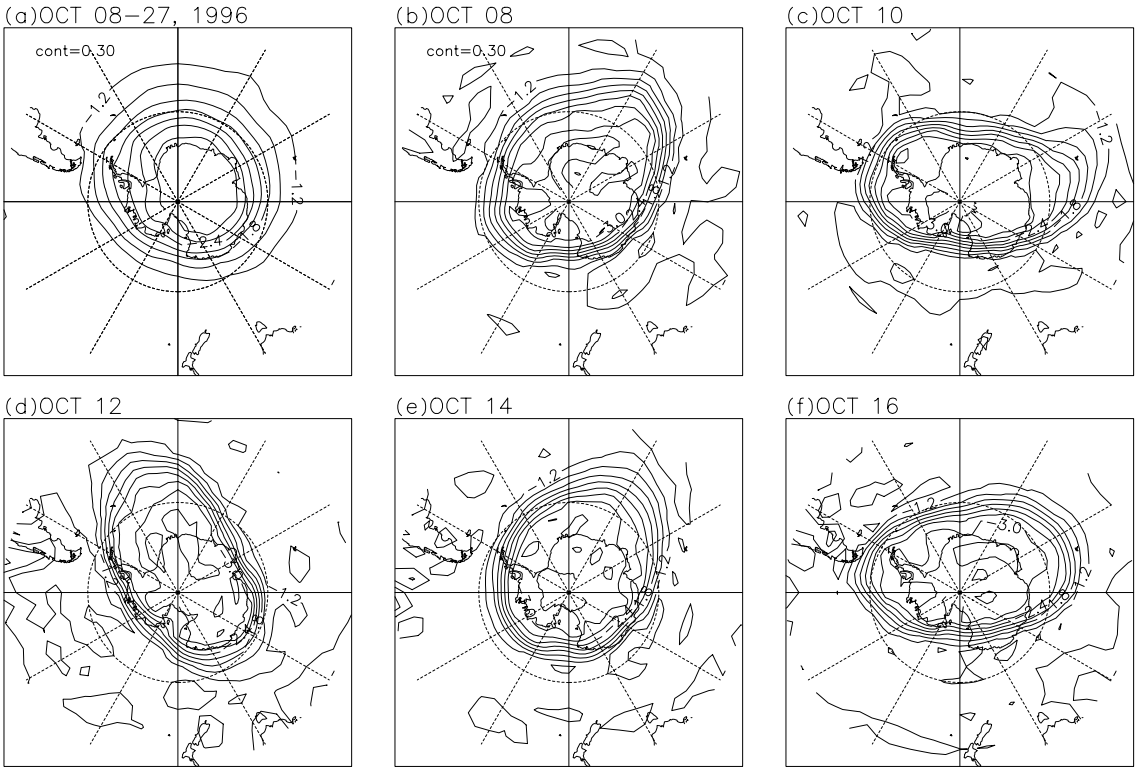

Figure 4.2: QGPV field at 20 hPa averaged for the 20-day period from Oct 8th to 27th in 1996 (a) and its time evolution (b-f) on the poleward side of 35°S. The value is scaled by Ω and the contour interval is 0.3.

means ($A'^* = A' - \langle A' \rangle$), and Fourier decomposition is taken in longitudes to obtain their component for each zonal wavenumber. Horizontal patterns of Wave 1 and Wave 2 are displayed in Figs. 4.3 and 4.4, respectively. The stationary Wave 1 (Fig. 4.3a) has much larger amplitude than the stationary Wave 2 (Fig. 4.4a), and has its maximum at ϕ_{SW1} =65°S. Transient Wave 2 (Fig. 4.4b-f), which has a much larger than the stationary component, rotates eastward with the phase speed of about 30° day^{-1}, corresponding to the rotation of the elongated polar vortex (Fig. 4.2b-f). During 8th-12th (Fig. 4.4b and d), the phase tilt with latitude of the transient Wave 2 changes from southeast-northwest to southwest-northeast. Opposite variation of the phase tilt is also seen from 12th to 16th.

Transient Wave 1 (Fig. 4.3b-f) rotates eastward with the period of about six days. It has comparable amplitude to the stationary Wave 1 component and has a nodal structure in latitudes with a secondary maximum in mid-latitudes. The dashed lines in Fig. 4.3 indicate the latitudes at which the time mean amplitude of the transient Wave 1 has local maximum, ϕ_{TW1P} =75°S and ϕ_{TW1E} =55°S. On 8th (Fig. 4.3b) and 14th (Fig. 4.3e), the transient Wave 1 shifts poleward, while it shifts equatorward on 10th (Fig. 4.3c) and 16th (Fig. 4.3f). The phase tilt of Wave 1 also changes periodically: On 8th and 14th, the phase tilts from southwest to northeast, while it does quite slightly on 10th and 12th. Hereafter I call transient Wave 1 " traveling Wave 1" and transient Wave 2 " traveling Wave 2" to

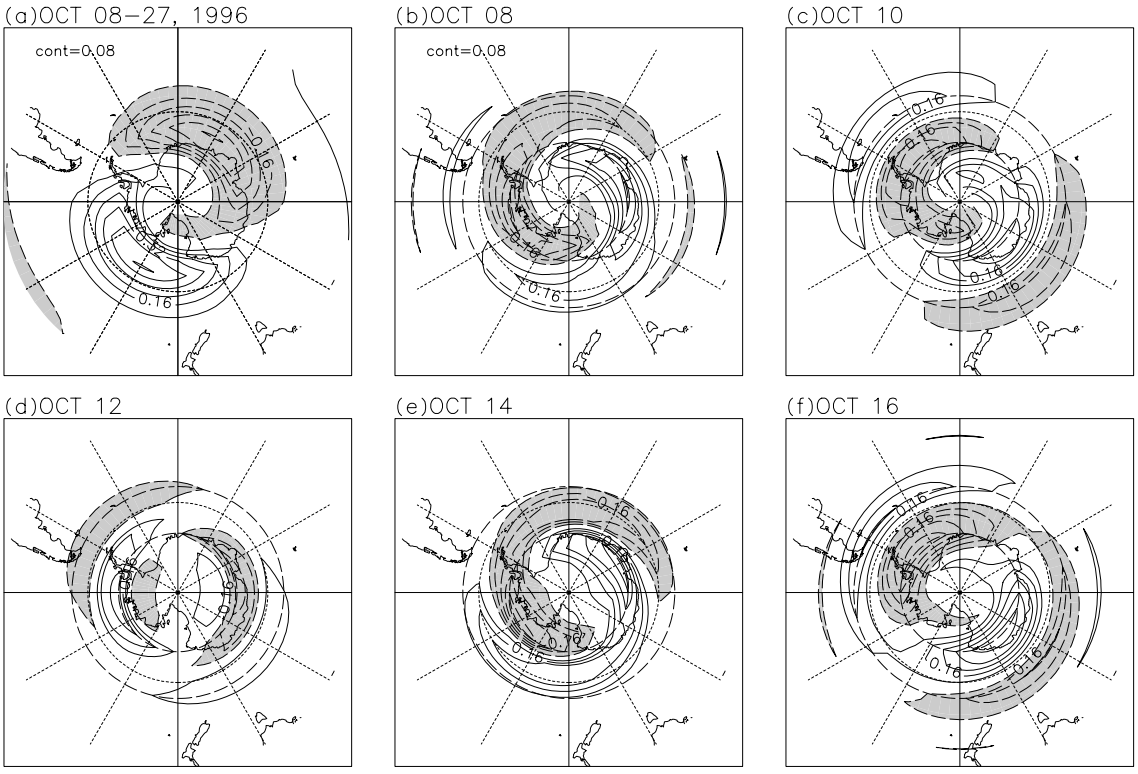

Figure 4.3: Vorticity field of stationary Wave 1 at 20-hPa (a) and time evolution of transient Wave 1 (b-f) for the 8-day period from Oct 8th to 16th in 1996. The value is scaled by Ω and the contour interval (*cont*) is 0.08. Zero lines are not drawn and the areas where the value is smaller than $-cont$ are shaded.

specify the characteristics of the waves.

4.2.3 Time mean spatial structure

Time mean structures of the dominant waves are displayed in Fig. 4.5. The vertical structure of stationary Wave 1 at ϕ_{SW1} (Fig. 4.5a bottom) reveals westward phase tilt with height above 100 hPa, indicating upward propagation of the stationary Wave 1 in the lower stratosphere. To illustrate the structure of the traveling Waves 1-3 (Fig. 4.5b-d), composites for the 20-day data are made by shifting the sections zonally so as to align the wave phase at a reference latitude at 20 hPa level. I select the reference as the latitude where the time mean amplitude of each wave is maximum at that level; ϕ_{TW1P} =70°S for Wave 1, ϕ_{TW2} =60°S for Wave 2, and ϕ_{TW3E} =60°S for Wave 3. The characteristics shown here are obtained in case that the reference level is selected above 150 hPa, while not obtained when the reference level is set in the upper troposphere. The composite of traveling Wave 2 has phase tilt from southeast to northwest and is roughly equivalent barotropic between 30 and 10 hPa, while it tilts westward with height between 150 and 50 hPa. The composite of traveling Wave 1 has a node around 62.5°S, between ϕ_{SW1} and ϕ_{TW2}, with the maxima at ϕ_{TW1P} and ϕ_{TW1E}; the amplitude in the pole-side is much larger. The traveling Wave 1 has phase tilt from southwest to northeast contrary to the Wave 2 and

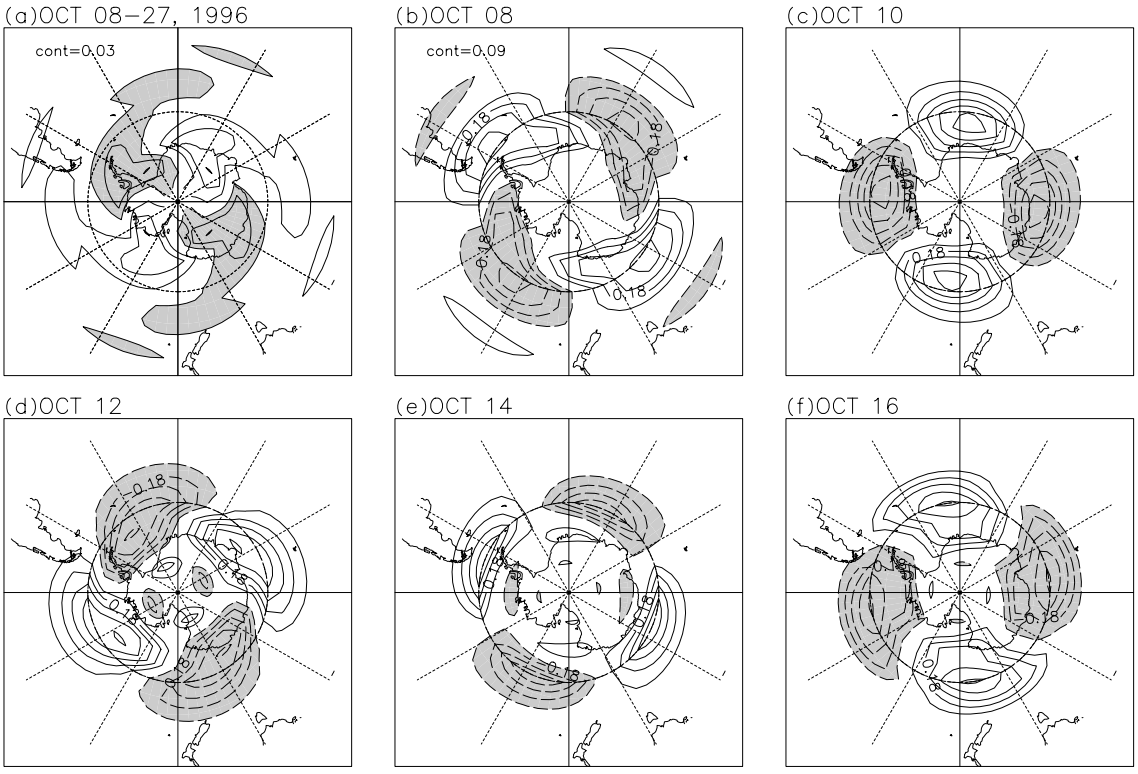

Figure 4.4: Same as in Fig. 4.3 but for Wave 2. The contour intervals (*cont*) are 0.03 for stationary wave and 0.09 for transient wave. Zero lines are not drawn and the areas where the value is smaller than $-cont$ are shaded.

is roughly equivalent barotropic in the stratosphere. The composite of traveling Wave 3 also shows a nodal structure with the maxima at ϕ_{TW3P} =75°S and ϕ_{TW3E} =60°S. The latitudinal structures of the traveling Waves 1 and 3 satisfy the relation of Eq. (4.1); the traveling Waves 1 and 3 with a node can be regarded as higher harmonic waves generated by wave-wave interaction between the stationary Wave 1 and the traveling Wave 2.

The Eliassen-Palm (EP) flux vector represents the wave structure more quantitatively. For wave fields satisfying the quasi-geostrophic conditions, the EP flux vector $\mathbf{F}(\phi, p, t) = (0, F_\phi, F_p)^{\mathbf{T}}$ are described as the products of the stationary ($\langle A \rangle$) and transient (A^*) components:

$$
\begin{aligned}
\mathbf{F}\left(\phi, p, t\right) &= \sum_{k=1}^{\infty} \mathbf{F}_k \\
&= \sum_{k=1}^{\infty} \begin{pmatrix} 0 \\ F_{\phi_k} \\ F_{p_k} \end{pmatrix} = \sum_{k=1}^{\infty} \begin{pmatrix} 0 \\ \rho_0 a \cos\phi \left\{ \overline{\langle u_k \rangle \langle v_k \rangle} + \overline{\langle u_k \rangle v_k^*} + \overline{u_k^* \langle v_k \rangle} + \overline{u_k^* v_k^*} \right\} \\ \rho_0 a \cos\phi \, \frac{f}{\theta_{0z}} \left\{ \overline{\langle \theta_k \rangle \langle v_k \rangle} + \overline{\langle \theta_k \rangle v_k^*} + \overline{\theta_k^* \langle v_k \rangle} + \overline{\theta_k^* v_k^*} \right\} \end{pmatrix} \\
&= \sum_{k=1}^{\infty} \left\{ \mathbf{F}_k^{\langle\rangle\langle\rangle} + \mathbf{F}_k{}^{\langle\rangle *} + \mathbf{F}_k{}^{*\langle\rangle} + \mathbf{F}_k{}^{**} \right\}, \qquad (4.3)
\end{aligned}
$$

where subscript k for each quantity denotes the component associated with zonal wavenum-

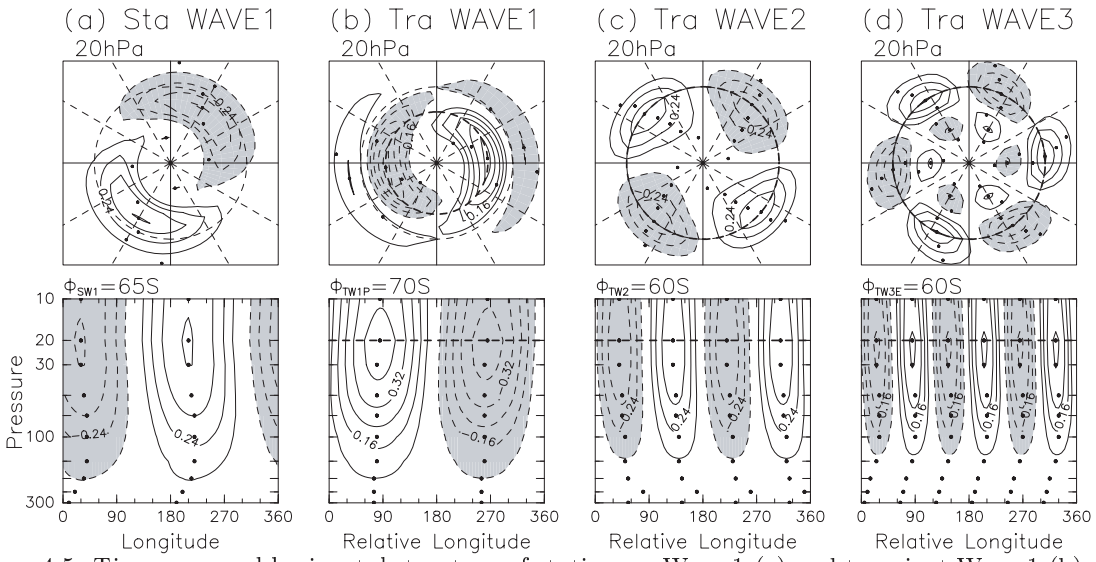

Figure 4.5: Time averaged horizontal structure of stationary Wave 1 (a) and transient Wave 1 (b), Wave 2 (c) and Wave 3 (d) at 20 hPa (upper panels) for the 20-day period from Oct 8th to 27th in 1996. Reference latitudes for transient waves to make composite are selected at 70°S, 60°S and 60°S, respectively, where the time mean amplitude is maximum at the 20-hPa level and drawn with the dashed lines. The vertical structure of the stationary Wave 1 at 65°S and the composite vertical structures of transient Waves 1, 2, and 3 at the reference latitude are shown in each lower panel. The contour intervals (*cont*) are 0.12 for stationary Wave 1 and transient Wave 2, and 0.08 for transient Wave 1 and Wave 3. Zero lines are not drawn and the areas where the amplitude is smaller than $-cont$ are shaded.

ber k, and the other notations are same as Andrews et al (1987). The EP flux vector for the wave of the zonal wavenumber k, $\mathbf{F}_k = (0, F_{\phi k}, F_{pk})^{\mathbf{T}}$, is divided into four components: ${\mathbf{F}_k}^{\langle\rangle\langle\rangle}$ and ${\mathbf{F}_k}^{**}$ arise from the stationary and transient wave components, respectively, while ${\mathbf{F}_k}^{\langle\rangle *}$ and ${\mathbf{F}_k}^{*\langle\rangle}$ arise from cross terms between these components. As $\langle {\mathbf{F}_k}^{\langle\rangle *} \rangle = \langle {\mathbf{F}_k}^{*\langle\rangle} \rangle = \mathbf{0}$, $\langle {\mathbf{F}_k}^{**} \rangle$ is a rough measure of the time averaged activity of the transient waves of zonal wavenumber k, and the ratio of the horizontal and vertical components give a measure of the relative importance of barotropic and baroclinic processes associated with each traveling wave.

Figure 4.6 shows the latitude-height sections of $\langle {\mathbf{F}_k}^{**} \rangle$ and its divergence for $k = 1$ (b), $k = 2$ (c), and $k = 3$ (d) together with that of the time mean zonal mean zonal wind $\langle \bar{u} \rangle$ (a). Note that the divergence is a wave driving of the zonal mean zonal angular momentum per unit volume: $\rho a \cos\phi \frac{\partial \bar{u}}{\partial t} = \nabla \cdot \mathbf{F}$. In the middle stratosphere, there are common features for Waves 1-3 that the horizontal components are prominent in high-latitudes and that the divergences have dipole structures. In case that the traveling waves are not propagated from the troposphere, but are generated in the stratosphere, dominance of the horizontal component of the EP flux is expected for each wave. The EP flux vector for the traveling Wave 2 directs equatorward with a node of the dipole pattern on the equator side of the jet core (Fig. 4.6a), suggesting the importance of barotropic instability. The horizontal dipole of the wave driving confined in the stratosphere is a typical pattern for Wave 2 reported

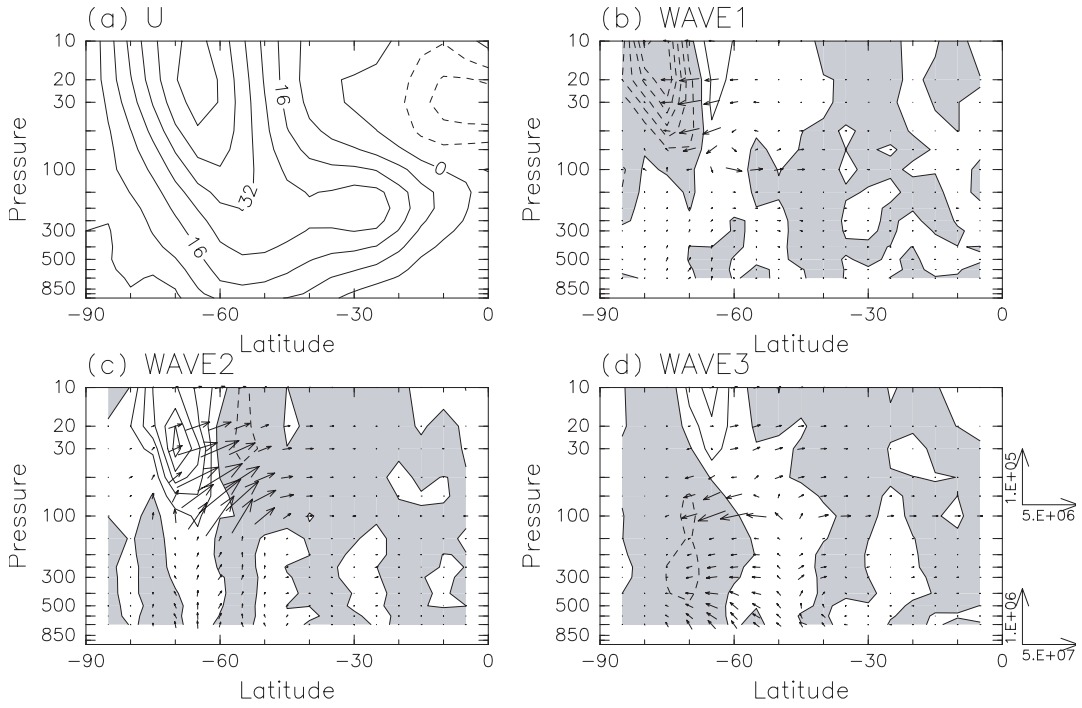

Figure 4.6: Latitude-height sections of the time mean zonal mean zonal wind $\langle \bar{u} \rangle$ at 65°S for the 20-day period from Oct 8th to 27th in 1996 (a), and the time mean EP flux vector consisting of the transient component $\langle \mathbf{F}^{**} \rangle$ and its divergence expressed as a wave driving of zonal mean zonal momentum the zonal force per unit mass for Wave 1 (b), Wave 2 (c) and Wave 3 (d). The contour interval for $\langle \bar{u} \rangle$ is 8 m s^{-1} and dashed lines indicate negative value. The contour interval for the wave driving is 0.8 m s^{-1} day^{-1} and negative values are shaded. The length of the unit vector is displayed on the right-hand-side of the graph (d). Note that the scaling of the unit vector below 100 hPa is ten times as large as that at and above 100 hPa.

in previous papers in the monthly mean fields in winter and spring (e.g., Hartmann et al. 1984; Manney et al. 1991a). As to the traveling Wave 1, the EP directs poleward and the wave driving has the opposite sign in high-latitudes (Fig. 4.6b). The EP flux vector for Wave 3 (Fig. 4.6d) directs equatorward on the equator side of the jet core and poleward on the pole side in the middle stratosphere. The EP flux vectors in the lowermost stratosphere for traveling Waves 2 and 3 seem to be related to the tropospheric wave activity, but I focus only on the middle stratosphere around 20 hPa in this paper.

4.2.4 Time variations

Figures 4.7(a-d) show Hovmöller diagrams at the 20-hPa level for traveling Wave 1 at ϕ_{TW1E} =55°S and ϕ_{TW1P} =70°S, traveling Wave 2 at ϕ_{TW2} =60°S, and traveling Wave 3 at ϕ_{TW3E} =60°S. The eastward traveling Wave 1 has the same phase speed of about 60°day^{-1} between ϕ_{TW1E} and ϕ_{TW1P} and has a nodal structure with out-of-phase relationship between these latitudes.

The phase speed of the eastward traveling Wave 2 is about a half of that of Wave 1, i.e., about 30°day^{-1}, while that of Wave 3 is about one third, 20°day^{-1}. In other words,

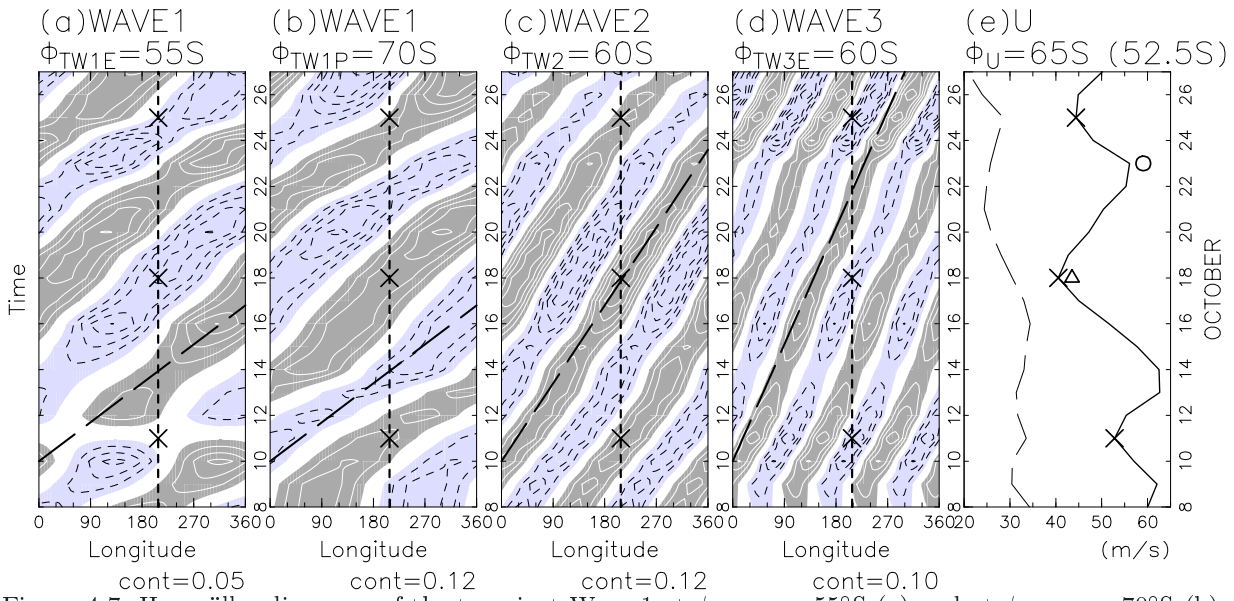

Figure 4.7: Hovmöller diagrams of the transient Wave 1 at $\phi_{TW1E} = 55°$S (a) and at $\phi_{TW1P} = 70°$S (b), Wave 2 at $\phi_{TW2} = 60°$S (c) and Wave 3 at $\phi_{TW2} = 60°$S (d) for vorticity field at 20 hPa for the 20-day period from Oct 8th to 27th in 1996. The vertical dashed line indicates the location of the ridge of the stationary Wave 1 at $\phi_{SW1} = 60°$S and the mark 'X' denotes the time when the ridge of the traveling Wave 2 at ϕ_{TW2} overlaps with the stationary Wave 1 at ϕ_{SW1}. The value is scaled by Ω and the contour intervals *cont* are denoted under each panels. Dark shade indicates above *cont* and light shade below $-$*cont*. Time evolutions of the zonal mean zonal wind at $\phi_U = 65°$S (solid line) and 52.5°S (dashed line) are also shown in (e) and the circle and triangle marks indicate the days of which the latitudinal structure is displayed in Fig. 4.1.

the periods are the same for these traveling Waves 1, 2 and 3 (about 7 days). Vertical dashed lines indicate the longitude of the ridge of the stationary Wave 1 at 65°S and the mark 'X' denotes the time when the ridge of the traveling Wave 2 at ϕ_{TW2} overlaps with the stationary Wave 1 at ϕ_{SW1}. The overlap of the ridge among the traveling Wave 1 at ϕ_{TW1P}, the traveling Wave 2 at ϕ_{TW2} and the stationary Wave 1 occurred at the same time. On the other hand, the trough of the traveling Wave 1 at ϕ_{TW1E} and that of the traveling Wave 3 at ϕ_{TW3E} overlap with the ridge of the stationary Wave 1 at the same time as denoted by 'X'. At that time, the traveling Waves 2 and 3 tend to have those maximum amplitudes, while the traveling Wave 1 tends to have its minimum amplitude.

The zonal mean zonal wind at ϕ_U =65°S at 20 hPa (solid line in Fig. 4.7e) vacillates with the same period so as to have its minimum value roughly at the same time of the phase overlap. Note that the out of phase relationship between the jet core and the mid-latitude flank of the jet is seen in broken and dashed lines in Fig. 4.1 for the two dates when $\bar{u}_{|60°\mathrm{S}}$ is strong (denoted by ◯) or weak (△).

Another way to show the periodic change of traveling waves more quantitatively is the polar diagram of the complex amplitude of each wave (e.g., Salby and Garcia 1987). The

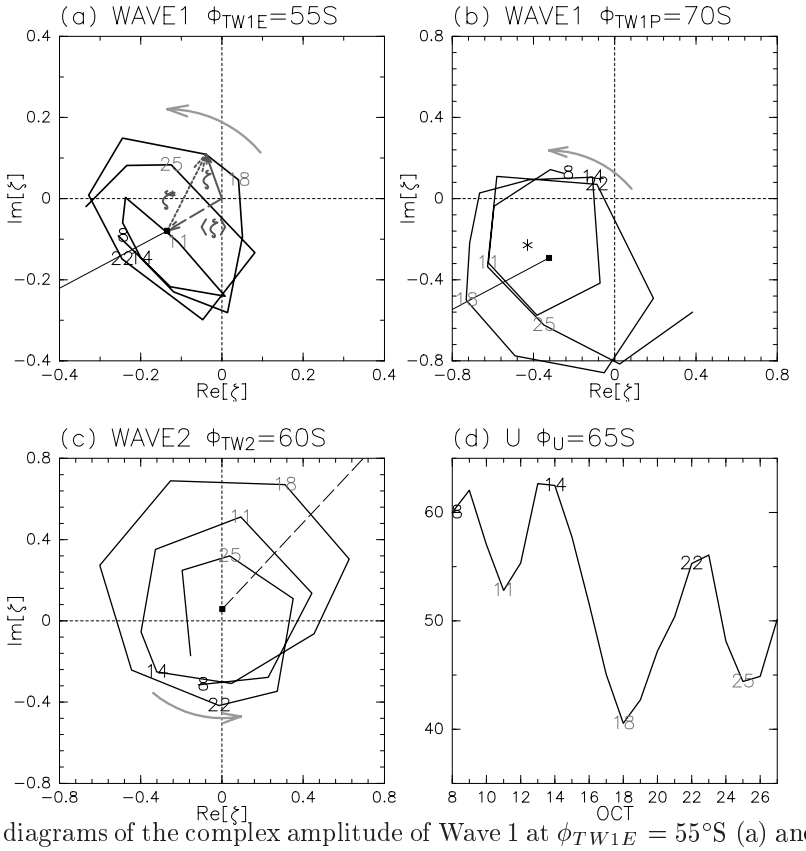

Figure 4.8: Polar diagrams of the complex amplitude of Wave 1 at $\phi_{TW1E} = 55°$S (a) and at $\phi_{TW1P} = 70°$S (b), and Wave 2 at $\phi_{TW2} = 60°$S (c) at 20 hPa for the selected 20 days. Square marks indicate the stationary component (i.e. the time mean value). Asterisk mark $*$ indicates the stationary component at $\phi_{SW1} = 65°$S and thin lines passing through the square mark in (a) and (b) and the dashed line in (c) are the phase of the stationary Wave 1. Time evolution of the zonal mean zonal wind at $\phi_U = 65°$S is also shown in (d). Labels correspond to the date when the transient Wave 1 at ϕ_{TW1P} is in phase (black) or out of phase (gray) with the stationary Wave 1 at ϕ_{SW1}.

vorticity field can be decomposed in Fourier series with zonal wavenumber k:

$$\zeta = \sum_{k=0}^{K} \mathrm{Re}\left[\zeta_k(\phi, p, t) \exp\left(ik\lambda\right)\right] = \zeta_0(\phi, p, t) + \sum_{k=1}^{K} \left[|\zeta_k(\phi, p, t)| \cos\left\{(k\lambda - \arg[\zeta_k])\right\}\right] \quad (4.4)$$

Figure 4.8(a)-(c) shows the trajectory of $\zeta_k(\phi_i, p_j, t)$ for given ϕ_i and p_j in a Re[ζ_k]-Im[ζ_k] plane, and $|\zeta_k|$ means the amplitude of the wave and arg[ζ_k] means its phase. In Fig. 4.8(a) the total wave vector $\zeta_1(\phi_{TW1E}, 20\text{ hPa}, t)$ is decomposed as the stationary Wave 1 vector $\langle\zeta_1(\phi_{TW1E}, 20\text{ hPa})\rangle$ plus the traveling Wave 1 vector ${\zeta^*}_1(\phi_{TW1E}, 20\text{ hPa}, t)$ (that is, $\zeta_1 = \langle\zeta_1\rangle + {\zeta^*}_1$). The stationary Wave 1 at ϕ_{SW1} =65°S is indicated by the asterisk mark in Fig. 4.8(b), and half lines passing through the square point of $\langle\zeta\rangle$ in Figs. 4.8(a) and (b) have the same phase of the stationary Wave 1. The dashed line in Fig. 4.8(c) also shows the phase angle of the stationary Wave 1 in the polar diagram of Wave 2 ($2\arg\langle\zeta_1\rangle$). The phase relationship seen in Fig. 4.7 can be reconfirmed: The transient components of Waves 1 and 2 rotate counterclockwise with the period of about seven days, (or roughly three

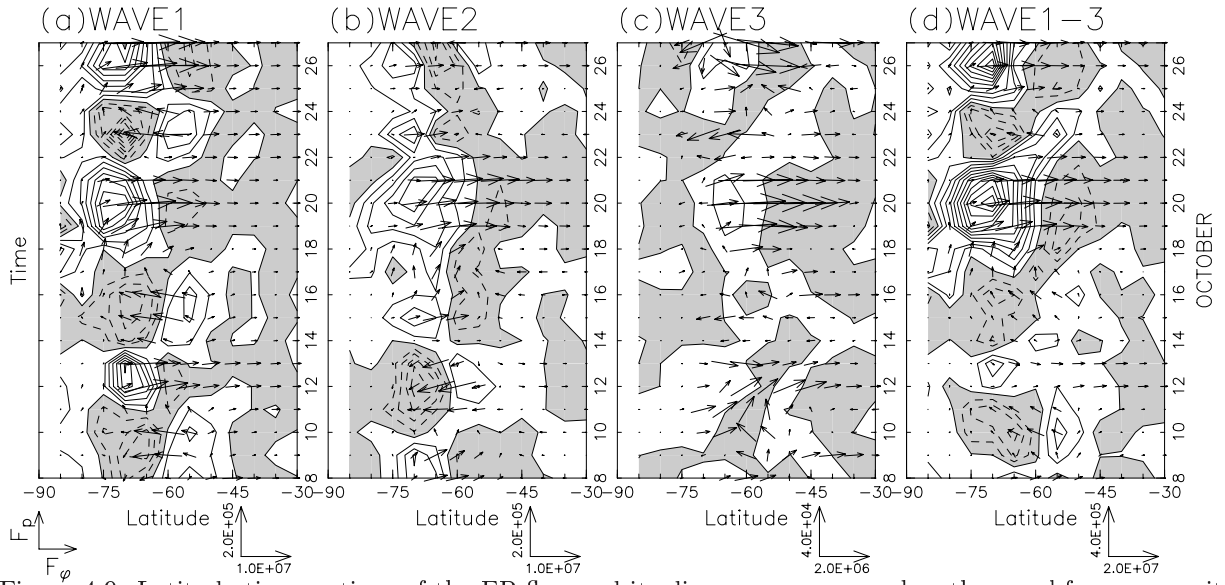

Figure 4.9: Latitude-time sections of the EP flux and its divergence expressed as the zonal force per unit mass for Wave 1 (a), Wave 2 (b), Wave 3 (c) and Wave1-3 (d) at 20 hPa for the selected 20 days. The length of the unit vector is displayed under each graph. The contour interval is 0.8 m s^{-1} day^{-1} and negative values are shaded.

rotations for 20 days.) The phase difference between the traveling component at ϕ_{TW1E} and that at ϕ_{TW1P} is always about π, indicating the out-of-phase relationship between the two latitudes. (Note six particular days denoted with the same black or gray numbers.) The traveling Wave 1 vector at ϕ_{TW1P} and Wave 2 vector at ϕ_{TW2} are almost parallel to the stationary Wave 1 vector at the same time (dates in gray numbers), and the traveling Wave 1 vector at ϕ_{TW1P} is almost anti-parallel, indicating the same timing of the overlap of these waves.

These polar diagrams enable us to capture the amplitude information easier. Figures 4.8(a) and (b) show the traveling Wave 1 component is comparable to the stationary Wave 1. The orbits of the total Wave 1 are elongated in a direction perpendicular to the stationary Wave 1 vector, indicating that the traveling Wave 1 has its minimum amplitude when it is in phase or out of phase with the stationary Wave 1 and has its maximum amplitude when the phase difference between the stationary Wave 1 and the traveling Wave 1 is about $\pm\pi/2$. If we see the amplitude variation of the total wave at high-latitudes, the amplitude of Wave 1 (Fig. 4.8b) has its maximum when the overlap of these waves takes place (dates in gray numbers), consistent with the earlier studies by Hirota et al. (1990) and Shiotani et al (1990). The amplitude of the total Wave 2 (Fig. 4.8c), which is dominated by the traveling component, also tends to be the maximum when the traveling Wave 2 is in phase with the stationary Wave 1. The time variation of zonal mean zonal wind at ϕ_U is shown in Fig. 4.8(d) again to confirm that it is weakest when the traveling Wave 1 at ϕ_{TW1P} is in phase with the stationary Wave 1, while it is strongest when the traveling

Wave 1 at ϕ_{TW1P} is in opposite phase to the stationary Wave 1.

Quasi-periodic variations of the phase tilt of Waves 1 and 2 as shown in Figs. 4.3 and 4.4 suggest that the EP flux also fluctuates quasi-periodically. Figure 4.9(a) shows the time change of the EP flux for Wave 1 ($\mathbf{F}_1$) and its divergence at 20 hPa level. The horizontal component F_{ϕ_1} is relatively large in high-latitudes and changes its direction quasi-periodically associated with the phase relation between the stationary and traveling Wave 1. Corresponding to this feature, the dipole pattern of the divergence with a node around 60°S also changes its sign quasi-periodically. The divergence or convergence has peaks around ϕ_{TW1P} or ϕ_{TW1E} at the timing that the amplitude of the traveling Wave 1 is maximum, (that is, the traveling Wave 1 vector is perpendicular to the stationary Wave 1 vector.) Interference between the stationary wave and a monochromatic traveling wave can produce this kind of periodic fluctuation of the EP flux (cf. Salby and Garcia 1987). An example of the interference between a normal mode Rossby wave known as "5-day wave" and the forced stationary planetary wave was reported by Hirooka (1986). The dominance of the terms $\mathbf{F}_1^{\langle\rangle *}$ and $\mathbf{F}_1^{*\langle\rangle}$ in $\mathbf{F}_1$ (not shown) is the evidence that the interference between the stationary Wave 1 and the induced traveling Wave 1 by wave-wave interaction causes the quasi-periodic variation of the EP flux. A hint of similar periodicity is also seen for $\mathbf{F}_3$ (Fig. 4.9c). It points to the same direction as $\mathbf{F}_1$, though the dipole pattern of the divergence is not clearly seen.

As for the Wave 2 (Fig. 4.9b), the horizontal component is dominant for this period except for the three days from 16-18th. For the first half of the period, $\mathbf{F}_2$ also changes its direction rather periodically in the opposite direction to $\mathbf{F}_1$ with the dipole pattern of the divergence of $\mathbf{F}_2$. As the EP flux divergence of the Wave 1 component dominates, the total EP flux divergence for Waves 1-3 (Fig. 4.9d) also fluctuates quasi-periodically, consistent with the vacillation of the zonal mean zonal wind (Fig. 4.7e): The EP flux divergence at ϕ_U =65°S precedes the zonal wind by a quarter period. The anti-correlation of the zonal mean zonal wind between 65°S (solid line) and 52.5°S (dashed line) shown in Fig. 4.7(e) can be explained by the dipole structure of the EP flux divergence mainly due to the interference between the stationary Wave 1 and the traveling Wave 1 which was generated by the wave-wave interaction between the stationary Wave 1 and traveling Wave 2.

4.3 A numerical experiment

4.3.1 Model description

I use a dynamical model of the two-dimensional flow on the earth with zonal-flow forcing, dissipation and surface topography to investigate the fundamental mechanism of the quasi-periodic variation of the polar vortex due to wave-wave interaction described in the previous section. The detailed result will be reported in Chapter 5. The flow is governed by a

vorticity equation in the form

$$\frac{D}{Dt}\left(\zeta + f + \frac{hf}{H}\right) = -\alpha(\zeta - \overline{\zeta_0}) + \nu\left(\nabla^2 + \frac{2}{a^2}\right)(\zeta - \overline{\zeta_0}), \tag{4.5}$$

where $\zeta = \nabla^2\psi$ is the relative vorticity, $f = 2\Omega\sin\phi$ Coriolis parameter, Ω the rotation of the earth, h the height of the surface topography, and H the thickness of the fluid layer. The potential vorticity (hereafter noted as PV) $q = \zeta + f + (hf/H)$ is conserved following fluid motion if the forcing and dissipation terms on the right side of Eq. (4.5) can be neglected. The relaxation time α^{-1} of the forcing is set to 10 days and the viscosity coefficient ν is fixed at a small constant to give the dissipation time of 1 day at the largest total wavenumber ($N = 85$) as in Mizuta and Yoden (2001). In the SH, sinusoidal surface topography of zonal wavenumber 1 is assumed in longitudinal direction as

$$h(\lambda, \phi) = \frac{1}{2}h_0(\sin 2\phi)^2 \cos\left(\lambda - \frac{\pi}{6}\right),$$

and there is no topography in the NH. The prescribed equilibrium state for the forcing that is given by zonally symmetric vorticity $\overline{\zeta_0} = \frac{1}{a}\frac{\partial \overline{u_0}}{\partial \phi}$ is set so as to satisfy the necessary condition of barotropic instability (Hartmann 1983):

$$\overline{u_0} = \frac{1}{2}U\left(1 + \tanh\frac{\phi - \phi_0}{B}\right)\cos\phi,$$

where U is a measure of the intensity of the prescribed jet, B its width, and ϕ_0 its position.

The régime diagram in the case without the topography ($h_0 = 0$) was obtained by Ishioka and Yoden (1995). An eastward traveling Wave 2 with a constant amplitude is obtained over a wide range of the parameters. I set $U = 240$ m s^{-1} and $\phi_0 = 55°$, and sweep the parameters B and h_0. The régime diagram is shown in Chapter 5. At specific parameter ranges, the stationary Wave 1 generated by the topography is dominant, as well as the eastward traveling Wave 2 due to barotropic instability, and a periodic variation of the polar vortex occurs in the result of the interaction between these waves. In this section, I examine a result for the parameters $B = 6$ and $h_0/H = 0.08$ as an example of such a situation similar to the observed quasi-periodic variation as described in the previous section.

4.3.2 A case similar to observation

Figure 4.10 shows latitudinal profiles of the time averaged zonal mean zonal wind $\langle\bar{u}\rangle$ and PV $\langle\bar{q}\rangle$ (solid line) together with the prescribed zonally symmetric forcing (dotted line). Qualitatively similar features as the observation (Fig. 4.1) are found in mid- and high-latitudes except that the jet is stronger. The negative region of the latitudinal gradient of $\bar{q}$ disappears in the time mean state owing to the vorticity redistribution by the waves generated by the barotropic instability, and $\langle\bar{q}\rangle$ is nearly constant in mid-latitudes. When

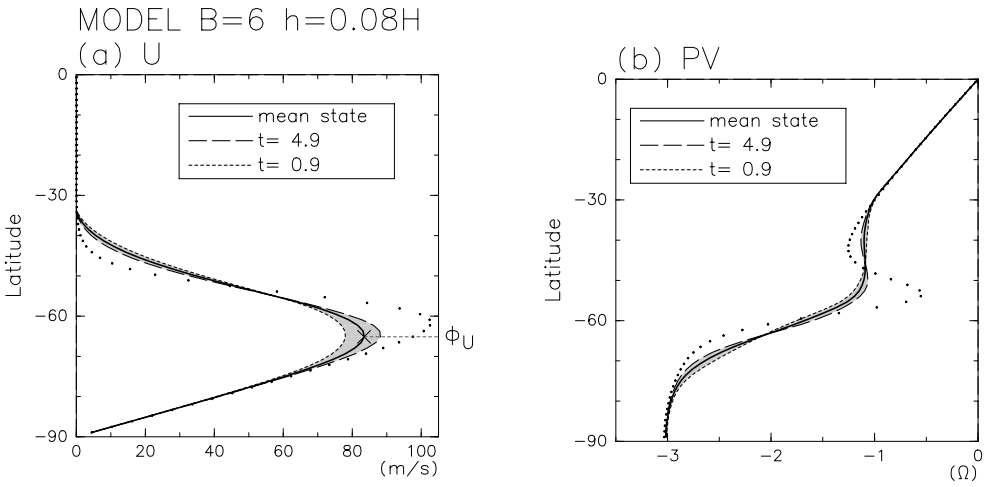

Figure 4.10: Latitudinal profiles of zonal mean zonal wind (a) and zonal mean PV (b) obtained from the barotropic model experiments with $B = 6°$ and $h_0 = 0.08H$. The solid line shows the time mean state along with the variation range for each latitude (shaded region). The dotted line shows the prescribed zonal mean forcing. The broken (dashed) line shows the profiles on $t = 4.9$ ($t = 0.9$) when the zonal mean zonal wind at the jet core ϕ_U has its maximum (minimum) value. The value of the PV is scaled by Ω.

the zonal mean zonal wind in high-latitudes is stronger than the mean state, it is weaker in mid-latitudes, or vice versa. In other words, when the gradient of PV in high-latitudes is larger than the mean state, it is smaller in mid-latitudes, or vice versa.

Horizontal structures of the Waves 1 and 2 (not shown) also have similar characteristics to the observations shown in Fig. 4.5 top: The amplitudes of stationary Wave 1 and traveling Wave 2 have only one maximum at ϕ_{SW1} =63.7°S and ϕ_{TW2} =60.9°S, respectively, while the traveling Wave 1 has double maxima at ϕ_{TW1E} =55.3°S and ϕ_{TW1P} = 66.5°S with a node between the two latitudes.

Figure 4.11 displays the polar diagram of the complex amplitudes for Wave 1 at ϕ_{TW1E} (a) and ϕ_{TW1P} (b) and that for Wave 2 at ϕ_{TW2} (c), as well as the time variation of the zonal mean zonal wind at the latitude of the jet core, ϕ_U = 65.1°S (d). Dominance of stationary Wave 1 and traveling Wave 2 resembles the observed state as shown in Fig. 4.8. This is a purely periodic solution which has similar characteristics to the observed quasi-periodic variations as follows: (1) Transient Wave 1 propagates eastward with the same period as Wave 2, keeping the out-of-phase relation between ϕ_{TW1E} and ϕ_{TW1P}. (2) The traveling Wave 1 at ϕ_{TW1P} and Wave 2 at ϕ_{TW2} are in phase with the stationary Wave 1 almost simultaneously at $t = 0.9$ and 10.6. (3) The amplitude of traveling Wave 2 at ϕ_{TW2} has its maximum at that time, whereas the traveling Wave 1 at ϕ_{TW1P} has a minimum amplitude when in phase or out of phase with the stationary Wave 1. (4) The zonal mean zonal wind is weakest when the phase overlap occurs (t = 0.9 and 10.6). Furthermore, traveling Wave 3 also propagates eastward with the same angular frequency as Waves 1 and 2, and its amplitude variation is similar to that observed (not shown).

The EP flux and its divergence for the model experiment are shown in Fig. 4.12(a-

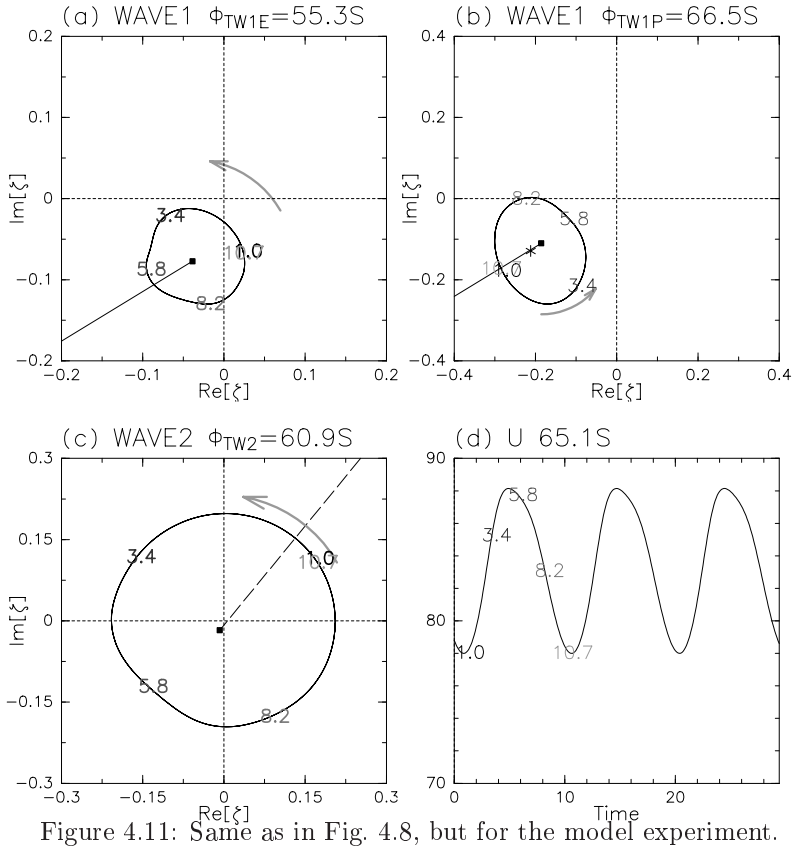

Figure 4.11: Same as in Fig. 4.8, but for the model experiment.

d), together with the time change of zonal mean zonal wind at ϕ_U =65.1°S and 51.1°S (Fig. 4.12e). Here, $\mathbf{F}_k(0, F_{\phi_k}, 0)^{\mathbf{T}} = (0, -\overline{u_k v_k}, 0)^{\mathbf{T}}$. Features of the EP flux are also similar to those observational results: (1)The EP flux for Wave 1, $\mathbf{F}_1$, changes its direction periodically associated with the phase relation between the stationary Wave 1 and traveling Wave 1, thus the dipole pattern of the divergence with a node around 60°S also changes its sign periodically. (2)$\mathbf{F}_2$ also changes its direction periodically in the opposite direction to $\mathbf{F}_1$ with the dipole pattern of the divergence as seen in Fig. 4.9b for the first half of the period. (3) $\mathbf{F}_3$ is small compared to the other two components but shows periodic change of its direction. (4) The EP flux divergence of the Wave 1 component dominates the EP flux divergence for the Waves 1-3, which explains the anti-correlated time change of the zonal mean zonal wind between 65.1°S (solid line) and 51.1°S (dashed line). Only one difference of the EP flux in the model experiment from the observation is that the EP flux for the Waves 1-3 is always convergent between 55°S and 60°S, which is due to the fact that the EP flux convergence of Wave 2 there is larger than the divergence of Wave 1. All the evidences presented here show that the observed traveling Waves 1 and 3 as described in the previous section are consistent with the traveling waves generated by the wave-wave interaction of the stationary Wave 1 and the traveling Wave 2.

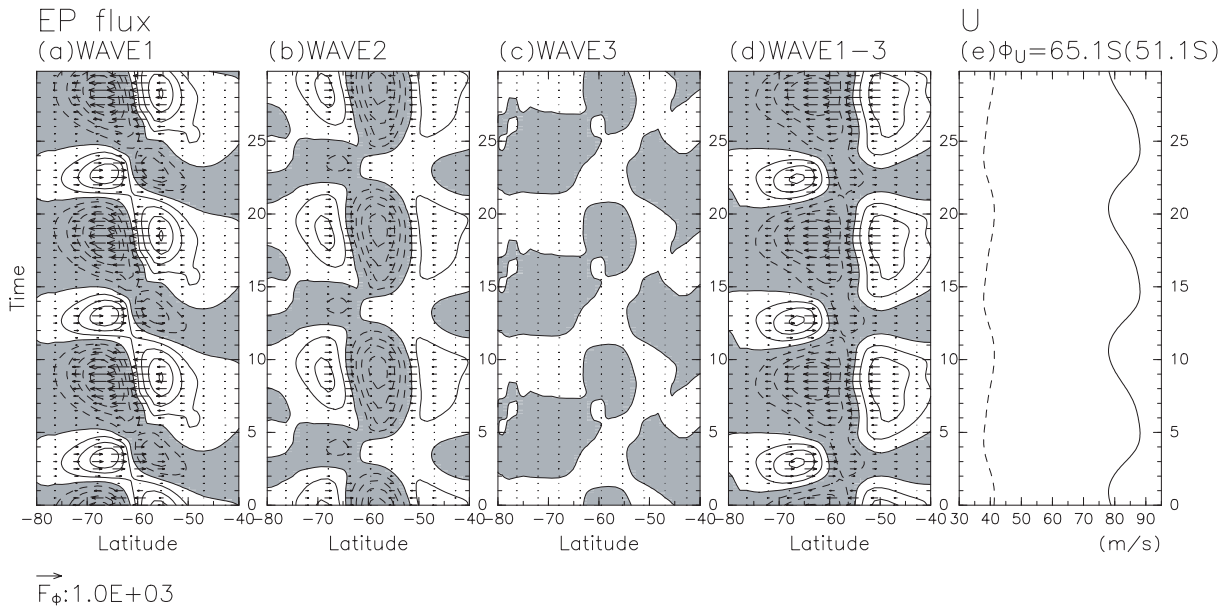

Figure 4.12: (a-d) Same as in Fig. 4.9, but for 30 days for the model experiment. The length of the unit vector is displayed under the graph (a). The contour interval is 0.8 m s^{-1} day^{-1} and negative values are shaded. (e) Time evolution of the zonal mean zonal wind at $\phi_U = 65.1$°S (solid line) and 51.1°S (dashed line) for the model experiment. The length of the unit vector is displayed under the graph.

4.4 Interannual variability

Returning to the observation data, interannual variability of the quasi-periodic variations of the polar vortex is investigated using the 24-year data from 1979 to 2002. Figure 4.13 shows Hovmöller diagrams of the transient Wave 2 at ϕ_{TW2} (defined for each year and noted above each panel) for the 20-day period from October 8th to 27th in the 24 years, which is the same period as Fig. 4.7 for the case of 1996. Regular eastward traveling Wave 2 with comparable amplitude to that in 1996 is often observed. The latitude ϕ_{TW2} ranges from 55°S to 70°S depending on the year.

Figure 4.14 shows the complex amplitudes for Wave 1 at ϕ_{TW1P} (solid line) and Wave 2 at ϕ_{TW2} (dashed line) for eight of the years when the amplitude of the traveling Wave 2 has large amplitude: 1983, 1984, 1985, 1990, 1994, 1995, 1997, and 1998. For comparison, results for 1996 are shown in Figure 4.8. Eastward propagation of the traveling Wave 1 is clearly seen in 1983, 1984, and 1998 with the same phase relationship between the traveling Waves 1 and 2. The traveling Waves 1 tends to propagate eastward at a similar angular frequency as Wave 2 and to be in phase with the stationary Wave 1 nearly at the same timing with the phase-overlap of Wave 2 as seen in 1996. In particular, the amplitude variation in 1984 also shows similar characteristics with the case of 1996. In the other years shown in Fig. 4.14, the eastward propagation of Wave 1 can be discernible for some sub-period, although the angular frequency is largely different. This kind of relationship is not clearly seen in the years when the amplitude of traveling Wave 2 is small such as the years 1988, 2000, 2001 (not shown).

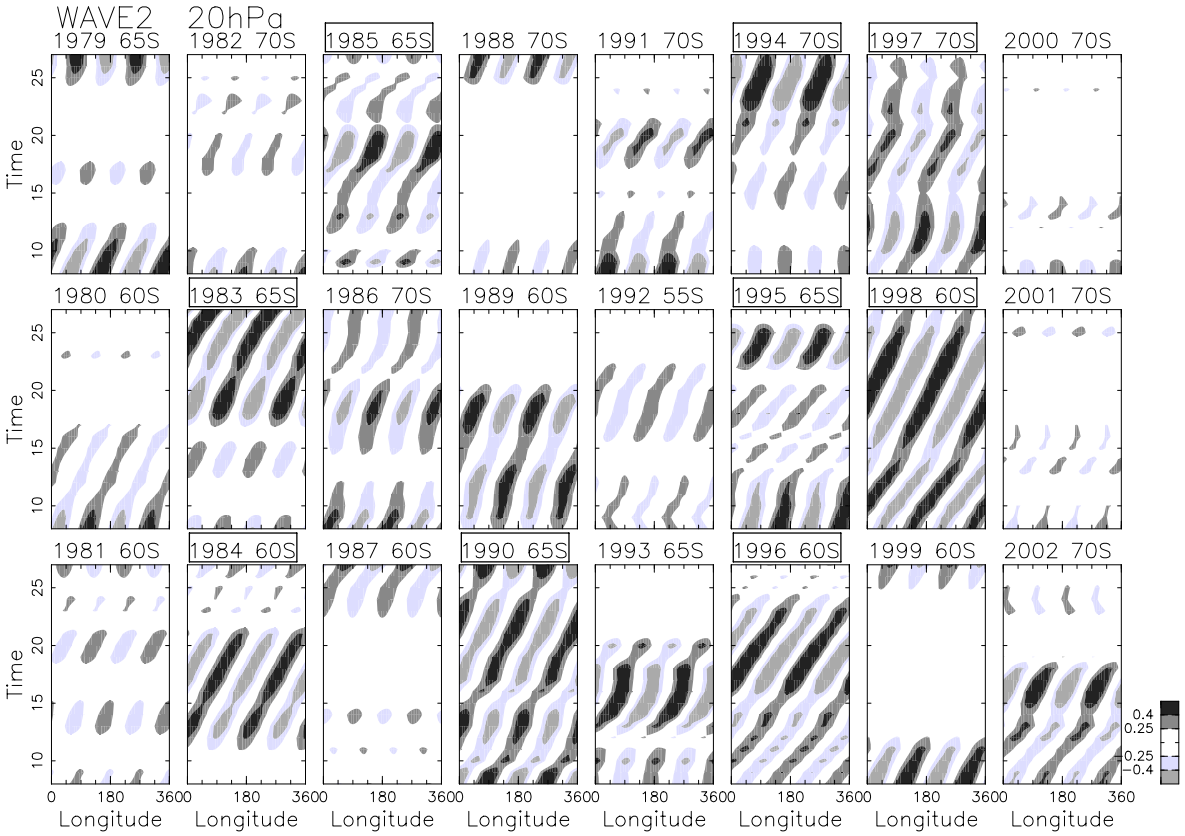

Figure 4.13: Hovmöller diagrams of the transient Wave 2 at ϕ_{TW2} for vorticity field at 20 hPa during October 8th to 27th for the 24 years from 1979 to 2002. The value is scaled by Ω. The titles are enclosed by squares for the years in which the transient Wave 2 has the nine largest amplitude.

Figure 4.15(a) shows the relation between the amplitude of the stationary Wave 1 at ϕ_{SW1} and that of the traveling Wave 2 at ϕ_{TW2} for the 24 years. The stationary Wave 1 has large interannual variability as reported by Hio and Hirota (2002) and its amplitude has weak and negative correlation with that of the traveling Wave 2 ($r = -0.39$). The amplitude of the stationary Wave 1 for the nine years with large amplitude of the traveling Wave 2 varies from year to year.

Figure 4.15(b) shows the scatter diagram between the amplitude of the traveling Wave 2 and the latitudinal difference of the time mean zonal mean QGPV between 40°S and 45°S at 20 hPa, where its latitudinal gradient is small (Fig. 4.1). For the nine years with the large amplitude, the latitudinal difference tends to be negative or small positive except for 1998. In 1986 for which the latitudinal difference is also negative, the amplitude of the traveling Wave 2 is not so small. Contrarily, the latitudinal difference of the time mean zonal mean QGPV tends to be large in other years with small amplitude of the traveling Wave 2. These suggest the generation of traveling Wave 2 by *in situ* instability of the zonal mean state when the amplitude of the traveling Wave 2 is large except for 1998. In 1998, the wave activity flux from the troposphere is very large (Fig. 4.15d), suggesting that the traveling Wave 2 is propagated from the troposphere in this year.

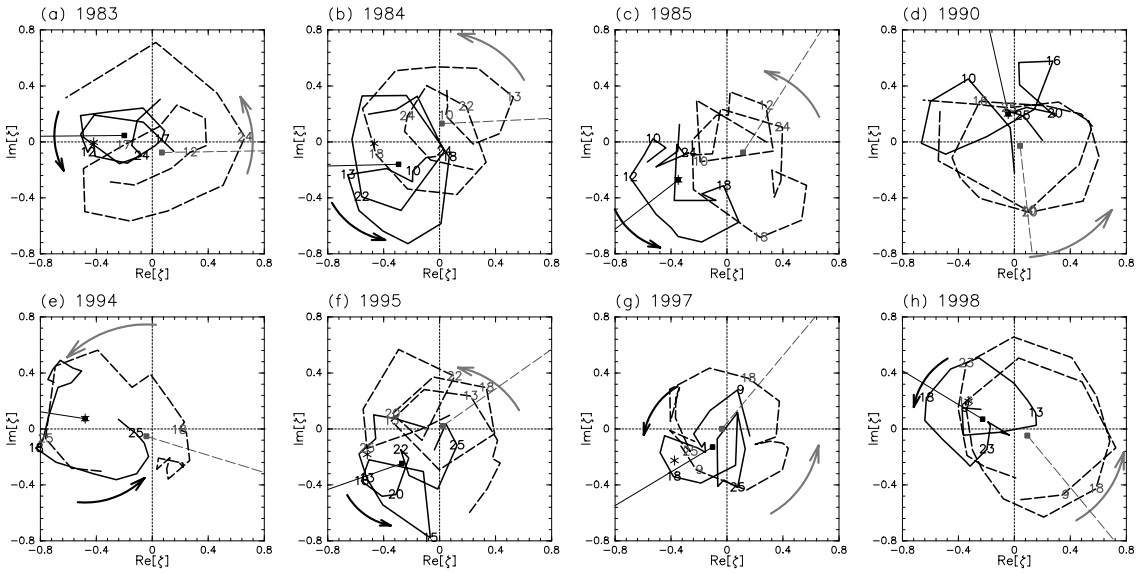

Figure 4.14: Polar diagrams of the complex amplitude of Wave 1 at ϕ_{TW1P} (solid line) and Wave 2 at ϕ_{TW2} (dashed line) for the period of 20 days from Oct 8th to 27th, 1983 (a), 1984 (b), 1985 (c), 1990 (d), 1994 (e) 1995 (f), 1997 (g) and 1998(h). The marks are same as in Fig. 4.8.

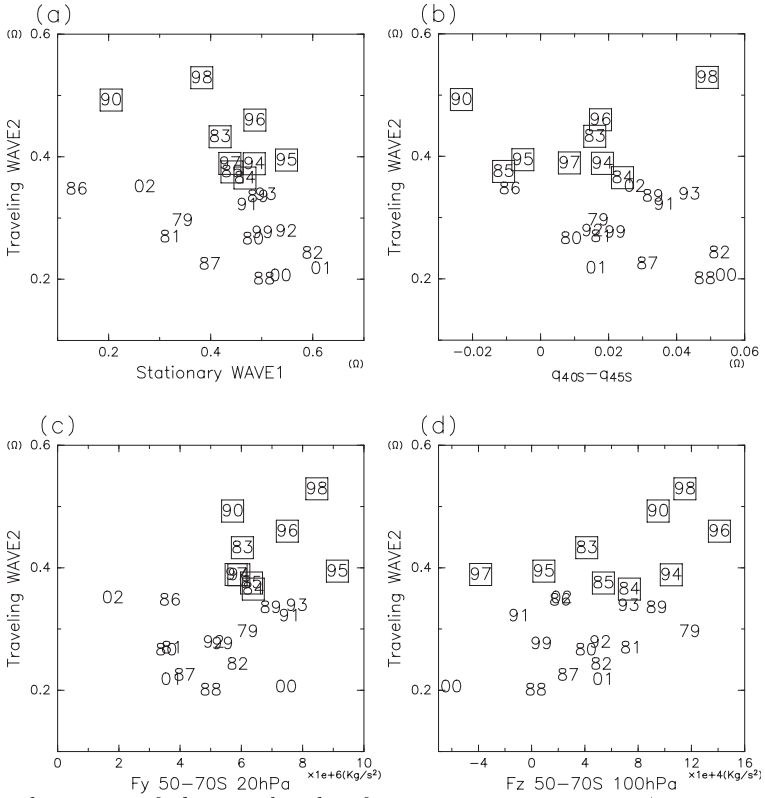

Figure 4.15: Scatter diagrams of the amplitude of stationary Wave 1 at ϕ_{SW1} versus the amplitude of transient Wave 1 at ϕ_{TW2} (a), the difference of the time mean zonal mean QGPV between 45°S and 40°S at 20 hPa (b), the time mean absolute value of the horizontal component of the EP flux of Wave 2 between 50°S and 70°S at 20 hPa (c), and the time mean vertical component of the EP flux of Wave 2 between 50° and 70°S at 100 hPa (d) for the period of 20 days from Oct 8th to 27th for each year from 1979 to 2002. Each year is indicated by the last two digits. The meaning of the frame to select the nine years is same as in Fig. 4.13. Note that ϕ_{SW1} and ϕ_{TW2} are defined for each year.

The relation of the amplitude of the traveling Wave 2 to the horizontal component of the EP flux for Wave 2 (F_{ϕ_2}) at 20 hPa between 50°S and 70°S is shown in Fig. 4.15(c). Since the horizontal component changes its sign periodically in the case of 1996 (Fig. 4.9), I take the time mean of the absolute value of F_{ϕ_2}. The horizontal component of the EP flux has a large magnitude for the nine years. On the other hand, the time mean of the vertical component of the EP flux for Wave 2 at 100 hPa between 50°S and 70°S has full range of variations for the nine years with large amplitude of the traveling Wave 2 (Fig. 4.15d). In some of the years, e.g., 1995 and 1997, the small wave activity propagated from the troposphere suggests the generation of traveling Wave 2 in the stratosphere.

4.5 Discussion

In Sections 4.2 and 4.4, I presented quasi-periodic variations of the polar vortex observed in October. The wave-wave interactions between the Waves 1 and 2 were pointed out by Hirota et al. (1990) and Manney et al. (1991a) for August and September. Figure 4.16 shows the polar diagrams of the complex amplitudes of Wave 1 at 50°S (a) and 65°S (b), and Wave 2 at 60°S (c) for the period from August 15th to September 20th in 1988, in which the quasi-periodic variation of these waves was reported by Hirota et al. (1990). We can find the similar periodic variations of the Waves 1 and 2 and the zonal mean zonal wind as seen in Fig. 4.8 in spite of the slower phase speed.

Another case of the wave-wave interaction is found in the period from August 8th to September 30th in 2002, during which on September 24th, the polar vortex split into two and a major stratospheric sudden warming event occurred in the first time for over two decades of satellite observations (Allen et al. 2003). The polar diagrams of the complex amplitudes of Wave 1 at 50°S (a) and 70°S (b), and Wave 2 at 60°S (c) are shown in Fig. 4.17.As pointed out by Scaife et al. (2004), quasi-periodic variation of Waves 1 and 2, and the zonal mean zonal wind (d) can be seen through the winter. Clustering of the dates written in black or gray shows that the eastward traveling Wave 1 at 70°S has a similar angular frequency to the Wave 2 at 60°S and is anti-correlated with that at 50°S. The clustering also shows that phase overlap of traveling Waves 1 and 2 with the stationary Wave 1 occurs roughly at the same time. These phase variations similar to those in Figs. ?? and 4.11 suggest that the quasi-periodic variation of the polar vortex before its split can be understood as a result of the wave-wave interaction between the stationary Wave 1 and the traveling Wave 2. This result is consistent with that by Manney et al (2004): They made sensitivity tests using a mechanistic model with a time-varying bottom forcing near the tropopause analyzed at the Met Office and suggested that the vacillation of the wave amplitude may arise from the wave-wave interaction between the Waves 1 and 2. Quasi-periodic variations of the polar vortex are sometimes observed in September in the other years, although the wave-wave interaction is not as clear as those in October due to slower phase speed of traveling Wave 2. Seasonal evolution of the polar vortex and strong wave

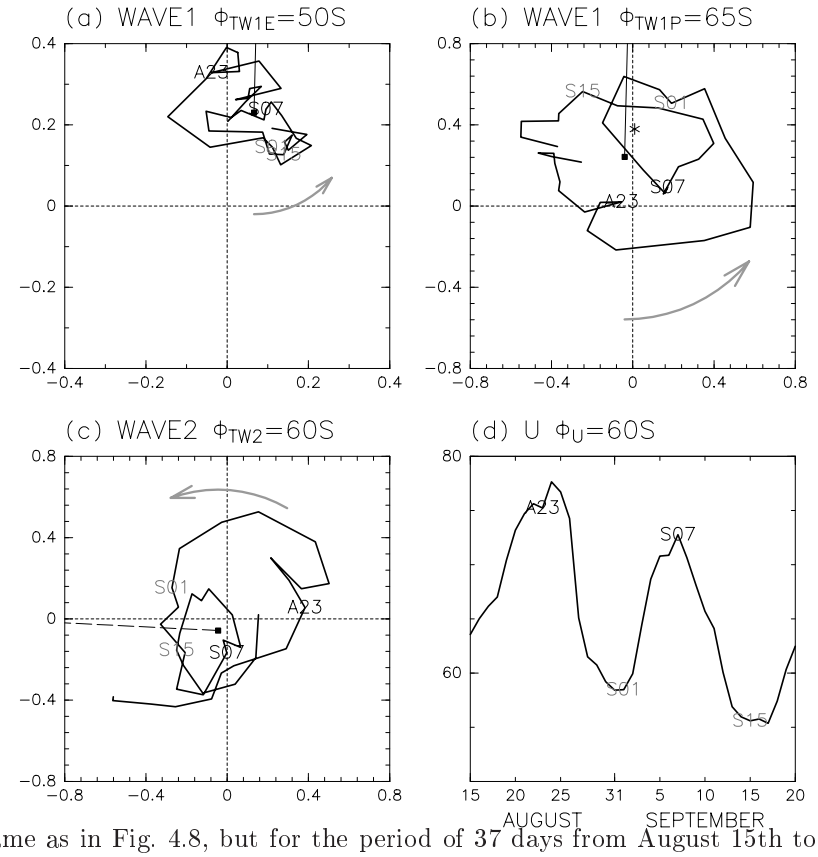

Figure 4.16: Same as in Fig. 4.8, but for the period of 37 days from August 15th to September 20th in 1988. The latitude is defined in the same way as Fig. 4.8 and is specified at the top of each panel. The labels indicate the initials of the months and dates.

activity propagated from the troposphere obscure the interaction. Seasonal evolution of the polar vortex and strong wave activity propagated from the troposphere obscure the interaction. The angular frequency of the traveling Wave 2 is much larger in 2002 than in 1988, which may be a result of much earlier seasonal evolution in August and September 2002 (Chapter 2).

4.6 Conclusions

Quasi-periodic variations of the polar vortex in the Southern Hemisphere stratosphere as shown in Fig. 4.2 were investigated from a viewpoint of the wave-wave interaction between Wave 1 and Wave 2. In a typical period for the 20 days from October 8th to 27th in 1996, the traveling Wave 1 propagates eastward with comparable amplitude to the stationary Wave 1 and the eastward traveling Wave 2 (Figs. 4.3 and 4.4). This traveling Wave 1 has a latitudinal node around 60°S where both the stationary Wave 1 and the traveling Wave 2 have maximum amplitude (Fig. 4.5). The EP flux diagnosis shows that the traveling Wave 1 is generated in the stratosphere (Fig. 4.6b).

Hovmöller diagrams (Fig. 4.7) and the polar diagrams of the complex amplitude (Fig. 4.8) reveal that traveling Waves 1 and 2 have the same angular frequency of 60° day^{-1}. The

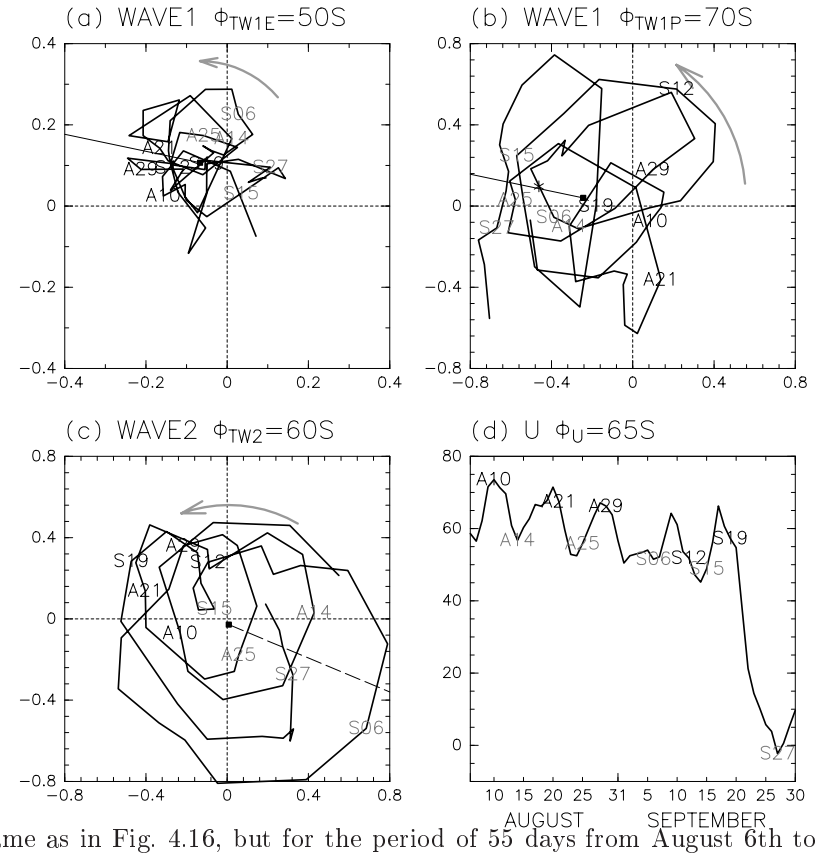

Figure 4.17: Same as in Fig. 4.16, but for the period of 55 days from August 6th to September 30th in 2002.

traveling Wave 1 in high-latitudes and the traveling Wave 2 are in phase with the stationary Wave 1 at the same time. The amplitude of the traveling Wave 2 is a maximum at this time, while the traveling Wave 1 has minimum amplitude when it is in phase or out of phase with the stationary Wave 1. The zonal mean zonal wind also vacillates quasi-periodically and has its minimum when the above mentioned phase overlapping occurs.

The EP flux for Wave 1 in the middle stratosphere also shows quasi-periodic variations due to interference between the stationary and traveling components (Fig. 4.9): The horizontal component changes its direction with the period of the eastward propagation and the divergence of the EP flux changes quasi-periodically. As the wave driving of the Wave 1 component dominates, the zonal mean zonal wind also changes quasi-periodically through the wave-mean flow interaction.

Similar periodic variations of the polar vortex are obtained in the numerical experiment with a spherical barotropic model in the circumstance that the stationary Wave 1 generated by the topographic forcing coexists with the eastward traveling Wave 2 due to barotropic instability of the forced mean zonal wind: The traveling Wave 1 with a node in mid-latitude, which is generated through the wave-wave interaction, propagates eastward at the same angular frequency as the traveling Wave 2 (Fig. 4.11). The phase relationship and the amplitude fluctuation of these waves show the same characteristics with the observation.

Furthermore, the zonal mean zonal wind vacillates with the same frequency, which is explained by the wave interference between the stationary Wave 1 and the traveling Wave 1 (Fig. 4.12). These results support that the observed quasi-periodic variations of the polar vortex can be explained by the wave-wave interaction between the stationary Wave 1 and the eastward traveling Wave 2.

In nine out of the 24 years from 1979 to 2002, similar quasi-periodic variations of the polar vortex are seen for the same 20 days in October (Fig. 4.14 and 4.15). The amplitude of the stationary Wave 1 and that of the transient Wave 2 are large in these years (Fig. 4.15a). The amplitude of the Wave 2 is well correlated with the latitudinal gradient of the zonal mean quasi-geostrophic potential vorticity in mid-latitudes (Fig. 4.15b).

It is important to know the latitudinal structures of waves and zonal mean quantities in diagnosing wave-wave interaction. The nodal structure of the traveling Wave 1 is the evidence to show the occurrence of the wave-wave interaction. Therefore, if we look at the amplitude of Waves 1 and 2 only at 60°S as in some previous studies, it would be difficult to find a clear relationship between the Waves 1 and 2 because the node of the traveling Wave 1 is located around 60°S and the latitude shifts from year to year.

Chapter 5

Periodic variations of the polar vortex due to the wave-wave interaction in a barotropic model

Abstract

Evolution of the polar vortex in a barotropic model with time independent topography of zonal wavenumber 1 is investigated for a wide range of topographic amplitude and jet profile. For narrow prescribed jets, three kinds of solutions are obtained; vacillation, periodic solution, and irregular solution. For small topographic amplitudes, the vacillating solution is obtained. Planetary waves of zonal wavenumber 2 (Wave 2) propagates eastward changing its amplitude at the commensurable frequency. For larger topographic amplitude, the flow obeys the periodic solution and the zonal flow fluctuates at the same frequency with the eastward propagation of Waves 1 and 2, whereas for still large topographic amplitude, the flow becomes irregular. At the règime transition from the vacillation to the periodic solution, the variable range of the mean zonal flow and that of the Wave-2 amplitude change those features.

The mean zonal flow fluctuates mainly due to the enstrophy exchange with Wave 2 for the vacillation. For the periodic solution, the enstrophy exchange with Wave 1 which is largely canceled out by that of Wave 2, plays the leading role in the fluctuation of the mean zonal flow.

From the enstrophy diagnosis, we found that the time change of Wave 2 for the vacillation is explained by radiative dumping, advection by time mean zonal mean zonal flow, and wave-wave interaction between the Wave 2 and Wave 4. On the other hand, for the periodic solution, the contribution of wave-wave interaction between Wave 1 and Wave 3 and that of advection by transient zonal mean flow also have large values and control the change of the enstrophy of Wave 2.

5.1 Introduction

Wave-wave interactions between the stationary Wave 1 and eastward traveling Wave 2 were reported by several authors. Hirota et al. (1990) and Shiotani et al. (1990) investigated quasi-periodic amplification of Wave 1 in late winter and found that Wave-1 amplitude

reaches its maximum when the ridges of Wave 1 and Wave 2 overlap. Following their study, I investigated quasi-periodic variations of polar vortex in terms of the wave-wave interaction in Chapter 4. The transient Wave 1, which is generated by the wave-wave interaction, travels eastward with the same angular frequency with that of the traveling Wave 2, and has a node around 60°S where these primary waves have large amplitude. The polar night jet also vacillates with the same frequency to have its minimum when the stationary Wave 1 and the transient Wave 1 are in phase at the polar side of the node. The zonal flow vacillation is primarily due to quasi-periodic variations of the wave driving by the interference of the stationary and traveling Wave 1. Similar periodic variations of the polar vortex were obtained in the numerical experiment with a spherical barotropic model in the circumstance that the stationary Wave 1 generated by the topographic forcing coexists with the eastward traveling Wave 2 due to barotropic instability of the forced mean zonal flow (Figs. 4.11 and 4.12). In this chapter, I use the same model to investigate the evolution of polar vortex in a wide range of parameters such as the amplitude of the topography and the prescribed zonal flow, in terms of dynamics of wave-wave interaction. I especially focus on how the mean zonal flow and the Wave 2 change those features from the case without topography of Wave 1 to the case in which the effect of Wave 1 is important.

Smith (1984) derived terms of wave-wave interaction in the potential enstrophy balance in order to investigate the dynamics of the anti-correlation between the amplitude of planetary Waves 1 and 2 in the Northern Hemisphere. Her studies (Smith 1984; Smith et al. 1985) using observational data and a subsequent study by Robinson (1985) with the use of three-dimensional β channel model suggest that wave-wave interactions could have a large effect on the interaction of waves with the mean flow. They examined the potential enstrophy budget averaged over a wide range in latitudes, however, we should investigate spatial structure as well as time variation of the contribution of the wave-wave interaction because the latitudinal structure is one of the important features of the wave-wave interaction as shown in Chapter 4.

Scinocca and Haynes (1998) considered the forcing of planetary wave variability in the stratosphere by synoptic-scale baroclinic eddies in the troposphere using a troposphere-stratosphere coupled primitive equation model without zonally asymmetric thermal and topographic forcings, and showed that the realistic stratospheric planetary wave amplitudes and variability can be forced through the wave-wave interaction of the baroclinic eddies. In their study, Transformed Fourier Decomposition (TFD) equations were introduced, which were used to combine the eddy vorticity forcing and the eddy temperature forcing of zonal wavenumber k into single expression form. They analyzed the spatial and temporal characteristics of the derived total effective eddy forcing for zonal wavenumber k, though the patterns are very complicated because of a highly nonlinear system in the troposphere.

Following their study, I examine the spatial and temporal characteristics of each term of the enstrophy equation including the nonlinear terms. Using the enstrophy equation,

we can evaluate the contribution of each term quantitatively. I consider the wave-wave interaction in more simple stratospheric case using a more simple model, the barotropic model, which will enable us to understand how the wave-wave interaction affects the change of a certain wavenumber (Wave 2 in this chapter) and which combinations of waves are dominant for the change of the enstrophy.

Single layer models have been used to study nonlinear dynamics of the winter stratosphere; such as planetary wave breaking (Juckes and McIntyre 1987, Thuburn and Lagneau 1999), the vacillation of the polar vortex with no topographic forcing (Ishioka and Yoden 1994, hereafter IY), the chaotic mixing process and transport barrier (Mizuta and Yoden 2001), and internal variation with topographic forcing (Rong and Waugh 2003). Rong and Waugh investigated the evolution of the polar vortex in a shallow water model with topography for a range of the topographic forcing amplitude. For small forcing amplitudes, there are only weak disturbances on the edge of the polar vortex and the vortex area remains constant. For large forcing amplitudes, the flow is highly nonlinear and there are cycles where the vortex breaks down and then reforms. As they were interested in the case for the large amplitude, they made analysis of the mass within potential vorticity contours, and showed that the vacillation for large forcing amplitude were primarily explained by the diabatic relaxations and hyper-diffusion. On the other hand, in the case that the flow is weakly nonlinear that I focus on in this paper, a barotropic model is sufficient to examine the nonlinear effect since there is no change of mass.

My objective is to examine the flow régimes sweeping the parameters of the topographic forcing and profile of prescribed jet, and to evaluate contribution of the nonlinear effect to the time change of the mean zonal flow and waves by the enstrophy diagnosis.

5.2 Model and Diagnosis

5.2.1 Model

I use the dynamical model of the two-dimensional flow on the earth with zonal-flow forcing, dissipation and surface topography, which is the same model as used in Chapter 4. The system is governed by a vorticity equation in the form

$$\frac{D}{Dt}\left(\zeta + f + \frac{hf}{H}\right) = -\alpha(\zeta - \overline{\zeta_0}) + \nu\left(\nabla^2 + \frac{2}{a^2}\right)(\zeta - \overline{\zeta_0}), \tag{5.1}$$

where $\zeta(\lambda, \phi, t) = \nabla^2\psi$ is the relative vorticity, $\psi(\lambda, \phi, t)$ the streamfunction, λ the longitude, ϕ the latitude, t the time, $f = 2\Omega\sin\phi$ the Coriolis parameter, Ω the angular speed of the earth's rotation, a the radius of the earth, h the height of the surface topography, and H the thickness of the fluid layer. The relaxation time α^{-1} of the Newtonian-type forcing is set to 10 days and artificial viscosity coefficient ν is fixed at a small constant (6.43×10^4 m^2 s^{-1}) to give the dissipation. The horizontal Laplacian operator ∇^2 and the

material derivative operator D/Dt are given by,

$$\nabla^2 = \left[\frac{1}{a^2\cos^2\phi}\frac{\partial^2}{\partial\lambda^2} + \frac{1}{a^2\cos\phi}\frac{\partial}{\partial\phi}\left(\cos\phi\frac{\partial}{\partial\phi}\right)\right], \tag{5.2}$$

$$\frac{D}{Dt} = \frac{\partial}{\partial t} + u\frac{1}{a\cos\phi}\frac{\partial}{\partial\lambda} + v\frac{1}{a}\frac{\partial}{\partial\phi}, \tag{5.3}$$

where the horizontal velocity is

$$(u, v) = \left(-\frac{1}{a}\frac{\partial\psi}{\partial\phi},\ \frac{1}{a\cos\phi}\frac{\partial\psi}{\partial\lambda}\right). \tag{5.4}$$

I use a spectral model with T85 truncation and the fourth-order Runge-Kutta method for time integration. The potential vorticity (hereafter PV), $q = \zeta + f + hf/H$, is conserved following fluid motion if the forcing and dissipation terms on the right side of Eq. (5.1) can be neglected.

The prescribed zonally symmetric vorticity $\bar{\zeta_0} = \nabla^2\bar{\psi}_0$ for the forcing is set to satisfy the necessary condition of barotropic instability (Hartmann 1983):

$$\overline{u_0} = \frac{1}{2}U\left(1 + \tanh\frac{\phi - \phi_0}{B}\right)\cos\phi, \tag{5.5}$$

where U is a measure of the intensity of the prescribed jet, B its width, and ϕ_0 its position. An Example of the profiles of $\overline{u_0}$ and $\overline{q_0}$ is shown in Fig. 4.10. All the conditions are same as IY and Mizuta and Yoden (2001) in the case of $h = 0$ and the régime diagram for this case in the three dimensional parameter space (U, B, and ϕ_0) is given in IY (their Fig. 1).

To introduce the effect of the stationary Wave 1, sinusoidal surface topography of zonal wavenumber 1 is assumed in the model SH:

$$h(\lambda, \phi) = \frac{1}{2}h_0(\sin 2\phi)^2\cos\lambda, \tag{5.6}$$

and no topography in the NH. I sweep the parameters B and $r = h_0/H$, with $U = 240$ m s^{-1} and ϕ_0 =55°, to investigate dynamical features depending on the parameters.

5.2.2 Diagnostics

The dynamical features of time dependent solutions are examined with the Fourier decomposed enstrophy equations, which can describes the effect of the wave-wave interaction explicitly. The fundamental concept is based on TFD equation. Equation (5.1) can be written schematically as

$$\frac{\partial\zeta}{\partial t} = \mathcal{C}(\bar{\psi}_0) + \mathcal{L}(\psi) + \mathcal{N}(\psi, \psi), \tag{5.7}$$

where $\mathcal{C}(\bar{\psi}_0)$ is a constant term, $\mathcal{L}(\ )$ an operator that is linear in ψ, and $\mathcal{N}(\ )$ a nonlinear operator that is quadratic in ψ, i.e. advection terms. Decomposing ψ into a zonal mean $\bar{\psi}$ and zonal wavenumber k components, $\psi = \bar{\psi} + \sum_k \psi_k$, the nonlinear term is described as

$$\mathcal{N}(\psi, \psi) = \mathcal{N}(\bar{\psi}, \bar{\psi}) + \sum_k \overline{\mathcal{N}(\psi_k, \psi_k)} + \mathcal{L}_{\mathcal{N}}(\bar{\psi}, \psi_k) + \sum_k \left\{\sum_l \sum_m \mathcal{N}(\psi_l, \psi_m)_k\right\},$$

where $\mathcal{L}_{\mathcal{N}}(\ )$ is linear in each of $\bar{\psi}$ and ψ_k. As $\mathcal{N}(\bar{\psi},\bar{\psi}) = 0$ in the governing equation, Eq. (5.7) results in

$$\frac{\partial}{\partial t}\left(\bar{\zeta} + \sum_k \zeta_k\right) = \mathcal{C}(\bar{\psi}_0) + \mathcal{L}(\bar{\psi}) + \sum_k \left\{ \mathcal{L}(\psi_k) + \mathcal{L}_{\mathcal{N}}(\bar{\psi},\psi_k) + \overline{\mathcal{N}(\psi_k,\psi_k)} + \sum_l \sum_m \mathcal{N}(\psi_l,\psi_m)_k \right\}. \tag{5.8}$$

Thus, the zonal mean and zonal wavenumber k components of Eq. (5.7) are expressed as

$$\frac{\partial \bar{\zeta}}{\partial t} = \mathcal{C}(\bar{\psi}_0) + \mathcal{L}(\overline{\psi}) + \sum_k \overline{\mathcal{N}(\psi_k,\psi_k)}, \tag{5.9}$$

$$\frac{\partial \zeta_k}{\partial t} = \mathcal{L}(\psi_k) + \mathcal{L}_{\mathcal{N}}(\overline{\psi},\psi_k) + \sum_l \sum_m \mathcal{N}(\psi_l,\psi_m)_k. \tag{5.10}$$

Scinocca and Haynes (1998) extracted equivalent of $\sum_l \sum_m \mathcal{N}(\psi_l,\psi_m)_k$ for $k = 1$ and $k = 2$ in the primitive equations at each time step, and imposed the full or part of $\mathcal{N}(\psi_l,\psi_m)_k$ as a prescribed forcing in the linearized model to investigate important component (thermal or vorticity forcing), frequency, and pressure level for the generation of planetary waves. In this study, I divide streamfunction and vorticity fields into the stationary ($\langle\ \rangle$) and transient components (*) and derive the enstrophy equation for the transient component. Enstrophy is a useful diagnostic quantity because it is a positive measure of the strength of wave disturbance. Substituting the stationary and transient components into Eqs. (5.9) and (5.10) and subtracting the time averages, we obtain

$$\frac{\partial \bar{\zeta}^*}{\partial t} = \mathcal{C}(\bar{\psi}_0) + \mathcal{L}(\bar{\psi}^*) + \sum_k \overline{\mathcal{N}\left(\psi_k,\ \psi_k\right)^*}, \tag{5.11}$$

$$\frac{\partial \zeta_k^*}{\partial t} = \mathcal{L}(\psi_k^*) + \mathcal{L}_{\mathcal{N}}\left(\bar{\psi},\ \psi_k\right)^* + \sum_l \sum_m \mathcal{N}\left(\psi_l,\psi_m\right)_k^*, \tag{5.12}$$

where each term can be broken down into

$$\mathcal{N}\left(\psi_k,\ \psi_k\right)^* = \mathcal{N}\left(\langle\psi_k\rangle, \psi_k^*\right) + \mathcal{N}\left(\psi_k^*, \psi_k^*\right)^*, \tag{5.13}$$

$$\mathcal{L}_{\mathcal{N}}\left(\bar{\psi},\ \psi_k\right)^* = \mathcal{L}_{\mathcal{N}}\left(\langle\bar{\psi}\rangle, \psi_k^*\right) + \mathcal{L}_{\mathcal{N}}\left(\bar{\psi}^*, \langle\psi_k\rangle\right) + \mathcal{L}_{\mathcal{N}}\left(\bar{\psi}^*, \psi_k^*\right)^*, \tag{5.14}$$

$$\mathcal{N}\left(\bar{\psi}_l,\ \psi_m\right)_k^* = \mathcal{N}\left(\langle\bar{\psi}_l\rangle, \psi_m^*\right) + \mathcal{N}\left(\psi_l^*,\ \psi_m^*\right)^*. \tag{5.15}$$

Multiplying Eqs. (5.11) by $\bar{\zeta}^*$ and (5.12) by ζ_k^*, respectively, and taking a zonal average for the equation as to the zonal wavenumber k, the zonal mean enstrophy for zonal mean and wavenumber k components can be obtained as follows:

$$\frac{\partial}{\partial t}\left(\frac{1}{2}\bar{\zeta}^{*2}\right) = \bar{\zeta}^*\mathcal{L}(\bar{\psi}^*) + \sum_k \bar{\zeta}^*\overline{\mathcal{N}\left(\psi_k,\ \psi_k\right)^*}, \tag{5.16}$$

$$\frac{\partial}{\partial t}\left(\frac{1}{2}\overline{\zeta_k^{*2}}\right) = \overline{\zeta_k^*\mathcal{L}(\psi_k^*)} + \overline{\zeta_k^*\mathcal{L}_{\mathcal{N}}\left(\bar{\psi},\ \psi_k\right)^*} + \sum_l \sum_m \overline{\zeta_k^*\mathcal{N}\left(\psi_l,\psi_m\right)_k^*}. \tag{5.17}$$

Table 5.1: Régime diagram for two external parameters B and r. Symbol S refers to a steady-wave solution, V and V_2 a vacillation, P a periodic solution, I a irregular solution, Sta a stationary-wave solution, and N a no-wave solution.

B	3.0	3.5	**4.0**	4.5	5.0	5.5	6.0	6.5	7.0	7.5	8.0	9.0	10	11	12	14	16	18
r =0	V	V	**V**	V	V	V	S	S	S	S	S	S	S	S	N	N	N	N
0.02	V_2	V_2	**P**	P	P	P	P	P	P	P	P	Sta	Sta	Sta	Sta	Sta	Sta	Sta
0.04	P	P	**P**	P	P	P	P	P	P	P	P	Sta	Sta	Sta	Sta	Sta	Sta	Sta
0.06	P	P	**P**	P	P	P	P	P	P	P	P	Sta	Sta	Sta	Sta	Sta	Sta	Sta
0.08	I	I	**I**	P	P	P	P	P	P	P	P	Sta	Sta	Sta	Sta	Sta	Sta	Sta
0.10	I	I	**I**	I	I	P	P	P	P	P	P	Sta	Sta	Sta	Sta	Sta	Sta	Sta

The first terms on the right hand side in Eqs. (5.16) and (5.17) are concerned with the radiative dumping and dissipation. The second term in Eq. (5.16) is the term concerned with wave-mean flow interaction. Note that $\overline{\mathcal{N}(\psi_k, \psi_k)}$ is the divergence of the Eliassen Palm flux. The second term in Eq. (5.17) is the rate at which the wave extracts enstrophy from the zonal flow, and the final term is the rate at which the wave gains enstrophy from wave-wave interactions. I investigate latitudinal and temporal structure of each term of the enstrophy equation for the mean zonal flow and that for the Wave 2 using the Eqs. (5.16) and (5.17), respectively.

5.3 Flow régime

Table 5.1 is a régime diagram for two external parameters of the width of the prescribed zonal flow B and the external topographic height r, in wide ranges of $3 \leq B \leq 18$ and $0 \leq r \leq 0.1$. In case of $r = 0$ (IY), the three kinds of solution are obtained. For the narrower prescribed jet to satisfy the barotropic instability condition, the steady-wave solution (S) ($6 \leq r \leq 11$) and the vacillation (V) ($3 \leq r \leq 5.5$) are obtained. For the steady-wave solution, Wave 2 propagates eastward without changing its amplitude, while for the vacillation Wave 2 changes its amplitude periodically. When the forcing of the jet is wide enough to satisfy the barotropic stability($r \geq 12$), no wave is generated (N).

As regards $r \neq 0$, four kinds of solution are obtained; vacillation (V_2), periodic solution (P), irregular solution (I), and stationary-wave solution (Sta). In periodic solution, both Wave 1 and Wave 2 travel eastward periodically, and the zonal mean flow also fluctuates at the same period. The flow changes purely periodically over a wide range of r with the prescribed zonal flow satisfying the barotropic instability condition. For small B and r ($B \leq 3.5$ and $r = 0.02$), the vacillating solution V_2 is obtained, for which the features of the mean flow and wave are similar to those for the vacillation at $r = 0$ (V) as will hereinafter be described in detail. For large topographic forcing with small B ($B \leq 5.5$), the flow

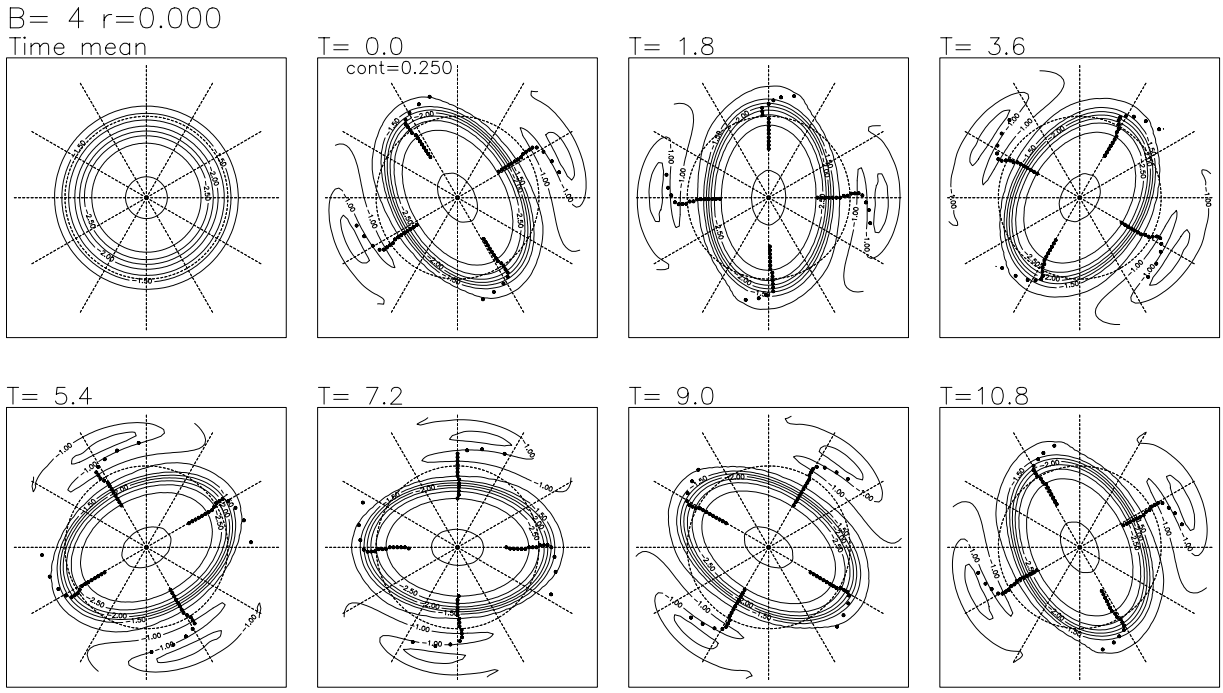

Figure 5.1: Time mean and time evolution of the potential vorticity for $\phi \geq 40°$S for the vacillation, $B = 4$ and $r = 0$. The value is scaled by Ω and the contour interval is 0.25. The unit of time is a day. Dotted lines indicate the location of the ridge or trough between 72.1°S and 51.1°S.

becomes irregular. For $9 \leq B \leq 18$ in which the forcing satisfies the barotropically stable condition ($13 \leq B$), only the stationary Wave 1 due to the topographic effect is observed.

Figures 5.1, 5.2 and 5.3 show examples of the time mean and time evolution of PV for the vacillation V ($B = 4$ and $r = 0$), for the periodic solution P ($B = 4$ and $r = 0.04$), and for the irregular one I ($B = 4$ and $r = 0.09$), respectively. For the vacillation, the time mean polar vortex is exact circular (Fig. 5.1). The elongated polar vortex rotates eastward with an angular phase velocity of about $\pi/10.8$ per day. It changes shape, stretching ($t = 5.4 \rightarrow 10.8$) and shrinking ($t = 0.0 \rightarrow 3.6$) in the vacillation cycle about 9.2 day. As for the periodic solution (Fig. 5.2), the time mean polar vortex shows an off-the-pole structure with roughly circular form, reflecting the dominance of the stationary Wave 1 forced by the topography. The elongated vortex rotates eastward with an angular phase velocity of about $\pi/9.6$ per day, changing its shape at the same period. The ridge and trough lines of the Wave 2 (dots) show the tilted phase variation: The phase on the inner side of the vortex edge does not tilt at $t = 7.2$, whereas it tilts from southeast to northwest at $t = 1.8$ and 3.6. Such a tilting structure is not observed for the vacillation (Fig. 5.1). For the irregular solution, the polar vortex is more disturbed and filamental structures are observed at the edge of the polar vortex (Fig. 5.3). However, some fundamental features observed for the periodic solutions are still found, such as the off-the-pole structure and the eastward rotation.

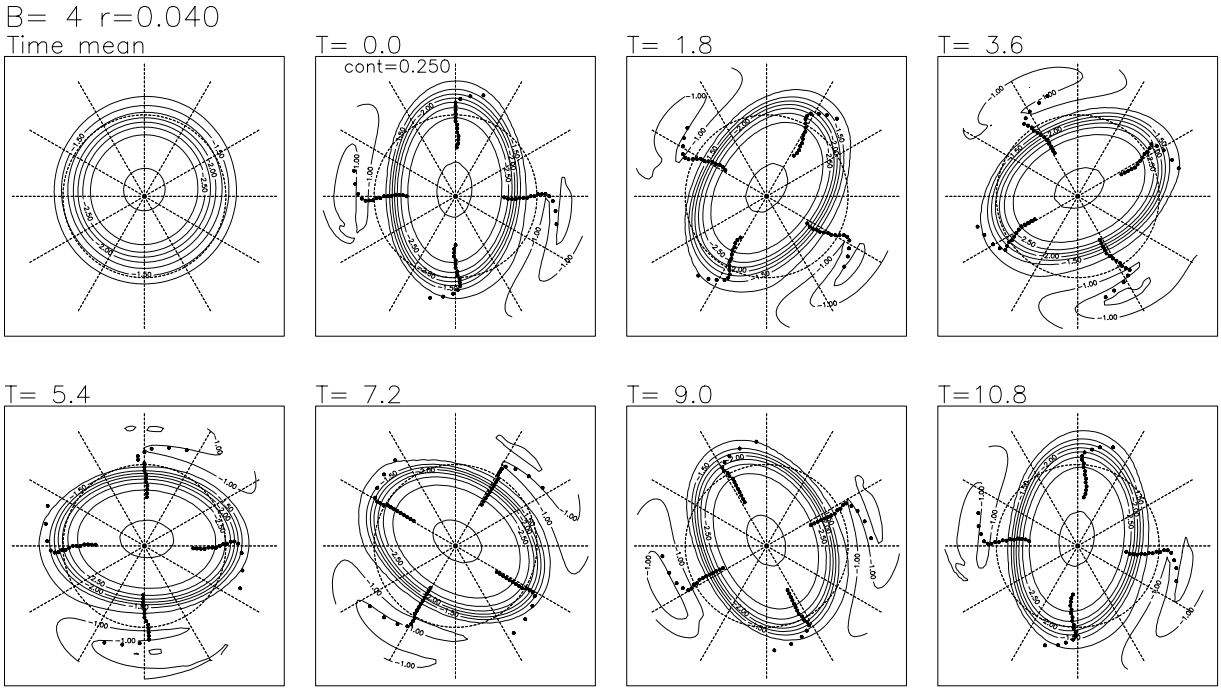

Figure 5.2: Same as Fig. 5.1, but for the periodic solution, $B = 4$ and $r = 0.04$.

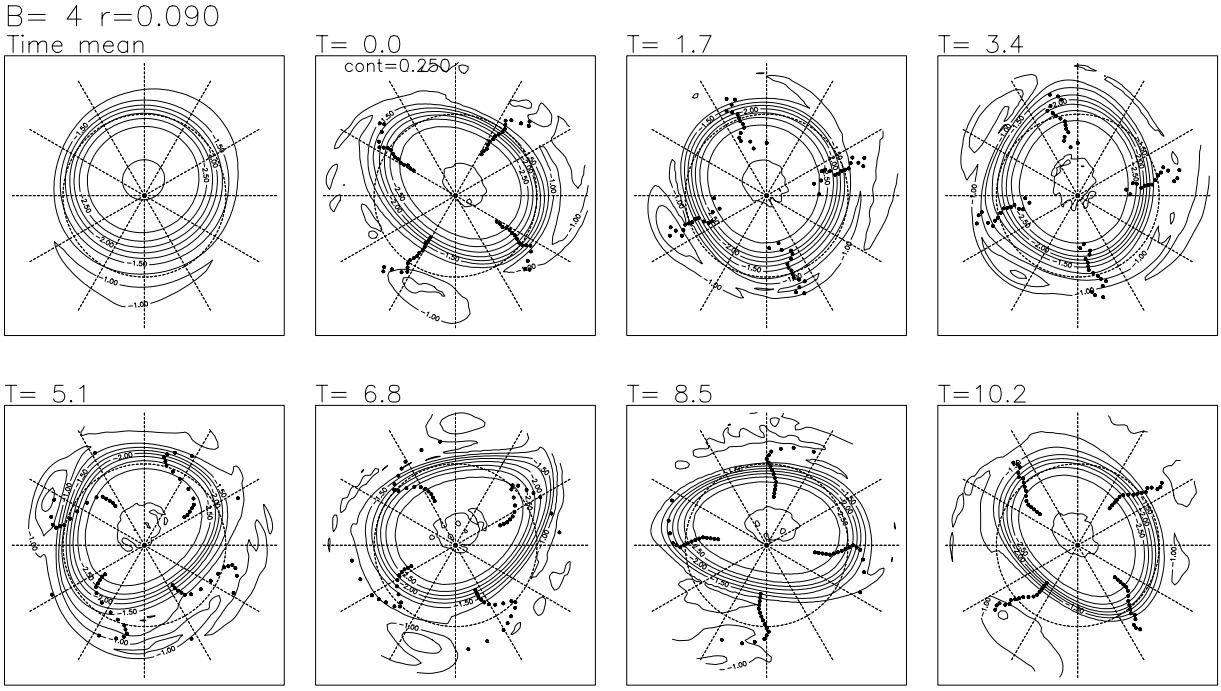

Figure 5.3: Same as Fig. 5.1, but for the irregular solution, $B = 4$ and $r = 0.09$.

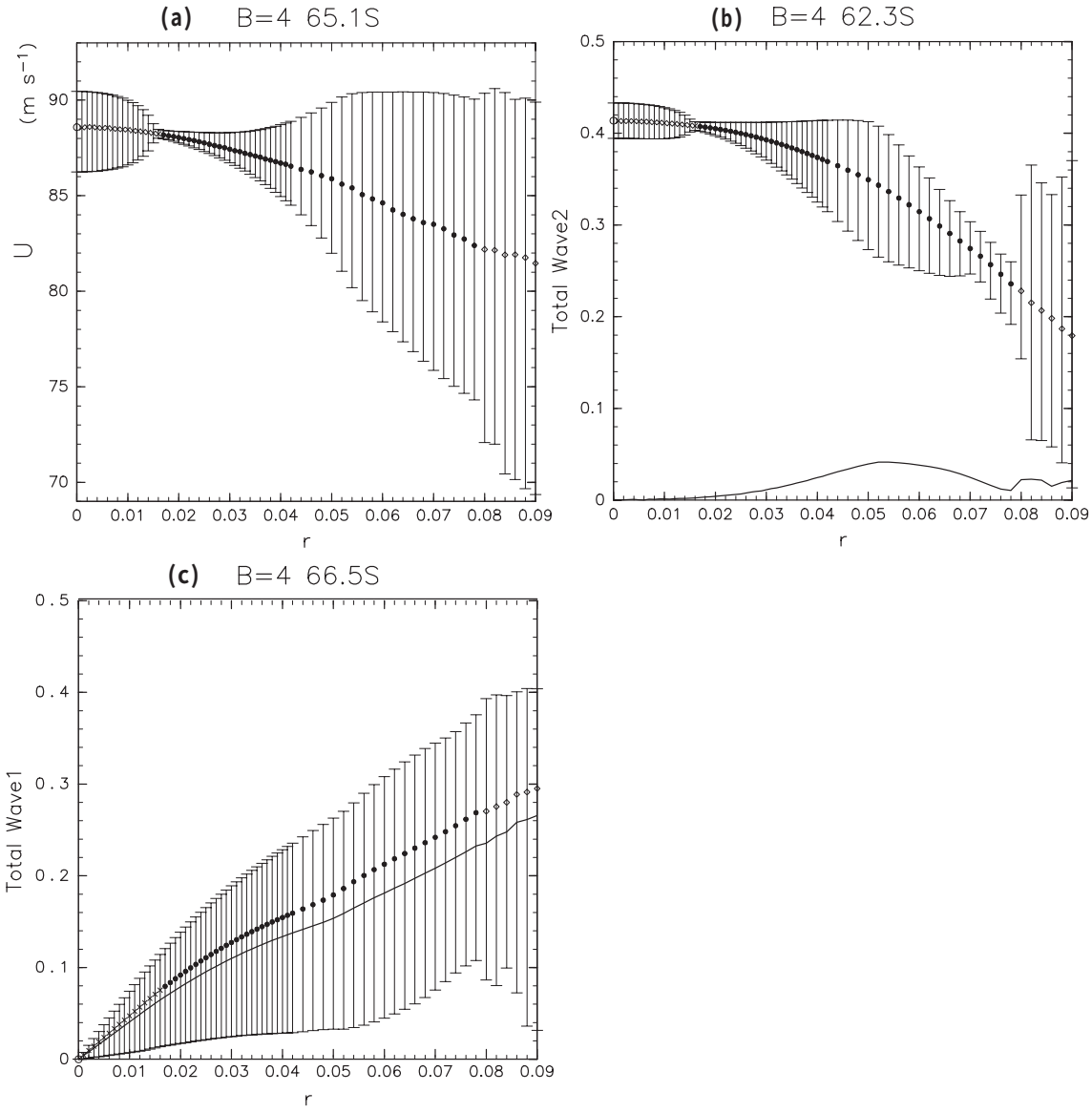

Figure 5.4: Time mean zonal mean wind at 65.1°S (a), amplitude of total Wave2 at 62.3°S (b) and total Wave 1 at 66.5° (c) plotted for the external parameter r with $B = 4$ with the variable range shown by the vertical bar. The vacillation for $r = 0$ (V) is indicated by ($\circ$), vacillation for small r (V_2) by ($\times$), periodic solution by ($\bullet$), and the irregular solution by ($\diamond$). The solid lines in (b) and (c) indicate the amplitude of stationary Wave 2 and 1, respectively. The amplitudes are scaled by Ω.

Here I now examine the régime transition with r in more detail for $B = 4$ as a representative, for which various kinds of solutions are obtained. I sweep the parameter r every 0.001 for $0 \leq r \leq 0.042$ and 0.002 for $0.044 \leq r \leq 0.09$. Figure 5.4 shows the dependence of some important quantities on the parameter r: the time mean zonal mean zonal flow at 65.1°S (a), and the mean amplitude of the total Wave 2 at 62.3°S (b) and the total Wave 1 at 66.5S (c), together with those variation ranges (vertical bar). I select the latitude at which each quantity is maximum for wide range of r. The average period is changed for each r according as the period of the phase variation of traveling Wave 2.

For $0 < r \leq 0.016$, the vacillating solution (V_2) is obtained as observed for $B \leq 3.5$ with $r = 0.02$ (expressed by 'X' in Fig. 5.4). The flow changes purely periodically (solid circle) for $0.017 \leq r \leq 0.078$, which behaves irregularly for $r \geq 0.08$ (diamond). The time mean zonal mean zonal flow becomes weak gradually with the increase of r for all the régimes. Variable range of zonal mean zonal flow changes its features with the régime transition: For the vacillation, it gets narrow as r increases and has its minimum at $r = 0.016$, then broadens gradually for $r \geq 0.017$. It becomes large in a discontinuous manner at $r = 0.8$.

As for the Wave 2 (Fig. 5.4b), the amplitude of total Wave 2 decreases with r. The variable range changes at $r = 0.017$: It becomes narrow with r for the vacillation and has its minimum at $r = 0.016$, while it increases for $0.17 \leq r \leq 0.052$ in which the maximum amplitude is almost constant. For $0.052 \leq r \leq 0.078$, the variable range decreases with r accompanying with the decrease of the maximum amplitude. It changes in a discontinuous manner at $r = 0.08$, though the time mean amplitude gradually decreases continuously with r for the irregular solution. The change of the amplitude of the stationary Wave 2 (solid line) is roughly zero for the vacillation ($0 \leq r \leq 0.016$). For the periodic solution, it increases with the peak at $r = 0.052$ and then decreases with r.

Concerning to the Wave 1 (Fig. 5.4c), the variable range of the amplitude of total wave, as well as mean value, increases with the r for $0 \leq r \leq 0.078$ and no outstanding change is found accompanying the transition from the vacillation to the periodic solution.The variable range changes in a discontinuous manner at $r = 0.08$, though the time mean amplitude gradually increases continuously.

Figure 5.5 shows the time variation of the zonal mean zonal flow (top), and polar diagrams of Wave 2 at ϕ_{TW2} (middle) and Wave 1 at ϕ_{TW1P} (bottom) of 12 experiments for $0 \leq r \leq 0.088$, where the definitions of ϕ_{TW2} and ϕ_{TW1P} are same as Chapter 4; the transient Wave 2 and Wave 1 have its maximum at ϕ_{TW2} and ϕ_{TW1P}, respectively. For the vacillation ($0 \leq r \leq 0.016$), the mean zonal flow fluctuates almost sinusoidally and the polar diagrams of Wave 1 and Wave 2 show torus structure, which is the characteristics for the vacillation; The angular phase velocity of the eastward propagation of Wave 2 is different from the vacillation cycle, as recognized by the timings when the mean zonal flow has its local maximum (minimum), indicated by open circle (cross mark). For $0 < r \leq 0.016$, the Wave 1 also rotates eastward with the same angular frequency as Wave 2.

For the periodic solution ($0.016 \leq r \leq 0.078$), the mean zonal wind fluctuates periodically and the phase of the Waves 2 is always same at the time when the zonal wind has its maximum or minimum, indicating that the frequency of the eastward propagation of Wave 2 is same as that of the fluctuation of the mean zonal flow. The transient Wave 1 also propagates eastward with the same frequency. The phase of traveling Wave 1 when the zonal mean flow is minimum (cross mark for Wave 1) is almost same as that of traveling Wave 2 when the zonal flow is maximum (circle for Wave2). For $0.24 \leq r \leq 0.56$, the traveling Wave 2 at the timing when the mean zonal flow is maximum, is not in opposite

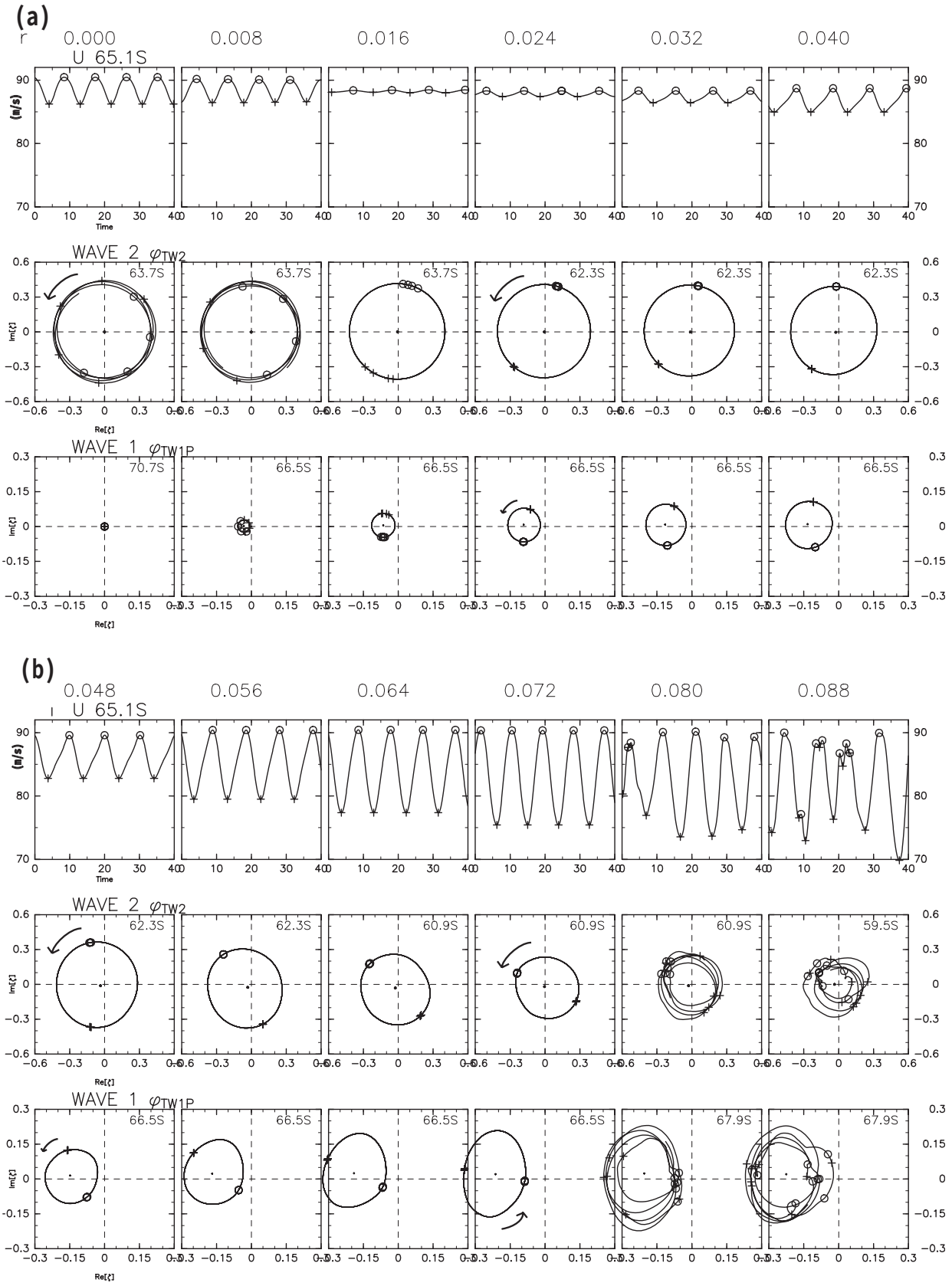

Figure 5.5: Time change of zonal mean zonal flow at 65.1°S (top), and polar diagrams for Wave 2 at ϕ_{TW2} (middle) and Wave 1 at ϕ_{TW1P} (bottom) for $B = 4$ for a range between $r = 0$ and $r = 0.04$ (a) and between $r = 0.048$ and $r = 0.088$ (b) every 0.004. The marks (∘) and (+) indicate the phase at the time when the mean zonal wind reaches its local maximum and minimum, respectively.

phase to the counterpart at the timing when the zonal mean flow is minimum. In synchronization with this, the mean zonal flow changes in saw-tooth waveform. As r increase, the phase difference of traveling Waves 2 between the these two timings approaches to π. For $r = 0.072$, the periodicity is similar to almost those for $B = 6$ and $r = 0.08$ shown in previous chapter (Fig. 4.11): The traveling Wave 1 is in phase with the stationary Wave 1 and traveling Wave 2 at the timing when the mean zonal flow is minimum.

For the irregular solution ($r = 0.080$ and 0.088), the mean zonal flow fluctuates rather periodically. The clusters of the marks in the polar diagrams indicate that both the traveling Wave 1 and 2 also rotate eastward with a similar frequency as the variation in mean zonal flow.

5.4 Diagnostics based on the enstrophy equations

Since the different characteristics are clearly seen between the vacillation and the periodic solution as to the variable range of zonal flow and that of Wave 2 (Fig. 5.4a and b), the enstrophy diagnosis of the zonal flow and that of the transient Wave 2 are made for five cases out of the 12 cases shown in Fig. 5.5, $r = 0$, 0.008, 0.024, 0.032 and 0.040, as representatives, in order to examine how the dynamics change with the régime transition. I focus on the effect large-scale waves, that is, dominant scale in this model.

5.4.1 Zonal flow

The Eq. (5.16) can be rewritten as:

$$\frac{\partial}{\partial t}\left(\frac{1}{2}\bar{\zeta}^{*2}\right) = \bar{\zeta}^{*}\mathcal{L}(\bar{\psi}^{*}) + \underbrace{\bar{\zeta}^{*}\overline{\mathcal{N}\left(\psi_1,\, \psi_1\right)^{*}}}_{\text{Term A}} + \underbrace{\bar{\zeta}^{*}\overline{\mathcal{N}\left(\psi_2,\, \psi_2\right)^{*}}}_{\text{Term B}} + \sum_{k=3}^{85} \bar{\zeta}^{*}\overline{\mathcal{N}\left(\psi_k,\, \psi_k\right)^{*}}, \qquad (5.18)$$

Figure 5.6 shows the enstrophy tendency (top) and the contributions of Wave 1 (Term A) (third), of Wave 2 (Term B) (bottom) and the sum of the two terms (Term A +Term B) (second) in Eq. (5.18) for the five experiments. The enstrophy tendency changes its sign periodically for all the cases: Corresponding to the change of the jet intensity as shown in Fig. 5.5, the enstrophy of the zonal mean component (i.e. the square of the gradient of the zonal mean wind) has the local minimum twice a period. For the periodic solution, the tilted structures propagating poleward with time are found at high-latitudes.

The pattern of the second panels can roughly reproduce the enstrophy tendency, indicating that the variations in the zonal flow are explained by the effect of the divergence of EP flux of Wave 1 (Term A) and Wave 2 (Term B) for the both régimes. For the vacillation ($r = 0$ and 0.008), Term A is extremely small compared to Term B, thus, the enstrophy of the mean zonal flow is mainly exchanged by that of the Wave 2. On the other hand, for the periodic solution ($r = 0.024$, 0.032, and 0.040), the contribution of Wave 1 (Term

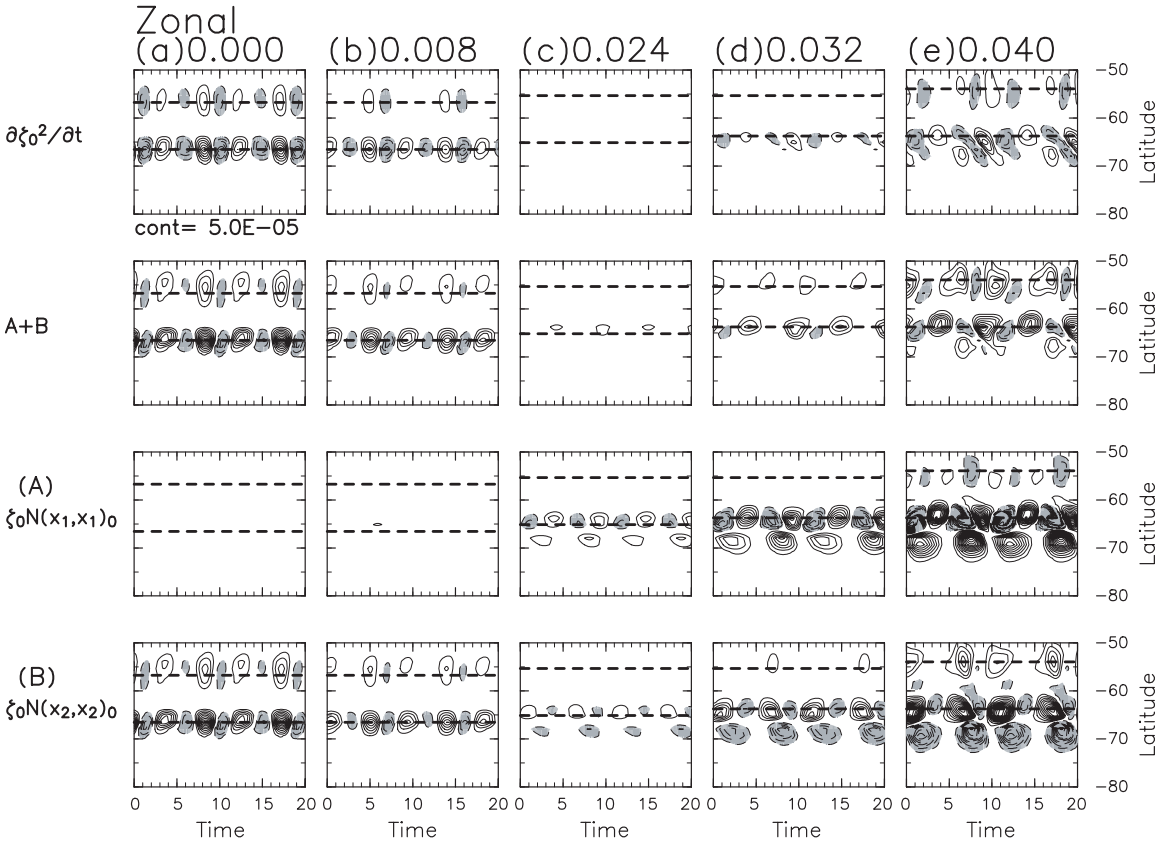

Figure 5.6: Latitude-time section of each term of enstrophy equation of the mean zonal flow for $r = 0$ (a), 0.008 (b), 0.024 (c), 0.032 (d), and 0.040 (e); the enstrophy tendency (top panel), Term A (third panel) and Term B (the bottom panels). The sum of Terms A and B is shown in the second panel. The enstrophy is scaled by Ω^2 and the time is scaled by *day*. The contour interval is $5.0 \times 10^{-4}[\Omega^2 \mathrm{day}^{-1}]$.

A) is comparable to that of Wave 2 (Term B). They largely cancel each other out and the pattern of the sum of Terms A and B represents the larger contribution of Wave 1.

Mean absolute value of these terms between 63.7°S and 66.5°S is plotted against to r in Fig. 5.7. The enstrophy tendency for the mean zonal flow can be expressed well by the wave forcing for Waves 1 and 2 for $0 \leq r < 0.07$. The absolute value of Term B which decreases with r is much larger than that of Term A (cross mark) for the vacillation régime, indicating that the vacillation of zonal flow is mainly explained by the effect of the Wave 2. For the periodic solution, Term A is slightly larger than Term B and increases for a wide parameter range ($0.17 \leq r \leq 0.054$). In addition, the sum of these terms (solid circles) is much smaller compared to each term. Thus, for this parameter range, Terms A and B largely cancel each other and Term B is the leading term in the enstrophy equation of the mean zonal flow as seen at $r = 0.024$, 0.032, and 0.040 (Fig. 5.6). For $r \geq 0.07$, difference between the enstrophy tendency and the sum of the Terms A and B become large with r, reflecting that the contribution from other wavenumber components becomes important.

In order to examine the contributions of stationary and transient waves, Terms A and B are broken down into the terms concerning the stationary and transient components (“

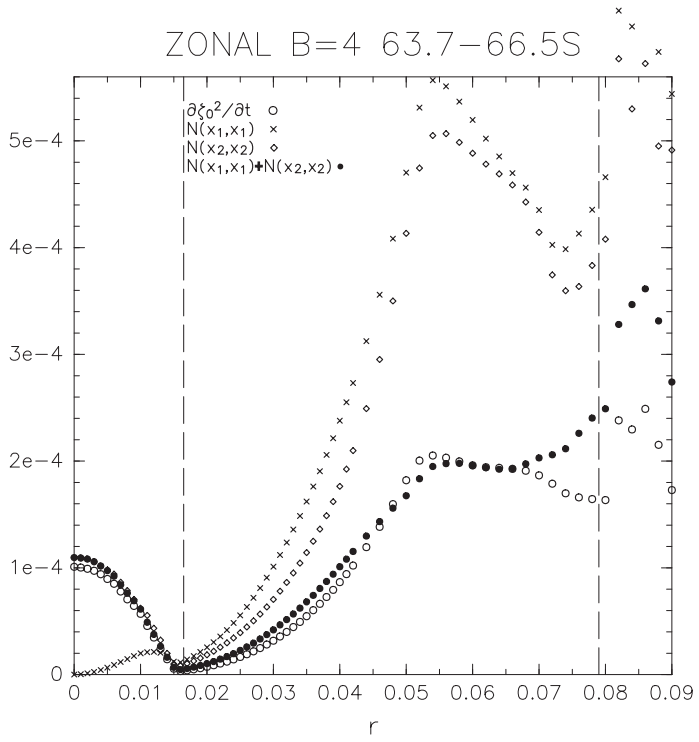

Figure 5.7: Time mean absolute value of each term in Eq. (5.18) between 63.7°S and 66.5°S plotted against the external parameter r; tendency of the enstrophy for the zonal flow (open circle), Term A $\bar{\zeta}^* \overline{\mathcal{N}\left(\psi_1,\, \psi_1\right)^*}$ (cross), Term B $\bar{\zeta}^* \overline{\mathcal{N}\left(\psi_2,\, \psi_2\right)^*}$ (diamond), and Term A + Term B (solid circle).

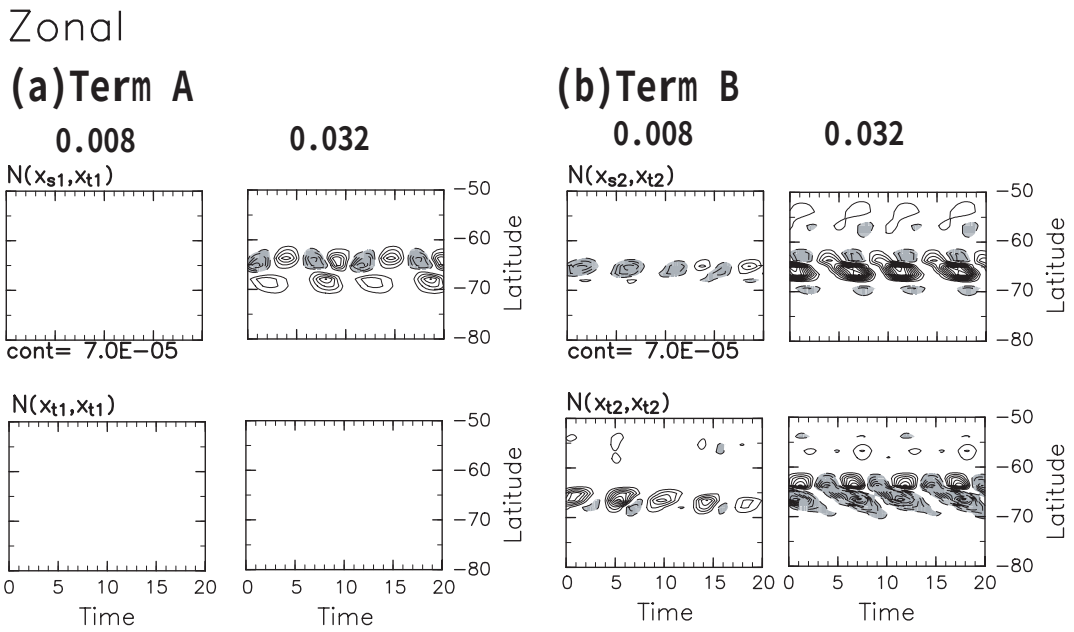

Figure 5.8: Latitude-time sections of the components of Term A (a) and Term B (b) for $r = 0.008$ (left) and $r = 0.032$ (right); terms concerning the stationary and transient components ($\bar{\zeta}^* \overline{\mathcal{N}\left(\langle\psi_k\rangle\,,\, \psi_k^*\right)}$) are shown in top panels and those concerning only the transient component ($\bar{\zeta}^* \overline{\mathcal{N}\left(\psi_k^*, \psi_k^*\right)^*}$) in bottom panels. The enstrophy is scaled by Ω^2 and the time is scaled by *day*. The contour interval is $7.0 \times 10^{-5} [\Omega^2 \mathrm{day}^{-1}]$.

cross term"); $\bar{\zeta}^*\overline{\mathcal{N}\left(\langle\psi_k\rangle\,,\psi_k^*\right)}$, and that concerning only the transient components ("spectral term"); $\bar{\zeta}^*\overline{\mathcal{N}\left(\psi_k^*,\psi_k^*\right)^*}$, according Eq. (5.13). The latitude-time sections of these terms are shown in Fig. 5.8 for the vacillation ($r = 0.008$) and the periodic solution ($r = 0.032$). As for the contribution of Wave 1 (Fig 5.8a), both the cross term and the spectral term of are small for the vacillation (left). On the other hand, the cross term is dominant for the periodic solution (right). Thus, the enstrophy tendency of zonal flow is controlled by the interference between the stationary Wave 1 and transient Wave 1 for the periodic solution.

As regards Wave 2, the spectral term of the traveling Wave 2 is dominant for both of the régime (Fig 5.8b), which is largely canceled out by the cross term of the stationary and traveling components.

5.4.2 Wave 2

I represent the enstrophy equation (Eq. (5.17)) for Wave 2 as follows:

$$\begin{aligned}\frac{\partial}{\partial t}\left(\frac{1}{2}\overline{\zeta_2^*}^2\right) =& \underbrace{\overline{\zeta_2^*\mathcal{L}(\psi_2^*)} + \overline{\zeta_2^*\mathcal{L}_{\mathcal{N}}\left(\bar{\psi},\,\psi_2\right)^*}}_{\text{Term C}} \\ &+ \underbrace{\overline{\zeta_2^*\mathcal{N}\left(\psi_2,\psi_4\right)_2^*}}_{\text{Term D}} \\ &\underbrace{+\overline{\zeta_2^*\mathcal{N}\left(\psi_1,\psi_1\right)_2^*} + \overline{\zeta_2^*\mathcal{N}\left(\psi_1,\psi_3\right)_2^*}}_{\text{Term E}} \\ &+ \sum_{l=3}^{85}\sum_{m=3}^{85}\overline{\zeta_2^*\mathcal{N}\left(\psi_l,\psi_m\right)_2^*},\end{aligned} \tag{5.19}$$

where Term C is the contribution of the linear forcing, Term D the contribution of wave-wave interaction between the Waves 2 and 4, and Term E the contribution of wave-wave interactions between the Waves 1 and 1 and between the Waves 1 and 3. Figure 5.9 shows latitude-time sections of the enstrophy tendency for transient Wave 2 (top) and Term C (third), Term D (fourth), Term E (bottom) and the sum of the three terms (Term C +Term D+Term E) (second) for the same five cases as same in Fig. 5.6. The enstrophy tendency changes its sign periodically in large area latitudinally with a maximum around 65°S for the vacillations ($r = 0$ and $r = 0.008$). For the periodic solutions ($r = 0.024$, 0.032, and 0.040), the enstrophy tendency also changes its sign periodically, though its structure is quite different from that for the vacillation: The positive enstrophy tendency propagates poleward with time.

For vacillation, the contribution of wave-wave interaction by the odd wavenumbers (Term E) can be neglected. The contribution of wave-wave interaction between the Wave 2 and Wave 4 (Term D) largely cancels out that of linear term (Term C) and the sum of the Terms C and D can roughly reproduce the tendency of the enstrophy. Thus, the enstrophy

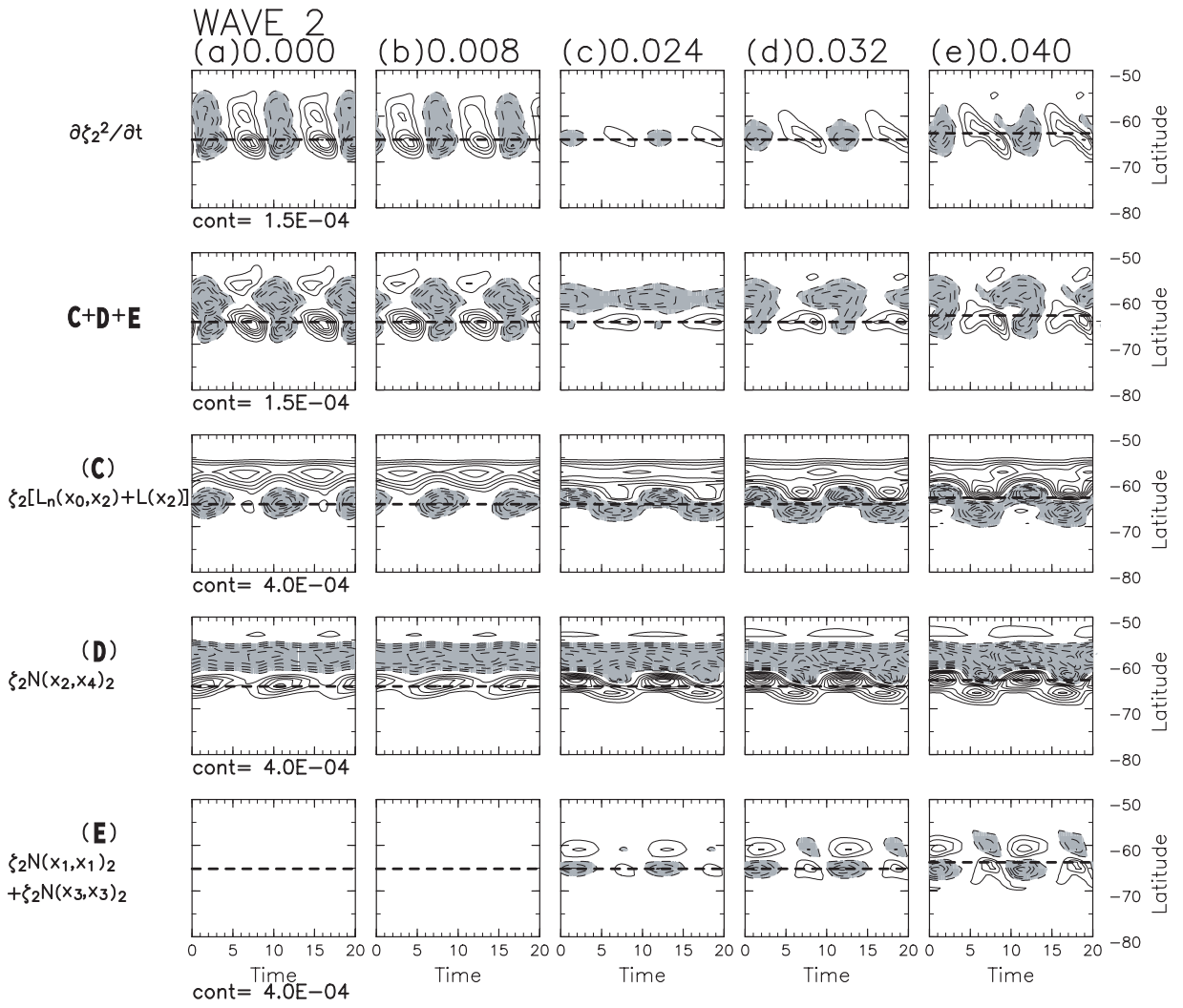

Figure 5.9: Latitude-time section of each term of the enstrophy equation for transient Wave 2 for $r = 0$ (a), 0.008 (b), 0.024 (c), 0.032 (d), and 0.040 (e); the enstrophy tendency for the transient Wave2 (top), Term C (third), D (fourth), and E (bottom). The sum of Terms C ,D and E is shown in the second panel. The enstrophy is scaled by Ω^2 and the time is scaled by *day*. The contour intervals are $1.5 \times 10^{-4}[\Omega^2 \mathrm{day}^{-1}]$ for top and second panels and $1.5 \times 10^{-4}[\Omega^2 \mathrm{day}^{-1}]$ for the three bottom panels.

tendency of Wave 2 is explained by the radiative dumping and the gain from the wave-wave interaction between the Wave 2 and 4.

As for the periodic solution, Term C largely cancels out Term D, though the spatial patterns of these terms show some different aspects from those for the vacillation: For the periodic solutions, both Terms C and D have the dipole structures on the pole side of 55°S with the node around 65°S, of which signs are opposite between the two terms, while such dipole structures are not seen for the vacillation. Term C (Term D) is always positive (negative) between 55°S and 60°S for all the cases. For the periodic solution, Term E shows a dipole pattern with a node around 62.5°S and changes its sign periodically. As the result of the large cancellation between Terms C and D, the pattern of the sum of Terms C, D and E (second) resembles that of Term E around 65°S. Since the pattern of the enstrophy

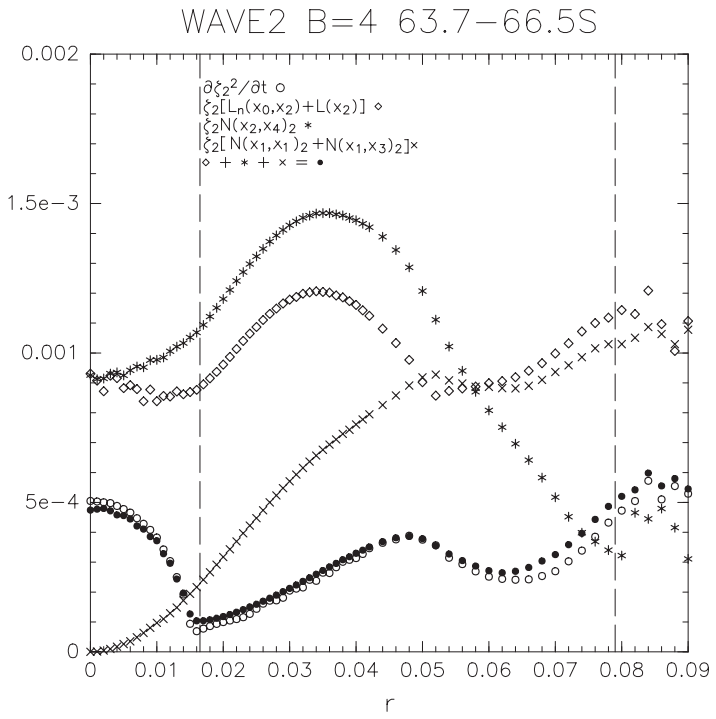

Figure 5.10: Time mean absolute value of each term in Eq. (5.19) between 63.7°S and 66.5°S plotted against the external parameter r; tendency of the enstrophy for the transient Wave 2 (open circle), Terms C $\overline{\zeta_2^* \mathcal{L}(\psi_2^*)} + \overline{\zeta_2^* \mathcal{L}_{\mathcal{N}}\left(\bar{\psi}, \psi_2\right)^*}$ (diamond), Term D $\overline{\zeta_2^* \mathcal{N}\left(\psi_2, \psi_4\right)_2^*}$ (asterisk) , Term E $\overline{\zeta_2^* \mathcal{N}\left(\psi_1, \psi_1\right)_2^*} + \overline{\zeta_2^* \mathcal{N}\left(\psi_1, \psi_3\right)_2^*}$ ("X" mark), and Term C + Term D + Term E (solid circle).

tendency can be roughly explained by the pattern of Terms C, D, and E around 65°S, the wave-wave interactions between the odd wavenumbers are also important for the time change of Wave 2 there.

Figure 5.10 shows the time mean absolute value of these quantities between 63.7°S and 66.5°S plotted against r. The value of Term E monotonically increases with r for $0 < r \leq 0.052$. The difference between Terms C and D becomes large as the increase of r for the vacillation ($0 \leq r \leq 0.16$), suggesting that the contribution of Term E becomes important with the increase of r. For the periodic solution, the change of Term D for $0.17 \leq r \leq 0.052$ shows very similar curve to that in Term C. As the results of the large cancellation between the two terms, the sum of the Terms C, D, and E is quite small compared to Term C and Term D, and increases monotonically in similar way with Term E. These results suggest that Term E is important for the change of the enstrophy of the transient Wave 2 for the periodic solution as seen in Fig. 5.9 for $r = 0.024$, 0.032 and 0.040. For $r > 0.058$, Term E dominates over Term D.

Figure. 5.11 shows the latitude-time section of the dominant terms composing Terms C, D, and E according Eqs. (5.14) and (5.15) (see Appendix Eq. (A.11)) for the vacillation ($r = 0.008$) and for the periodic solution ($r = 0.032$). The term D can be explained well only by the effect of the wave-wave interaction between transient Waves 2 and 4 (Fig. 5.11b) for both experiments. As for Term E, all of the terms can be negligible for the vacillation

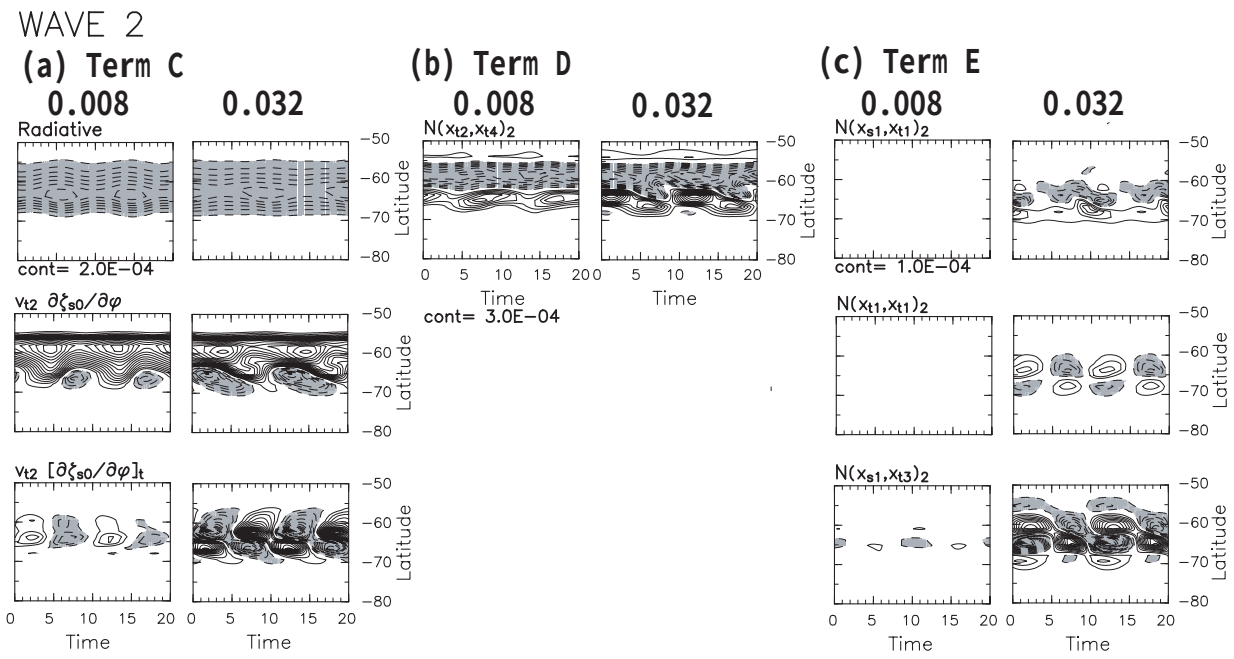

Figure 5.11: Latitude-time sections of the dominant components of Term C (a), Term D (b), and Term E (c) for $r = 0.008$ (left) and $r = 0.032$ (right): $:-\alpha\bar{\zeta_2^*}$ (top), $\overline{-\zeta_2^* v_2^* \frac{\partial\langle\bar{\zeta}\rangle}{a\partial\phi}}$ (middle), and $\overline{-\zeta_2^* \left(v_2^* \frac{\partial\bar{\zeta}^*}{a\partial\phi}\right)^*}$ (bottom) for Term C, $\overline{\zeta_2^* \mathcal{N}\left(\psi_2^*, \psi_4^*\right)_2^*}$ for Term D, and $\overline{\zeta_2^* \mathcal{N}\left(\bar{\psi}_1, \psi_3^*\right)_2}$ (top) , $\overline{\zeta_2^* \mathcal{N}\left(\bar{\psi}_1, \psi_1^*\right)_2}$ (middle) and $\overline{\zeta_2^* \mathcal{N}\left(\bar{\psi_1}^*, \psi_1^*\right)_2^*}$ (bottom) for Term E. The enstrophy is scaled by Ω^2 and the time is scaled by *day*. The contour intervals are $2 \times 10^{-4}[\Omega^2 \mathrm{day}^{-1}]$ for (a), $3 \times 10^{-4}[\Omega^2 \mathrm{day}^{-1}]$ for (b), and $1 \times 10^{-4}[\Omega^2 \mathrm{day}^{-1}]$ for (c).

(left). For the periodic solution (right), the contribution of wave-wave interaction between the stationary Wave 1 and the transient Wave 3 ($\overline{\zeta_2^* \mathcal{N}\left(\bar{\psi}_1, \psi_3^*\right)_2}$) is dominant with a tripole structure (Fig. 5.11b).

The contribution of the linear forcing (Fig. 5.11a) can be approximately explained by three terms, term concerning the radiative dumping $-\alpha\bar{\zeta_2^*}$ (top) in $\overline{\zeta_2^* \mathcal{L}(\psi_2^*)}$, and terms concerning advection $\overline{-\zeta_2^* v_2^* \frac{\partial\langle\bar{\zeta}\rangle}{a\partial\phi}}$ (middle) and $\overline{-\zeta_2^* \left(v_2^* \frac{\partial\bar{\zeta}^*}{a\partial\phi}\right)^*}$ (bottom) in $\overline{\zeta_2^* \mathcal{L}_\mathcal{N}\left(\bar{\psi}, \psi_2\right)^*}$. For the vacillation, $\overline{-\zeta_2^* \left(v_2^* \frac{\partial\bar{\zeta}^*}{a\partial\phi}\right)^*}$ is much smaller than the other two terms. Thus, the change of the enstrophy for transient Wave 2 is explained by the these three effects, the radiation, the advection by the time mean zonal mean flow $\overline{-\zeta_2^* v_2^* \frac{\partial\langle\bar{\zeta}\rangle}{a\partial\phi}}$, and the wave-wave interaction between traveling Waves 2 and 4. As for the periodic solution ($r = 0.032$), $\overline{-\zeta_2^* \left(v_2^* \frac{\partial\bar{\zeta}^*}{a\partial\phi}\right)^*}$ (Fig. 5.11a bottom) is significantly large as well as the other two terms, which cancels out the dipole structure of the term $\overline{\zeta_2^* \mathcal{N}\left(\psi_2^*, \psi_4^*\right)_2^*}$ at high latitude (Fig. 5.11b) and partly cancels the tripole pattern of the term $\overline{\zeta_2^* \mathcal{N}\left(\bar{\psi}_1, \psi_3^*\right)_2}$ (Fig. 5.11c bottom). The term $\overline{-\zeta_2^* v_2^* \frac{\partial\langle\bar{\zeta}\rangle}{a\partial\phi}}$ (Fig. 5.11a middle) cancels out the term $\overline{\zeta_2^* \mathcal{N}\left(\psi_2^*, \psi_4^*\right)_2^*}$ (Fig. 5.11b).

Furthermore, the mean absolute value of three dominant components between 63.7°S and 66.5°S of Term C is plotted for r in Fig. 5.12. The leading term changes from $\overline{-\zeta_2^* v_2^* \frac{\partial\langle\bar{\zeta}\rangle}{a\partial\phi}}$ to $\overline{v_2^* \left(\zeta_2^* \frac{\partial\bar{\zeta}^*}{a\partial\phi}\right)^*}$ at $r = 0.017$ with the régime transition and $\overline{v_2^* \left(\zeta_2^* \frac{\partial\bar{\zeta}^*}{a\partial\phi}\right)^*}$ increases monoton-

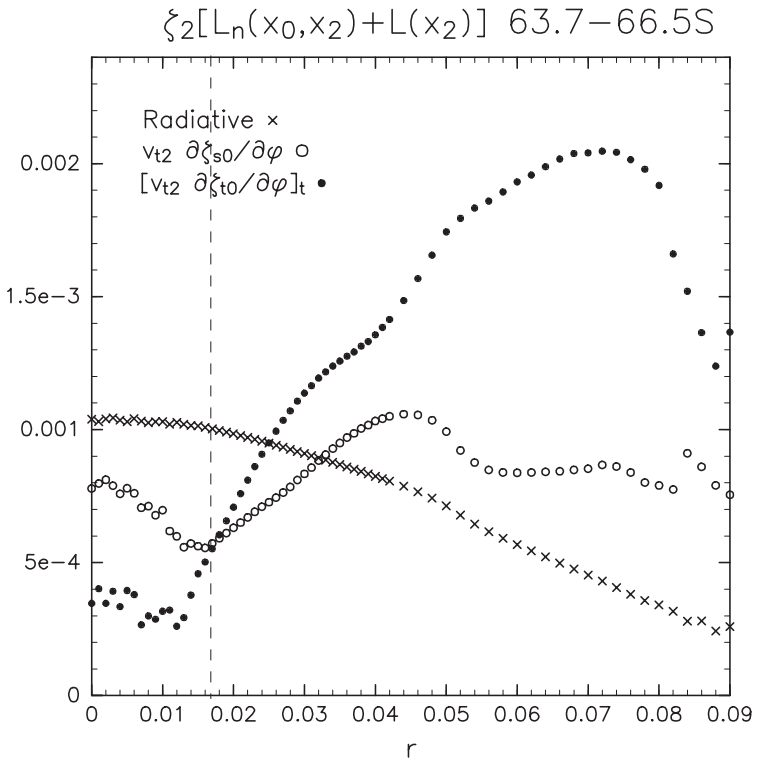

Figure 5.12: Time mean absolute value of the dominant components of the Term C between 63.7°S and 66.5°S plotted against the external parameter r; $-\alpha\bar{\zeta}_2^*$ (X mark), $\overline{-\zeta_2^* v_2^* \frac{\partial \langle\bar{\zeta}\rangle}{a\partial\phi}}$ (open circle), and $\overline{-\zeta_2^* \left(v_2^* \frac{\partial \bar{\zeta}^*}{a\partial\phi}\right)^*}$ (solid circle).

ically in similar way as Term E for the periodic solution (Fig. 5.10). These results suggest that the term$\overline{v_2^* \left(\zeta_2^* \frac{\partial \bar{\zeta}^*}{a\partial\phi}\right)^*}$ and $\overline{\zeta_2^* \mathcal{N}\left(\bar{\psi}_1, \psi_3^*\right)_2}$ are important for the periodic solution.

5.5 Discussion

Fig. 5.4 suggests that features of the solutions change around $r = 0.052$: The amplitude of the transient Wave 2 has a peak at $r = 0.052$. The maximum amplitude of the total Wave 2 is almost constant for $0.017 \leq r \leq 0.052$ which begins to decrease at $r = 0.052$. The maximum of the zonal mean flow increases with r for $0.017 \leq r \leq 0.052$ and keeps almost constant value for $r > 0.052$. As for the amplitude of the Wave 1, there is almost no variation in the minimum amplitude $0.017 \leq r \leq 0.052$. It increases with r for $0.052 \leq r \leq 0.08$.

Fig. 5.5 suggests the differences in the angular frequencies of the transient Waves 1 and 2 between the two ranges. As to $r < 0.052$, the circle and plus marks for Waves 1 and 2 are out of alignment with the dot which represents the phase of stationary component, whereas they are almost in alignment with the dot for $r > 0.052$.

Both the absolute value of Term A ($\bar{\zeta}^* \overline{\mathcal{N}\left(\psi_1, \psi_1\right)^*}$) and Term B ($\bar{\zeta}^* \overline{\mathcal{N}\left(\psi_2, \psi_2\right)^*}$) have the peak around $r = 0.052$ and decreases with r for $r > 0.052$, though for $r \leq 0.052$ Term C

almost cancels out Term D.

Term E in the enstrophy equation of Wave 2 dominates over Term D for $r \geq 0.058$ and the curve of Term C is along that of Term E for $r \geq 0.052$. These results suggest that Term C and Term E largely cancel out each other for $r \geq 0.052$.

5.6 Conclusions

Solutions of a barotropically unstable polar vortex with a topographic forcing are investigated in terms of wave-wave interactions for a wide range of the amplitude of the topography and the prescribed jet profile. When the topographic forcing $h = rH$ does not equal zero, I obtained four kinds of solutions, the vacillation, the periodic solution, the irregular solution, and the stationary-wave solution (Table 5.1). I sweep the parameter of the height of the topographic forcing r with $B = 4$ to investigate the flow régime in detail. The vacillating solution is obtained for the small $r < r_V = 0.016$, the irregular solution for large $r > r_I = 0.08$, and the periodic solution for $r_V < r < r_I$ (Figs. 5.4 and 5.5). The variable ranges of zonal flow and the amplitude of the Wave 2 become narrower with r for the vacillation and broaden for the periodic solution (Fig. 5.4).

For the periodic solution, the mean zonal flow fluctuates in saw-tooth waveform and both Waves 1 and 2 propagate eastward with the same frequency, while for the vacillation, the mean zonal flow fluctuates sinusoidally and both the polar diagram of the Wave 1 and that of the Wave 2 show torus structure (Fig. 5.5).

The diagnosis of the enstrophy equation of the mean zonal flow makes clear that the contribution of Wave 1 is much smaller than that for Wave 2 for the vacillation, while for the periodic solution, the contribution of Wave 1, which is largely canceled out by Wave 2, is the leading term (Figs. 5.6 and 5.7). This large contribution of Wave 1 is almost derived from the interference between the stationary and traveling components (Fig. 5.8).

As for the diagnosis of the enstrophy equation for Wave 2, the term concerning the wave-wave interaction between the Waves 2 and 4 largely cancels out the term concerning the linear forcing for both the vacillation and the periodic solution (Figs. 5.9 and 5.10). For the vacillation, the enstrophy tendency is roughly explained by the radiative dumping, the contribution of stationary zonal mean flow, and the nonlinear effect of the transient Wave 2 and the transient Wave 4. On the other hand, for the periodic solution, the contribution of the transient zonal mean flow and the contribution of wave-wave interaction between the stationary Wave 1 and the transient Wave 3 are also important for the enstrophy tendency (Figs. 5.11 and 5.12).

A Appendix

I introduce the enstrophy equation for the transient zonal flow and transient Wave 2 for the governing equation:

$$\frac{D}{Dt}\left(\bar{\zeta}+f+\frac{fh}{H}\right)=-\alpha(\zeta-\overline{\zeta_0})+\nu\left(\nabla^2+\frac{2}{a^2}\right)(\zeta-\overline{\zeta_0}). \tag{5.1}$$

Defining $R=\frac{fh}{H}$ and taking Fourier decomposition in longitude for each field u, v, ζ, R, Eq. (5.1) can be written

$$\begin{aligned}\frac{\partial\zeta}{\partial t}+\sum_k\frac{\partial\zeta_k}{\partial t}=&-\alpha\left(\bar{\zeta}+\sum_k\zeta_k-\bar{\zeta}_0\right)+\left(\nabla^2+\frac{2}{a^2}\right)\left(\bar{\zeta}+\sum_k\zeta_k-\bar{\zeta}_0\right)\\&-\bar{u}\frac{1}{a\cos\phi}\frac{\partial\zeta_k}{\partial\lambda}-\frac{1}{a}\frac{\partial\left(\bar{\zeta}+f\right)}{\partial\phi}v_k-\bar{u}\frac{1}{a\cos\phi}\frac{\partial R_k}{\partial\lambda}\\&-\sum_k\sum_l\left\{\nabla\cdot(\mathbf{u}_k\zeta_l)\right\}-\sum_k\sum_l\left\{\nabla\cdot(\mathbf{u}_kR_l)\right\}.\end{aligned} \tag{A.1}$$

Note that R does not have zonal component (Eq. 5.6). Taking the zonal mean and Fourier decomposition in longitude of Eq. (A.1) result in

$$\frac{\partial\bar{\zeta}}{\partial t}=-\alpha(\bar{\zeta}-\bar{\zeta}_0)+\left(\nabla^2+\frac{2}{a^2}\right)\left(\bar{\zeta}-\bar{\zeta}_0\right)-\sum_k\overline{\nabla\cdot(\mathbf{u}_k\zeta_k)}-\sum_k\overline{\nabla\cdot(\mathbf{u}_kR_k)}, \tag{A.2}$$

$$\begin{aligned}\frac{\partial\zeta_k}{\partial t}=&-\alpha\zeta_k+\left(\nabla^2+\frac{2}{a^2}\right)\zeta_k\\&-\bar{u}\frac{1}{a\cos\phi}\frac{\partial\zeta_k}{\partial\lambda}-\bar{u}\frac{1}{a\cos\phi}\frac{\partial R_k}{\partial\lambda}-\frac{1}{a}\frac{\partial(\bar{\zeta}+f)}{\partial\phi}v_k\\&-\sum_l\sum_m\{\nabla\cdot(\mathbf{u}_l\zeta_m)\}_k-\sum_l\sum_m\{\nabla\cdot(\mathbf{u}_lR_m)\}_k.\end{aligned} \tag{A.3}$$

Dividing each field into the stationary component ($\langle A\rangle$) and transient component (A^*), Equations (A.2) and (A.3) are rewritten as follows:

$$\begin{aligned}\frac{\partial\bar{\zeta}^*}{\partial t}=&-\alpha(\langle\bar{\zeta}\rangle+\bar{\zeta}^*-\bar{\zeta}_0)+\left(\nabla^2+\frac{2}{a^2}\right)\left(\langle\bar{\zeta}\rangle+\bar{\zeta}^*-\bar{\zeta}_0\right)\\&-\sum_k\left[\overline{\nabla\cdot(\langle\mathbf{u}_k\rangle\langle\zeta_k\rangle)}+\overline{\nabla\cdot(\langle\mathbf{u}_k\rangle\zeta_k^*)}+\overline{\nabla\cdot(\mathbf{u}_k^*\langle\zeta_k\rangle)}+\overline{\nabla\cdot(\mathbf{u}_k^*\zeta_k^*)}\right]\\&-\sum_k\left[\overline{\nabla\cdot(\langle\mathbf{u}_k\rangle R_k)}+\overline{\nabla\cdot(\mathbf{u}_k^*R_k)}\right],\end{aligned} \tag{A.4}$$

$$
\begin{aligned}
\frac{\partial \zeta_k^*}{\partial t} =& -\alpha\left(\langle\zeta_k\rangle+\zeta_k^*\right)+\left(\nabla^2+\frac{2}{a^2}\right)\left(\langle\zeta_k\rangle+\zeta_k^*\right)\\
&-\langle\bar{u}\rangle\frac{1}{a\cos\phi}\frac{\partial\langle\zeta_k\rangle}{\partial\lambda}-\langle\bar{u}\rangle\frac{1}{a\cos\phi}\frac{\partial\zeta_k^*}{\partial\lambda}-\bar{u}^*\frac{1}{a\cos\phi}\frac{\partial\langle\zeta_k\rangle}{\partial\lambda}-\bar{u^*}\frac{1}{a\cos\phi}\frac{\partial\zeta_k^*}{\partial\lambda}\\
&-\langle\bar{u}\rangle\frac{1}{a\cos\phi}\frac{\partial R_k}{\partial\lambda}-\bar{u^*}\frac{1}{a\cos\phi}\frac{\partial R_k}{\partial\lambda}\\
&-\frac{1}{a}\frac{\partial(\langle\bar{\zeta}\rangle+f)}{\partial\phi}\langle v_k\rangle-\frac{1}{a}\frac{\partial(\langle\bar{\zeta}\rangle+f)}{\partial\phi}v_k^*-\frac{1}{a}\frac{\partial\bar{\zeta^*}}{\partial\phi}\langle v_k\rangle-\frac{1}{a}\frac{\partial\bar{\zeta^*}}{\partial\phi}v_k^*\\
&-\sum_l\sum_m\left[\{\nabla\cdot(\langle\mathbf{u}_l\rangle\langle\zeta_m\rangle)\}_k+\{\nabla\cdot(\langle\mathbf{u_l}\rangle\zeta_m^*)\}_k+\{\nabla\cdot(\mathbf{u}_l^*\langle\zeta_m\rangle)\}_k+\{\nabla\cdot(\mathbf{u}_l^*\zeta_m^*)\}_k\right]\\
&-\sum_l\sum_m\left[\{f\nabla\cdot(\langle\mathbf{u}_l\rangle R_m)\}_k+\{\nabla\cdot(\mathbf{u}_l^*R_m)\}_k\right].
\end{aligned}
\tag{A.5}
$$

Taking the zonal mean of Eqs. (A.4) and (A.5) results in

$$
\begin{aligned}
0 =& -\alpha(\langle\bar{\zeta}\rangle-\zeta_0)\\
&-\sum_k\left[\overline{\nabla\cdot(\langle\mathbf{u}_k\rangle\langle\zeta_k\rangle)}+\left\langle\overline{\nabla\cdot(\mathbf{u}_k^*\zeta_k^*)}\right\rangle\right]\\
&-\sum_k\overline{\nabla\cdot(\langle\mathbf{u}_k\rangle R_k)},
\end{aligned}
\tag{A.6}
$$

$$
\begin{aligned}
0 =& -\alpha\langle\zeta_k\rangle+\left(\nabla^2+\frac{2}{a^2}\right)\langle\zeta_k\rangle\\
&-\langle\bar{u}\rangle\frac{1}{a\cos\phi}\frac{\partial\langle\zeta_k\rangle}{\partial\lambda}-\frac{1}{a\cos\phi}\left\langle\overline{u^*}\frac{\partial\zeta_k^*}{\partial\lambda}\right\rangle\\
&-\langle\bar{u}\rangle\frac{1}{a\cos\phi}\frac{\partial R_k}{\partial\lambda}\\
&-\frac{1}{a}\frac{\partial\langle\bar{\zeta}\rangle}{\partial\phi}\langle v_k\rangle-\frac{1}{a}\left\langle\frac{\partial\bar{\zeta^*}}{\partial\phi}v_k^*\right\rangle\\
&-\sum_l\sum_m\left[\{\nabla\cdot(\langle\mathbf{u}_l\rangle\langle\zeta_m\rangle)\}_k+\langle\nabla\cdot(\mathbf{u}_l^*\zeta_m^*)\rangle_k\right]\\
&-\sum_l\sum_m\{\nabla\cdot(\langle\mathbf{u}_l\rangle R_m)\}_k.
\end{aligned}
\tag{A.7}
$$

Subtracting Eq. (A.6) from Eq. (A.4), and Eq. (A.7) from Eq. (A.5), we get the vorticity equation for zonal flow and transient component of wavenumber k.:

$$
\begin{aligned}
\frac{\partial\bar{\zeta}^*}{\partial t} =& -\alpha\bar{\zeta}^*+\left(\nabla^2+\frac{2}{a^2}\right)\zeta_k^*\\
&-\sum_k\left[\overline{\nabla\cdot(\langle\mathbf{u}_k\rangle\zeta_k^*)}+\overline{\nabla\cdot(\mathbf{u}_k^*\langle\zeta_k\rangle)}+\left\{\overline{\nabla\cdot(\mathbf{u}_k^*\zeta_k^*)}\right\}^*\right]\\
&-\sum_k\overline{\nabla\cdot(\mathbf{u}_k^*R_k)},
\end{aligned}
\tag{A.8}
$$

$$
\begin{aligned}
\frac{\partial \zeta_k^*}{\partial t} = & -\alpha\zeta_k^* + \left(\nabla^2 + \frac{2}{a^2}\right)\zeta_k^* \\
& - \langle\bar{u}\rangle \frac{1}{a\cos\phi}\frac{\partial \zeta_k^*}{\partial \lambda} - \bar{u}^* \frac{1}{a\cos\phi}\frac{\partial \langle\zeta_k\rangle}{\partial \lambda} - \left\{\bar{u^*}\frac{1}{a\cos\phi}\frac{\partial \zeta_k^*}{\partial \lambda}\right\}^* \\
& - \bar{u^*}\frac{1}{a\cos\phi}\frac{\partial R_k}{\partial \lambda} \\
& - \frac{1}{a}\frac{\partial \langle\bar{\zeta}\rangle}{\partial \phi} v_k^* - \frac{1}{a}\frac{\partial(\bar{\zeta}^* + f)}{\partial \phi}\langle v_k\rangle - \frac{1}{a}\left\{\frac{\partial \bar{\zeta}^*}{\partial \phi} v_k^*\right\}^* \\
& - \sum_l \sum_m \left[\left\{\nabla\cdot\left(\langle\mathbf{u_l}\rangle\,\zeta_m^*\right)\right\}_k + \left\{\nabla\cdot\left(\mathbf{u}_l^*\,\langle\zeta_m\rangle\right)\right\}_k + \left\{\nabla\cdot\left(\mathbf{u}_l^*\zeta_m^*\right)\right\}_k^*\right] \\
& - \sum_l \sum_m \left\{\nabla\cdot\left(\mathbf{u}_l^* R_m\right)\right\}_k .
\end{aligned}
\tag{A.9}
$$

Multiplying Eq. (A.8) by $\bar{\zeta}^*$, and Eq. (A.9) by ζ_k^*, respectively, and taking a zonal mean, we finally obtain enstrophy equation for transient zonal mean zonal flow and wavenumber k.

$$
\begin{aligned}
\frac{\partial}{\partial t}\frac{\overline{\zeta}^{*2}}{2} = & \underbrace{\left[-\alpha\overline{\zeta^{*2}} + \overline{\zeta}^*\left\{\left(\nabla^2 + \frac{2}{a^2}\right)\overline{\zeta^*}\right\}\right]}_{\bar{\zeta}^*\mathcal{L}(\bar{\psi}^*)} \\
& \underbrace{-\sum_k \left[\nabla\cdot\left(\overline{\mathbf{u}_k^*\zeta_k}\right) + \nabla\cdot\left(\overline{\mathbf{u}_k\zeta_k^*}\right) + \left\{\nabla\cdot\left(\overline{\mathbf{u}_k^*\zeta_k^*}\right)\right\}^* + \nabla\cdot\overline{\left\{\mathbf{u}_k^*\left(R_k\right)\right\}}\right]}_{\sum_k \bar{\zeta}^*\overline{\mathcal{N}\left(\psi_k,\,\psi_k\right)^*}},
\end{aligned}
\tag{A.10}
$$

$$
\begin{aligned}
\frac{\partial}{\partial t}\frac{\overline{\zeta_k^{*2}}}{2} = & \underbrace{\left[-\alpha\overline{\zeta_k^{*2}} + \overline{\zeta_k^*\left\{\left(\nabla^2 + \frac{2}{a^2}\right)\zeta_k^*\right\}}\right]}_{\overline{\zeta_k^*\mathcal{L}(\psi_k^*)}} \\
& \underbrace{-\left[\begin{array}{l}
\overline{\zeta_k^*\overline{u^*}\frac{1}{a\cos\phi}\frac{\partial\langle\zeta_k\rangle}{\partial\lambda}} + \overline{\zeta_k^*\left\{\overline{u}^*\frac{1}{a\cos\phi}\frac{\partial\zeta_k^*}{\partial\lambda}\right\}^*} + \overline{\zeta_k^*\overline{u}^*\frac{1}{a\cos\phi}\frac{\partial R_k}{\partial\lambda}} \\
+\overline{\zeta_k^* v_k^*}\frac{\partial\left(\langle\overline{\zeta}\rangle + f\right)}{a\partial\phi} + \overline{\zeta_k^*\langle v_k\rangle\frac{\partial\overline{\zeta^*}}{a\partial\phi}} + \overline{\zeta_k^*\left\{v_k^*\frac{\partial\overline{\zeta}^*}{a\partial\phi}\right\}^*}
\end{array}\right]}_{\overline{\zeta_k^*\mathcal{L}_{\mathcal{N}}\left(\bar{\psi},\,\psi_k\right)^*}} \\
& \underbrace{-\sum_l\sum_m\left[\begin{array}{l}
\overline{\zeta_k^*\left\{\nabla\cdot\left(\mathbf{u}_l\zeta_m^*\right)\right\}_k} + \overline{\zeta_k^*\left\{\nabla\cdot\left(\mathbf{u}_l^*\zeta_m\right)\right\}_k} \\
+\overline{\zeta_k^*\left\{\nabla\cdot\left(\mathbf{u}_l^*\zeta_m^*\right)\right\}_k^*} + \overline{\zeta_k^*\left\{\nabla\cdot\left(\mathbf{u}_l^* R_m\right)\right\}_k}
\end{array}\right]}_{\sum_l\sum_m\overline{\zeta_k^*\mathcal{N}\left(\psi_l,\psi_m\right)_k^*}}.
\end{aligned}
\tag{A.11}
$$

Here, $R_k = 0$ for $k \neq 1$ in this study because the surface topography of zonal wavenumber 1 was assumed (Eq. (5.6)). I evaluate each quantity in the square bracket in the right hand side of Eqs. (A.10) and (A.11) for Wave 2.

Chapter 6

Conclusions

The winter stratospheric polar vortex in the Southern Hemisphere (SH) is colder with strong polar-night jet than that in the Northern Hemisphere, and persists into springtime fundamentally due to the small amplitude of large-scale planetary wave forcing from the troposphere. Interannual variations of the stratospheric circulations in the SH stratosphere were investigated from a view point of activities of dominant planetary waves, the stationary wave of zonal wavenumber 1 (Wave 1) and the eastward traveling Wave 2 with the long period of NCEP/NCAR Reanalysis dataset.

In September 2002, the polar vortex split into two and a major stratospheric sudden warming event occurred in the first time over the two decades of satellite observations. In Chapter 2, I investigated interannual variations of the seasonal march for 24 years from 1979 to 2002 and characterized the dynamical features of the unprecedented year 2002 by comparing with the other 23 years. Interannual variations in the seasonal march were characterized by variations in the timing of the deceleration of the polar-night jet. The upward EP flux in the lower stratosphere is a good indicator of the interannual variations of the seasonal march of the stratospheric circulation through winter and spring: The stronger wave activity in the lower stratosphere is associated with the earlier shift-down of the polar-night jet. In 2002, the upward flux of the wave activity in the lower stratosphere was extremely large in August compared with the other years and the large wave driving caused the earlier and larger deceleration of the mean zonal wind in the stratosphere.

In Chapter 3, I investigated the interannual variations of the stratospheric stationary waves in late winter (September and October) in associated with the tropospheric circulation patterns. Year-to-year variations of stationary planetary waves in late winter are characterized by longitudinal phase shifts and amplitude variations of Wave 1. The phase variations were well related to the variations in the tropospheric jet structure. The activities of synoptic-scale wave changed those features to maintain the tropospheric jet structure. The amplitude variations of stationary Wave 1 were closely related to those of the meridional heat flux by planetary-scale waves in the upper troposphere.

In Chapter 4, quasi-periodic variations of the polar vortex were examined in terms of the wave-wave interaction between the two dominant waves, the stationary Wave 1 and the eastward traveling Wave 2. A case study about October in 1996 made clear that eastward traveling Wave 1 with the same angular frequency as the traveling Wave 2 was generated by the wave-wave interaction, which had a latitudinal node around 60°S where the amplitude

of the two primary waves were large. Furthermore, the amplitude of traveling Wave 1 and Wave 2 changed quasi-periodically and the polar night jet also vacillated with the similar frequency. The zonal flow vacillation was a basically result of quasi-periodic variations of the wave driving by the interference of the stationary and traveling Wave 1. Such quasi-periodic variations due to wave-wave interaction often occurred for the 24 years in late winter when both the stationary Wave 1 and the transient Wave 2 were vigorous. Similar periodic variations of the polar vortex were obtained in the numerical experiment with a spherical barotropic model in the condition that the stationary Wave 1 generated by the topographic forcing and the eastward traveling Wave 2 due to barotropic instability of the forced mean zonal wind were dominant.

In Chapter 5, I investigated the time variations of the polar vortex in the barotropic model with time independent topographic forcing of zonal wavenumber 1 for a wide range of topographic amplitude and jet profile, focusing on the effect of the wave-wave interaction. When the prescribed zonal flow was barotropically unstable profile, the flow régime changed from the vacillating solution to the periodic one and finally the irregular one with the increase of topography height. The variable range of the Wave 2, as well as that of the mean zonal flow, changed its features with the transition of the flow règime. The enstrophy diagnosis made clear that the interaction between transient Waves 2 and 4 was important for the vacillation. On the other hand, the wave-wave interaction between the stationary Wave 1 and transient Wave 3 was also important for the time change of the Wave 2 for the periodic solution.

Through this study, I investigated the several features of the stratospheric circulations in statistical ways and by a case study. However, statistical studies always suffer the limitation of the data length. As shown in the example in Chapter 3, full dynamical troposphere-stratosphere coupled models will be useful to supplement the statistical arguments based on much longer datasets. The barotropic model used in Chapters 4 and 5 was also great help for understanding of the dynamical mechanism of the observed phenomena. Studies combining analyses of observational data and experiments using a full dynamic model or a simple model will largely develop our understanding of the dynamics in the stratosphere.

References

Allen, D. R., R. M. Bevilacqua, G. E. Nedoluha, C. E. Randall, and G. L. Manney, 2003: Unusual stratospheric transport and mixing during the 2002 Antarctic winter. *Geophy. Res. Lett.*, **30**, 1599, doi:10.1029/2003GL017117

Andrews, D. G., J. R. Holton, and C. B. Leovy, 1987: *Middle Atmosphere Dynamics.* Academic Press, 489 pp.

Aoki, H., M. Shiotani, and I. Hirota, 1996: Interannual variability of the tropospheric circulation and its relation to the stratosphere in the southern hemisphere. *J. Meteor. Soc. Japan*, **74**, 509-523.

Aoki, H., and I. Hirota, 1998: Quasi-stationary planetary waves in the southern hemisphere troposphere. *J. Meteor. Soc. Japan*, **76**, 581-596.

Baldwin, M.P., T. Hirooka, A. O'Neill, and S. Yoden, 2003: Major stratospheric warming in the Southern Hemisphere in 2002: Dynamical aspects of the ozone hole split. *SPARC Newsletter*, **20**, 24-26.

Charney, J., and P. Drazin, 1961: Propagation of planetary scale disturbances from the lower into the upper atmosphere. *J. Geophys. Res.*, **66**, 83-109.

Fusco, A., and M. L. Salby, 1999: Interannual variations of total ozone and their relationship to variations of planetary wave activity. *J. Climate*, **12**, 1619-1629.

Hartmann D. L., 1976: The structure of the stratosphere in the Southern Hemisphere during late winter 1973 as observed by satellite. *J. Atmos. Sci.*, **33**, 1141-1154.

——, 1979: Baroclinic instability of realistic zonal-mean states to planetary waves. *J. Atmos. Sci.*, **40**, 817-835.

——, 1983: Barotropic instability of the polar night jet stream. *J. Atmos. Sci.*, **40**, 817-835.

——, C. R. Mechoso, and K. Yamazaki, 1984: Observations of wave-mean flow interaction in the southern hemisphere. *J. Atmos. Sci.*, **41**, 351-362.

——, and F. Lo, 1998: Wave-driven zonal flow vacillation in the southern hemisphere. *J. Atmos. Sci.*, **55**, 1303-1315.

Harwood, R. S., 1975: The temperature structure of the Southern Hemisphere stratosphere August-October 1971. *Quart. J. Roy. Meteor. Soc.*, **101**, 75-91.

Hio, Y., and I. Hirota, 2002: Interannual variations of planetary waves in the Southern Hemisphere stratosphere. *J. Meteor. Soc. Japan*, **80**, 1013-1027.

——, and S. Yoden, 2004a: Interannual variations of the seasonal march in the Southern Hemisphere stratosphere for 1979-2002 and characterization of the unprecedented Year 2002. *J. Atmos. Sci.* in revision.

——, and ——, 2004b: Quasi-periodic variations of the polar vortex in the Southern Hemisphere stratosphere due to wave-wave interaction. *J. Atmos. Sci.* in revision.

Hirooka, T., 1986: Influence of normal mode Rossby waves on the mean field: Interference with quasi-stationary waves. *J. Atmos. Sci.*, **43**, 2088-2097.

Hirota, I., and Y. Sato, 1969: Periodic variation of the winter stratospheric circulation and intermittent vertical propagation of planetary waves. *J. Meteor. Soc. Japan*, **47**, 390-402.

——, T. Hirooka, and M. Shiotani, 1983 : Upper stratospheric circulations in the two hemispheres observed by satellites. *Quart. J. Roy. Meteor. Soc.*, **109**, 443-454.

——, K. Kuroi, and M. Shiotani, 1990: Midwinter warmings in the southern hemisphere stratosphere in 1988. *Quart. J. Roy. Meteor. Soc.*, **116**, 929-941.

Holton, J.R. , 1992: *An introduction to Dynamic Meteorology.* Academic Press, 497 pp.

——, and C. Mass, 1976: Stratospheric vacillation cycles. *J. Atmos. Sci.*, **33**, 2218-2225.

Ishioka, K., 2002: ispack-0.61 GFD-DENNOU Club. [Available online at http://www.gfd-dennou.org/arch/ispack/.]

——, and S. Yoden, 1995: Non-linear aspects of barotropically unstable polar vortex in a forced-dissipative system: flow régimes and tracer transport. *J. Meteor. Soc. Japan*, **73**, 201-212.

Jackes, M. N., and M. E. McIntyre, 1987: A high-resolution one-layer model of breaking planetary waves in the stratosphere. *Nature*, **328**, 590-596.

James, I. N., 1988: On the forcing of planetary-scale Rossby waves by Antarctica. *Quart. J. Roy. Meteor. Soc.* **114**, 619-637.

Kalnay, E., M. Kanamitsu, R. Kistler, W. Collins, D. Deaven, L. Gandin, M. Iredell, S. Saha, G. White, J. Woollen, Y. Zhu, M. Chelliah, W. Ebisuzaki, W. Higgins, J.

Janowiak, K. C. Mo, C. Ropelewski, J. Wang, A. Leetmaa, R. Reynolds, R. Jenne, and D. Joseph, 1996: The NCEP/NCAR 40-year reanalysis project. *Bull. Amer. Meteor. Soc.*, **77**, 437-471.

Kanzawa, H., and S. Kawaguchi, 1990: Large stratospheric sudden warming in Antarctic late winter and shallow ozone hole in 1988. *Geophys. Res. Lett.*, **17**, 77-80.

Karoly, D. J., 1990: The role of transient eddies in low-frequency zonal variations in the southern hemisphere circulation. *Tellus*, **42A**, 41-50.

——, and B. J. Hoskins, 1982: Three dimensional propagation of planetary waves. *J. Meteor. Soc. Japan*, **60**, 109-122.

Kayano, M. T., 1997: Principal modes of the total ozone on the Southern Oscillation timescales and related temperature variations. *J. Geophys. Res.*, **102**, 25797-25806.

Kuroda, Y., and K. Kodera, 1998: Interannual variability in the troposphere and stratosphere of the southern hemisphere winter. *J. Geophys. Res.*, **103**, 13787-13799.

Leovy, C. B., and P. J. Webster, 1976: Stratospheric long waves: Comparisons of thermal structure in the Northern and Southern Hemisphere. *J. Atmos. Sci.*, **33**, 1141-1154.

Lighthill, J., 1978: *Waves in fluid.* Cambridge University Press, 504 pp.

Limpasuvan, V., and L. Hartmann, 2000: Wave-maintained annular modes of climate variability. *J. Climate*, **13**, 4418-4429.

Manney, G.L., T. R. Nathan, and J. L. Stanford, 1988: Barotropic stability of realistic stratospheric jets. *J. Atmos. Sci.*, **45**, 2545-2555.

——, J. D. Farrara, and C. R. Mechoso, 1991a: The behavior or wave 2 in the Southern Hemisphere stratosphere during late winter and early spring. *J. Atmos. Sci.*, **48**, 976-998.

——, C. R. Mechoso, L. S. Elson, and J. D. Farrara, 1991b: Planetary-scale waves in the Southern Hemisphere winter and early spring stratosphere: stability analysis. *J. Atmos. Sci.*, **48**, 2509-2523.

——, J. L. Sabutis, D. R. Allen, W. A. Lahoz, A. A. Scaife, C. E. Randall, S. Pawson, R. Swinbank, and B. Naujokat, 2004: Simulations of dynamics and transport during the September 2002 Antarctic major warming. submitted to *J. Atmos. Sci.*

Mechoso, C. R., D. L. Hartmann, and J. D. Farrara, 1985: Climatology and interannual variability of wave, mean-flow interaction in the Southern Hemisphere. *J. Atmos. Sci.*, **42**, 2189-2206.

——, A. O'Neill, V. D. Pope, and J. D. Farrara, 1988: A study of stratospheric final warming of 1982 in the southern hemisphere. *Quart. J. Roy. Meteor. Soc.*, **114**, 1365-1384.

Mizuta, R., and S. Yoden, 2001: Chaotic mixing and transport barriers in an idealized stratospheric polar vortex. *J. Atmos. Sci.*, **58**, 2615-2628 .

Naito, Y., 2002: Planetary wave diagnostics on the QBO effects on the deceleration of the polar-night jet in the southern hemisphere. *J. Meteor. Soc. Japan*, **80**, 985-995.

Newman, P., E. Nash, and J. Rosenfield, 2001: What controls the temperature of the Arctic stratosphere during the spring? *J. Geophys. Res.*, **106**, 19999-20010.

North, G. R., T. L. Bell, R. F. Cahalan, and F. J. Moeng, 1982: Sampling errors in the estimation of empirical orthogonal functions. *Mon. Wea. Rev.*, **110**, 699-706.

Plumb, R. A., 2002: Stratospheric transport. *J. Meteor. Soc. Japan*, **80**, 793-809.

Quintanar, A. I., and C. R. Mechoso, 1995a: Quasi-stationary waves in the southern hemisphere. Part I: Observational data. *J. Climate*, **8**, 2659-2672.

——, and ——, 1995b: Quasi-stationary waves in the southern hemisphere. Part II: generation mechanism. *J. Climate*, **8**, 2673-2690.

Randel, W. J., 1987: A study of planetary waves in the southern winter troposphere and stratosphere. Part I: Wave structure and vertical propagation. *J. Atmos. Sci.*, **44**, 917-935.

——, W. J., and P. A. Newman, 1998: The stratosphere in the Southern Hemisphere. In *Meteorology of the Southern Hemisphere* edited by D.J. Karoly and D.G. Vincent. *Meteor. Monographs*, **27**, 243-282.

——, F. Wu, and R. Stlarski, 2002: Changes in column ozone correlated with the stratospheric EP flux. *J. Meteor. Soc. Japan*, **80**, 849-862.

Robinson, W. A., 1985: A model of the wave 1-wave 2 vacillation in the winter stratosphere. *J. Atmos. Sci.*, **42**, 2289-2304.

Rong, P. P., and D. W. Waugh, 2003: Vacillations in a shallow water model of the stratosphere. submitted to *J. Atmos. Sci.*

Salby, M., and R. Garcia, 1987: Vacillations induced by interference of stationary and traveling planetary waves. *J. Atmos. Sci.*, **44**, 2679-2711.

——, and P. F. Callaghan, 2002: Interannual changes of the stratospheric circulation: relationship to ozone and tropospheric structure. *J. Climate*, **15**, 3673-3685.

Scaife, A. A., and I. N. James, 2000: Response of the stratosphere to interannual variability of tropospheric planetary waves. *Quart. J. Roy. Meteor. Soc.*, **126**, 275-297.

——, D. R. Jackson, R. Swinbank, N. Batchart, H. E. Thornton, M. Keil, and L. Henderson, 2004: Stratospheric vacillations and the major warming over Antarctica in 2002. submitted to *J. Atmos. Sci.*

Scinocca J. F., and P. H. Haynes, 1998: Dynamical forcing of stratospheric planetary waves by tropospheric baroclinic eddies. *J. Atmos. Sci.*, **55**, 2361-2392.

SGKS Group, 2001: DCL-5.2. (in Japanese). GFD-DENNOU Club. [Available online at http://www.gfd-dennou.org/library/dcl/.]

Shiotani, M., 1990: Low-frequency variations of the zonal mean state of the Southern Hemisphere troposphere. *J. Meteor. Soc. Japan*, **68**, 461-470.

——, K. Kuroi, and I. Hirota, 1990: Eastward traveling waves in the southern hemisphere during the spring of 1983. *Quart. J. Roy. Meteor. Soc.*, **116**, 913-927.

——, N. Shimoda, and I. Hirota, 1993: Interannual variability of the stratospheric circulation in the southern hemisphere. *Quart. J. Roy. Meteor. Soc.*, **119**, 531-546.

Smith, A. K., 1983: Observation of wave-wave interactions in the stratosphere. *J. Atmos. Sci.*, **40**, 2486-2496.

——, J. C. Gille, and L. V. Lyjak, 1984: Wave-wave interactions in the stratosphere: observations during quiet and active wintertime periods. *J. Atmos. Sci.*, **41**, 363-373.

Taguchi, M., and S. Yoden, 2002: Internal intraseasonal and interannual variations of the troposphere-stratosphere coupled system in a simple global circulation model. Part II: Millennium integrations. *J. Atmos. Sci.*, **59**, 3037-3050.

Thuburn, J., and V. Lagneau, 1999: Eulerian mean, contour integral, and finite-amplitude wave activity diagnostics applied to a single layer model of the winter stratosphere. *J. Atmos. Sci.*, **56**, 689-710.

Trenberth, K. E., 1991: Storm tracks in the southern hemisphere. *J. Atmos. Sci.*, **48**, 2159-2178.

Ushimaru, S., and H. Tanaka, 1992: A numerical study of the interaction between stationary Rossby waves and eastward-traveling waves in the southern hemisphere stratosphere. *J. Atmos. Sci.*, **42**, 1354-1373.

Watterson, I. G., and I. N. James, 1992: Baroclinic waves propagating from high latitude source. *Quart. J. Roy. Meteor. Soc.*, **118**, 23-50.

Wilks, D. S., 1995: *Statistical methods in the atmospheric sciences.* Academic Press, 467 pp.

Yoden, S., 1987: Bifurcation properties of a stratospheric vacillation model. *J. Atmos. Sci.*, **44**, 1723-1733.

——, M. Shiotani, and I. Hirota, 1987: Multiple planetary flow regimes in the southern hemisphere. *J. Meteor. Soc. Japan*, **65**, 571-586.

Young, R., and H. Houben, 1989: Dynamics of planetary-scale baroclinic waves during southern hemisphere winter. *J. Atmos. Sci.*, **46**, 1365-1383.

This thesis is based on the following papers:

1. Interannual Variations of Planetary Waves in the Southern Hemisphere Stratosphere.
   Yasuko Hio and Isamu Hirota
   Journal of the Meteorological Society of Japan, 2002 **vol.80** 1013-1027.

2. Interannual Variations of the Seasonal March in the Southern Hemisphere Stratosphere for 1979-2002 and characterization of the unprecedented year 2002.
   Yasuko Hio and Shigeo Yoden
   Journal of the Atmospheric Sciences in revision.

3. Quasi-Periodic Variations of the Polar Vortex in the Southern Hemisphere Stratosphere due to Wave-Wave Interaction.
   Yasuko Hio and Shigeo Yoden
   Submitted to *Journal of the Atmospheric Sciences*.

Acknowledgments

I wish to express my special thank to Dr. Isamu Hirota for his continuous encouragement and fruitful suggestion. I also would like to gratefully acknowledge the enthusiastic supervision of Prof. Shigeo Yoden through the work. I thank Dr. Keiichi Ishioka for his efficient library package of the spherical barotropic model with the spectral transform method (Ishioka 2002). I would like to acknowledge the help by Dr. Ryo Mizuta for giving the program source of his model and courteous answers to my inquiries for it. I want to thank Dr. Yoko Naito and Dr. Masakazu Taguchi for helpful comments. I am grateful to all the members of the Meteorological Laboratory at Kyoto University for their warm words of encouragement, helpful discussion and advice. The GFD-DENNOU library (SGKS Group 2001) was used for graphical output. Computations were done at the Academic Center for Computing and Media Studies, Kyoto University. Finally, I am indebted to my parents for their understanding and endless encouragement when it was most required.